Journal of Achievements in Materials and Manufacturing Engineering
VOLUME 61
ISSUE 2
December
2013

Precipitation evolution and surface modification of magnesium alloys

T. Tański [a,*], M. Król [a], L.A. Dobrzański [a], Sz. Malara [b], J. Domagała-Dubiel [b]
[a] Institute of Engineering Materials and Biomaterials,
Silesian University of Technology,ul. Konarskiego 18a, 44-100 Gliwice, Poland
[b] Institute of Non-ferrous Metals, ul. Sowińskiego 5, 44-100 Gliwice, Poland
* Corresponding e-mail address: tomasz.tanski@polsl.pl

Received 21.10.2013; published in revised form 01.12.2013

Materials

ABSTRACT

Purpose: The purpose of this publication is to present the results of own long-term research summarising the experience concerning as casting magnesium alloys, and in especially a thermal analysis describing the process of alloys crystallisation, standard heat treatment according to the occurring phase transitions and precipitation processes, surface treatment with the CVD and PVD methods, laser surface treatment of surface layers, as well as using the methods of Computer Materials Science.
Design/methodology/approach: The research concerned in the first place an analysis of Mg-Al-Zn alloys crystallisation kinetics. Optimisation investigations for heat treatment conditions taking into consideration different cooling mediums were performed in order to identify fully the structure of the investigated magnesium casting alloys. Investigations were carried out of the structure and properties of coatings produced with the CVD and PVD methods on the investigated Mg-Al-Zn alloys. The last stage of investigating the presented Mg-Al-Zn alloys applied to laser surface treatment enabling to produce a quasi-composite structure of MMCs characterised by the gradient of phase composition as well as functional properties by feeding hard ceramic particles, in particular carbides and oxides, into the surface of the materials produced.
Findings: Valuable and original results were achieved based on the broad scope of the research performed both, in cognitive and applicational terms, concentrated mainly on the analysis and influence of chemical composition and technological heat and surface treatment processes on the structure and properties of the investigated alloys.
Practical implications: The properties of the core and surface layer of the part produced can be customised most advantageously by selecting the part's material and its structure and properties formation processes appropriately along with the surface layer type and technology ensuring the required functional properties.
Originality/value: The knowledge gathered for years concerning light metal alloys, and in particular Mg-Al-Zn alloys, of an undoubtedly valuable cognitive character, is dedicated not only to students but also postgraduates and researches to improve the conditions of education.
Keywords: Materials science; Casting magnesium alloys; Thermal analysis; Heat treatment; CVD and PVD; Laser surface treatment; Computer materials science

Reference to this paper should be given in the following way:
T. Tański, M. Król, L.A. Dobrzański, Sz. Malara, J. Domagała-Dubiel, Precipitation evolution and surface modification of magnesium alloys, Journal of Achievements in Materials and Manufacturing Engineering 61/2 (2013) 87-149.

1. Introduction

Magnesium was discovered by Humphrey Davy - English chemist and physicist. In 1808 the scholar obtained the following elements in the form of amalgams: calcium, strontium, barium and magnesium. Magnesium is one of the lightest metal with density 1.74 g/cm^3, atomic mass 24.31 and silver-grey colour, constituting 2% of the mass of the Earth's crust, which gives it the sixth place among the chemical elements in terms of availability. The magnesium's melting and boiling point amounts to 650 and 1107ºC respectively. The coefficient of linear thermal expansion for magnesium, in the room temperature equals $26 \cdot 10^{-6}$ 1/K [1-3].

Magnesium crystallises in the compact hexagonal network A3, with parameters a=0.321 nm and c=0.521 nm. Below 225ºC dislocation glide on the basal plane {0001} <1120> is only possible in the magnesium's structure, together with twinning on the plane {1012} <1011>. Pure magnesium and conventional magnesium cast alloys indicate tendency for fragility characterised by intercrystalline fracture and local transcrystalline fracture in the twin zones or basal plane {0001} with large grains. Above 225ºC a new basal plane is formed {1011}, causing good deformability of magnesium. The scope of temperature, in which the magnesium may be subject to plastic forming in the easiest way amounts to 350-450ºC [4].

Strength and plastic properties of the pure magnesium are relatively low and depend on its pureness. In the liquid state tensile strength R_m amounts to 80-120 MPa, yield strength R_e=20 MPa, extension A=4-6%, and hardness 30 HB [5,6]. Magnesium as a pure element is distinguished by slight strength and plastic properties. Therefore it is not used as construction material. Advantages of the magnesium, i.e. high heat of combustion, high chemical activity and low density contribute to its use in pyrotechnics, chemical industry, atomic power engineering and metallurgy.

However, magnesium is most frequently used for formation of components from aluminium alloys, where it is added so as to improve the strength and corrosion resistance. It is also used as an addition to zinc alloys so as to improve mechanical properties and dimensional stability [7,8]. Its widest scope of application magnesium achieved while forming light metal alloys in combination with other elements, i.e. aluminium, manganese, zinc, lithium, rare earth elements, copper, calcium, silicon and others.

Until the first half of the previous century magnesium and its alloys were manufactured only for military purposes. In the civil industry due to complicated manufacturing process and high costs of production, they could not compete with substantially cheaper construction materials, despite better mechanical properties. At present due to technological progress in the scope of magnesium alloys (alloys obtained by means of fast-rate quenching - Rapid Solidification Processing, composites based on magnesium matrix - MMCs, namely - Metal-Matrix Composites, casted in the solid-liquid state, rheocasting, thixocasting and thixoforming), forming, thermal treatment, technological improvements and preventing exposition to corrosion, they are more widely in many fields of life [9].

Components casted and being subject to plastic forming, manufactured from magnesium alloys find wide application in automobile industry and mechanical engineering. Slight density with very favourable strength properties enables manufacturing various components on their basis by means of casting method, plastic forming, and mechanical processing as well as welding. High-strength cast alloys with properties identical or very similar to the properties of alloys intended for plastic forming arouse special interest in the contemporary industry of mechanical engineering. Manufacturing of construction components by means of casting technology enables to obtain precise and complex shapes, with high level of material homogeneity and high resistance with a simultaneous good ductility of the alloy, as well as smaller amounts of labour for their execution and relatively low costs of mechanical processing.

Magnesium alloys are construction materials that are widely used in various industry branches, due to low density and high specific strength (in relation to small mass) [6, 10]. In addition, they indicate good corrosion resistance, lack of aggresivity in relation to the mould material and slight melting heat. High ability of damping vibrations and low inertia enable to use the magnesium alloys for fast-moving components at places, where rapid changes of speed take place. Increase of consumption of the magnesium alloys occurred also as a result of progress in manufacturing of new high-strength alloys with addition of Zr, Ce and Cd, very light alloys with Li (they are used in air constructions and spacecrafts) [11].

Mechanical properties of pure magnesium are relatively low, therefore they are not taken into consideration from the constructional point of view, nevertheless they may be improved by introducing additional alloys [12].

The most essential additive in Mg alloys is Al, substantially increasing the tensile strength, particularly by formation of the intermetallic phase $Mg_{17}Al_{12}$. Similar increase of strength may be achieved in the presence zinc and manganese, and addition of silver leads to achievement of good strength properties in the increased temperature [12,13]. High concentration of silicon reduces castability and results in fragility, whereas adding zirconium, due to high affinity for oxygen, causes formation of oxides that constitute crystal nuclei. Due to that the physical properties of Mg alloys are improved by means of dispersion hardening. Adding rare earth elements, i.e. Y, Nd, Ce has become very popular since the time when substantial increase of strength was stated as a result of age hardening. Cu, Ni and Fe are used very rarely due to the fact that they increase the tendency for corrosion, by emission of cathodic compounds during solidification of the alloys. It is one of the reasons why the development of Mg alloys makes its way towards high purity alloys with very low concentration of Fe, Ni and Cu [9,11,14]. Three basic alloying elements in the magnesium alloys are the following ones: Al, Zn and Mn.

Due to chemical composition 5 basic groups of alloys may be distinguished, which are presently manufactured for commercial purposes, based on the main alloying elements such as Al, Mn, Zn, Zr and RE. They are divided into the following subgroups [7,12,15]:

- Mg-Mn,
- Mg-Al-Mn,
- Mg-Al-Zn-Mn,
- Mg-Zr,
- Mg-Zn-Zr,
- Mg-RE-Zr,

- Mg-Ag-Re-Zr,
- Mg-Y-RE-Zr.

Until recently also thorium was a component in the above-mentioned groups of alloys, however due to it hazardous impact the following alloys are presently out of use:

- Mg-Th-Zr,
- Mg-Th-Zn-Zr,
- Mg-Ag-Th-Re-Zr.

Magnesium cast alloys have always dominated over alloys intended for plastic forming, particularly in Europe, where they traditionally comprised 85-90% of products. Al, Zn, and Mn are the earliest used alloy additives, and the alloy Mg-Al-Zn-Mn is still one of the most widely used of cast alloys. Other frequently used additives are zirconium, silicon, cerium and lithium.

At present over 50% of all the components made of magnesium alloys are manufactured by means of pressure casting. This process is characterised by good casting properties. Strength of the pressure-cast alloys may adopt high values, nevertheless the obtained ductility is relatively low. Despite various attempts permeability, which occurs during the process of pressure casting is also a problem. It impedes enhancement of properties by means of thermal treatment and substantially reduces weldability of components made of magnesium alloys [7, 16, 17]. Other 5% of products made of Mg alloys derive from plastic forming processes, performed both as cold and hot forming.

Casts from the magnesium alloys [13, 14, 18] are conducted by means of classical methods, namely:

- sand moulds,
- metal moulds (casting dies),
- under pressure,
- under pressure in cold- and hot-chamber diecasting machines,

as well as by means of modern casting methods:

- by means of pressing method in the liquid state (squeeze casting),
- in solid-liquid state (thixotropic casting),
- by means of low-pressure casting method.

Selection of the specific method depends on many factors, inter alia, requirements and properties of the obtained cast, size and shape of the components, as well as alloy castability.

Both the cast alloys as well as alloys for plastic forming may be processed by means of thermal treatment or not. Thermal treatment of the magnesium alloys in most cases is based on the change in solubility of components in the solid state and solidification of phases with high hardness. Adding alloying elements to magnesium results in formation of terminal solid solutions with decreasing solubility along with reduction of temperature.

Thermal treatment of the magnesium cast alloys consists in [1,8,12,19]:

- homogenisation annealing,
- stress relief annealing,
- recrystallisation annealing,
- age hardening.

The rate of diffusion of the magnesium alloys components is low and execution of their thermal treatment requires quite a long time. Therefore dispersion hardening of these alloys is used more rarely, however it is efficient. Thermal treatment at temperature exceeding 300°C has to take place in inert atmosphere [20,21]. Furnaces intended for thermal treatment of the magnesium alloys should protect the metal against oxidising as airtight as possible. The best results are achieved in electric resistance furnaces with forced air circulation, equipped with devices for introduction of the protective atmosphere, with automatic temperature control as well as heating control [9,14]. Using bath furnaces (salt-cromodising) is also advantageous. Nevertheless, nitric baths are not recommended, due to low level of safety of such a process (oxygen released during decomposition of nitre reacts with metal).

Correct arrangement of the casts is required, so that they would not deform during longer heat soak periods as a result of creeping. Arrangement on the body of the furnace should ensure free access of ambient atmosphere for uniform heating. In addition, casts should be selected in terms of equal thickness of the walls [7,17,22,23].

Conditions of the thermal treatment should be established depending on its type, chemical composition of the alloy, thickness of the walls, degree of the cast complexity, as well as the type of furnace. Rate of heating and soaking depend on cast geometry, thickness of the walls and the type of furnace, whereas the more complex the cast and the higher diversity of its walls' thickness, the slower should be the process. Temperature of the thermal treatment should be established according to the phase diagrams or ready tables for the given alloys [7,24].

In chamber furnaces the rate of heating is relatively low, due to slow exchange of heat. Too intensive heating in the chamber furnace may cause own tensions and formation of cracks. In the liquid heating medium of bath furnaces (melted salts), the heating process takes place much quicker and with high equability [7,11,13,18,25,26].

While developing the casting technologies for magnesium and its alloys, the present engineers focus mainly on the process safety, cost reduction, assurance of the product repeatability and achievement of the highest possible rate of injecting the metal into the mould. Magnesium alloys are very often used in the form of casts, manufactured as a result of solidification of the metallic liquid in the sand or metal moulds, which in turn constitute semi-finished product for manufacturing of plastic-formed products [27,28]. The obtained cast structure has a direct impact on mechanical and technological properties of the final products, therefore proper use of the knowledge on crystallisation and its mechanisms allowing for free control of crystallisation kinetics of the manufactured casts for the purpose of optimisation of the obtained structure and properties is a very essential factor leading to improvement of the quality of the casted products.

Crystallisation kinetics may be characterised by means of several quantities, namely:

- metal temperature,
- rate of quenching,
- rate of cooling,
- rate of generating the hidden heat of crystallisation,
- density of the grain, which is equivalent to density of the developed nuclei,
- participation of the constant fraction of the crystallised metal,
- concentration of components in the remaining liquid,
- characteristic distances and quantities describing shape and size of the structural components.

All these quantities constitute variables of the crystallisation period and geometric coordinates of the cast. The complete characteristics of the crystallisation kinetics may be obtained after combination of the crystallisation equations with the heat exchange equations, and the released heat of crystallisation is the factor combining all the equations and it depends on participation of the crystallised structural components [29].

Changes of temperature, rate of cooling and participation of the constant fraction is determined on the basis of experiments by means thermal or thermal-derivative analysis. Thermal analysis may be conducted immediately before pouring of the alloy into the mould, so as to make possible corrections of quality of the liquid metal e.g.: for the purpose of its subsequent heating or cooling. The curve in the layout: temperature - time, registered during solidification and quenching, allows for assessment of the liquid metal quality and results of its refinement or modification. The course of the hereby curve has characteristic shape, it illustrates interruptions and inflection points enabling to note down changes in the state of matter, transformations in the solid state and to assume the possibility of presence of any defects. The following curves may be distinguished: cooling curve temperature - time TA, differentiation curve DTA and differential cooling curve dT/dt (also known as thermal-derivative analysis). The method of thermal-derivative analysis initially used for assessment of alloy cast iron has also been used in relation to the alloys Cu (Cu-Sn, Cu-Zn, Cu-Al), Al (Al-Si-Cu, Al-Si-Fe, Al-Si-Mg, Al-Si-Cu-Zn) as well as zinc and other nonferrous metals [30-32].

The method of thermal-derivative analysis is very often used both for the scientific research, as well as during the industrial practice, i.e. within the scope of management of the production quality, where it enables quick assessment of concentration of the selected elements in alloys, assessment of certain mechanical and technological properties, which in turn decides about quality of the alloys.

Special advantage of the ATD method is not only the possibility of assessment of the alloy in terms of its chemical composition, but also the possibility of assessment of many details of kinetics of the process of the primary and secondary crystallisation during the same measurement process. Achievement of such amount of information on the material as for example degree of excessive cooling of the liquid, temporary rate of cooling, nucleation temperature, in such a short period (2-5 minutes) enables to make an immediate decision on improvement of the process quality, at the same time allowing for increase of quality of the casting and metallurgical production deciding about the level of reliability of machinery and equipment [33,34].

Dynamic development of the industry sets more and more higher requirements to present products and their components in the context of the anticipated working conditions and existing needs, at the same time supporting and directing progress in the field of material engineering, fostering manufacturing and testing of the new materials. Usable properties of many products and their components depend not only on the possibility of transferring the mechanical loads through the entire active section of the component made of the given material, most frequently subject to thermal treatment, or on its physico-chemical properties, but also very often or mainly on the structure and properties of the surface layers. In such cases economic aspects also impose using surface layers, ensuring required usable properties, with a simultaneous use of possibly cheap materials as core's component, from which other usable properties are generally required. Wide range of the available types of coatings and methods for formation of the structure and properties of the surface layers of the engineering materials, also including magnesium alloys, enables to design the most favourably selected properties of the core and surface layer of the manufactured component in a precise and complex manner. It should be expected that the advanced technologies of surface engineering, particularly including the techniques for applying thin coatings made of hard materials resistant to abrasive wear and corrosion, apart from the required usable properties should at the same time ensure the possibility of forming aesthetic values with undeniably important ecological aspect (the surface coating may not be subject to disintegration, cracks or delamination, should be possibly homogenous and cover the surface tightly, be durable and functional). Among many techniques increasing durability of the engineering materials important role in the industrial and laboratory practice play the methods for Physical Vapour Deposition (PVD), Chemical Vapour Deposition (CVD) and the hybrid methods (multiplex), enabling full control over the composition, structure and properties, making use of the characteristic features of the specific methods, inter alia CVD and PVD as well as conventional thermo-chemical treatment, i.e. heat spraying + thermal treatment, nitriding or glow discharge assisted carbonitriding + Pulsed Laser Deposition method (PLD), chemical, autocatalytic application of coatings + glow discharge assisted treatment.

Large diversity of PVD methods that are used presently depends on the number of factors, i.e. construction solutions of the used equipment as well as physico-chemical phenomena taking place during the process. Among many conditions, which influence the characteristics of the specific PVD methods the following ones should be mentioned: location of the zone for achievement and ionisation of pairs of the deposited material; methods for obtaining pairs of the deposited metals or compounds (evaporation, sublimation, sputtering), application of pairs of material (sputtering - S), (evaporation - E), (ion plating - IP); methods for intensification of layers' deposition (reactive methods, related to the use of reactive gases, activation methods, with activation of the gas ionisation process as well as pairs of par metals by additional phenomena, combined reactive-activation methods, in which various combinations of the given physical process are possible).

Due to concurrence of the coating application processes they are divided into two groups:

- classical application techniques, where application of the pairs of metals takes place in the vacuum (or atmosphere of the non-ionised gas) at clean and cold substrate in typical vacuum evaporation, the application process is usually slow, and the pairs of metal while reaching the substrate have low energy, which is the reason why they cannot dislocate the atoms from the substrate, and deposit on it instead, as a result of which the formed coatings have low density, poor adhesion and relatively high participation of contaminants,
- ionisation vacuum application techniques (most often reactive), which takes place at clean and cold or heated substrate, including many techniques, which may be jointly called ion plating, characterised by bombarding the surface of the applied coating with a stream of ions with the energy

sufficient for making sputtering, influencing the density, tightness and adhesion of the coating to the substrate, as a result of removal of any kinds of contamination atoms, which may also cause heating of the substrate, and even superficial implantation, and also ensures advantageous distribution of own tensions near the boundary substrate-coating.

During the processes of application of coatings by means of PVD methods the most possible homogenous distribution of the specific components of atmosphere inside the working chamber should be obtained and high level of ionisation of the working atmosphere should be ensured, composed of vapours of the applied material and particles of the reactive and working gases. Realisation of both these objectives is ensured variably depending on the used PVD method for formation of coatings.

As far as it is difficult to talk about complicated scheme of configuration in terms of the chemical and quantitative composition in case of on-layer coatings, then in case of complex coatings there are various possibilities. Among the complex coatings particularly the **multicomponent** coatings should be included, in which subnet of one element is partially filled with other element, i.e. carbides and nitrides form with each other continuous constant solutions (three- of four-component) characterised by better properties, particularly tribological, than the simple coatings; there properties may also be controlled by making use of the wide range of the mutual solubility, characteristic for these solutions. While examining complexity of coatings from the quantitative side the **multicomponent** coatings also called multilayer coatings are often cited in literature, which are formed as a result of application of layers of various materials in turn one onto another, most frequently the simple coatings with different properties. The specific layers forming the multicomponent coating should ensure the desired properties, respectively to their location, and while forming the transitional zones between each other they should guarantee smooth passage between frequently variable properties. The internal layer closest to the covered substrate should ensure adequate adhesion do the substrate, the intermediate layer or layers should be characterised by high hardness and strength, whereas the external layer should ensure good tribological, anticorrosion or decorative properties. The **gradient** coatings are the variation of multilayer coatings, varied by the chemical composition and properties of the single layers, smoothly changing at their thickness. In order to form the coatings with good tribological properties several different sources of pairs of metals and gases are frequently used at the same time. Such types of coatings are called **multiphase** coatings, composed of mixture of various phases. Special variations of the multiphase coatings are **composite** coatings, in which one phase is diffused in other coating, occurring in a continuous manner. The coatings that combine diversified properties of the metallic materials with covalent properties are called **metastable** coatings. Such type of coatings are formed as a result of synthesis of the non-equilibrium phases (metastable), e.g. crystallising in the regular system AlN, SiC (when their hexagonal variations are in equilibrium) enabling formation of the solution-strengthened coatings, for example of the type (Ti,Al)N, (Hf,Al)N, (Ti,Si)C and (Ti,Al,Si)N. While considering the division of the coatings that are complex in terms of their structure and size of crystallites, from which they are composed the **nanometric** coatings should be mentioned, in case of which the size of crystallites does not exceed 10 nm.

Continuous evolution of PVD methods heads in the direction of improvement of adhesion of the coatings, the result of which is rapid development of the techniques guaranteeing diffusion-adhesion combinations, namely the high-temperature techniques ensuring the highest energy of ions and atoms used for constitution of the coating, as well as in the direction of manufacturing of surface gradient materials [35, 36]. The examples of gradient coatings manufactured by PVD methods, which are also used for covering of the tested magnesium cast alloys Mg-Al-Zn are as follows:

- **$Ti_{1-x}Al_xN$** obtained by means of gradual change of tension of the substrate polarisation during the process of application of the coatings or change of working parameters of the device, where the concentration of aluminium x changes from the substrate to the external surface of the layer as a result of more intensive attraction of the titanium particles ionised by the substrate, to which higher negative tension was applied and which influences the change of the ratio of concentration of Ti and Al in the coating,
- **$Ti(C_xN_{1-x})$** - where the concentration x of carbon and as a consequence of nitrogen changes smoothly from the substrate to the surface of the layer as a result of the controlled change of concentration of N_2 and CH_4 during the application process,
- **$Ti_xAl_ySi_{1-(x+y)}N$** - where the concentration x of titanium and concentration y of aluminium, and as a consequence of silicon changes smoothly, respectively to the surface of the layer as a result of regulation of the conditions for application,
- **(Ti,Al,Si)N and (Al,Ti,Si)N** - where the change of the properties and structure from the substrate to the external surface of the layer is obtained by use of variable “shields” during the application process.

Rapid development of the PVD processes caused use of the specific properties of coatings at an industrial scale, not only for covering of the tool materials [37, 38], but also in other application fields, including inter alia for improvement of the properties of Mg alloys, to which relate inter alia own works [39, 40]. Hard coatings resistant to wear are more frequently used for improvement of properties and functionality of various usable materials. PVD coatings find their use in optics and microelectronics, biomedicine, aeronautics and space industry, power engineering, automobile industry, construction and housing industry and mechanical engineering. Increase of durability, limitation of the rate of wear, resistance to high temperature, low thermal conductivity coefficient and limitation of oxidising and corrosive processes have mainly decided about the use of the coating obtained during PVD processes for covering of many engineering materials. In case of using the coatings obtained by means of PVD methods, the requirements set for them mainly relate to not decreasing the mechanical properties of the substrate by the coatings and improving the tribological and anticorrosive properties, depending on the intended use of the coatings.

Above all, the coatings undoubtedly owe their favourable properties to strongly defective, fine crystalline and sometimes even amorphous structure and smaller size of the grain [35,36,41]. The technical conditions of the process of application of the coatings, such as: pressure of the gases in the furnace chamber, accelerating voltage (substrate polarisation), process temperature, distance between the substrate and the source of the deposited

material, as well as the chemical composition of coatings causing achievement of the desired properties also have a great impact.

Technologies of the physical deposition from the gas phase belong to the most commonly used methods for processing of the construction surface of the engineering materials [42-45].

Another surface engineering technology that is successfully used for processing of the magnesium alloys are laser technologies. The first laser presented in 1960 was specified as "invention that will have no use in practice". However, within the course of enhancement of laser technologies and their application possibilities the expressed words lost their value. At present many fields of science and technology make use of the possibilities carried by the use of laser, as for example: material technologies, precise measurements, control of the operations of working machinery, precise positioning of the folded constructions, medicine and biology, military techniques, holography, optical telecommunication and many other. Special attention among the above-mentioned ones should be paid to the laser surface processing of various materials, which allows for formation of the surface layer with the thickness from the decimal part of millimetre up to several millimetres and with special usable properties, high hardness and abrasion resistance, with simultaneous preservation of invariable properties of the substrate material. After proper selection of the processing conditions the components may be manufactured "ready for use", without the necessity of further finishing. Due to very precise supply of energy, non-contactness and full automation, laser technologies gain increasing importance of application. The global industry has already been using laser techniques in the wide range, and the broadest industrial application in the laser material processing have presently the solid lasers with active crystalline component, inter alia Nd:YAG, Yb:YAG, among which due to geometry of the applied active medium bar and disc lasers may be distinguished. In addition, CO_2 gas laser should be mentioned, as well as diode lasers, fibre-optic lasers, i.e. fibre lasers (included by some experts to solid-state lasers) with impulse or constant laser beam power, reaching as much as 100 kW [46-50].

HPDL lasers are made of many single diode emitters with GaAs, which are arranged in the so-called diode bars with the cross-section 0.6x0.115 mm and length 11 mm [51]. The diode bars are completed into packets, which in the next step are mounted in the copper body that is intensively cooled by water. Standard diode packets with the dimensions 182x130x272 mm ensure laser power up to 2.0 kW. In the high power diodes the alloy GaAs doped with Al, In or P is the semiconductor material, whereas the laser radiation is generated at the area of the connection of contact surface of the doped material p and n, as a result of recombination of electrons and holes. In the semiconductor GaAs (the source of photon radiation), at the state of equilibrium of the load carriers, electrons and holes their excess is limited only to the n and p type areas, which is caused by large difference of potentials at the contact area. Application of additional positive voltage to the p area, and the negative voltage to the n area results in reduction of potentials to the level, in which free flow of electrons and holes by p-n connections takes place and the process of recombination of electrons and holes occurs. The flow of current through the semiconductor takes place as a result of passage of greater number of loads to the area of p-n connection and exchange of loads that are subject to recombination. The excess of energy generated during the recombination process is released in the form of thermal laser radiation.

In order to obtain the possibly smallest laser spot, it is required to use special optical systems and short focal lengths due to substantial astigmatism of the laser beam. Special technology for construction of the packets of diode lasers intensively cooled by water results in obtaining high power in the diode lasers.

The material after laser processing conducted with the use of HPDL laser indicates the properties different from the ones conducted with the use of other high power lasers, and particularly is characterised by more homogenous melted zone and smaller surface roughness. Such advantages result from the unique properties of HPDL laser, i.e. high efficiency, approx. 30-50% (laser with power of 2.0 kW uses along with the laser cooling system 7.5 kW), very high radiation absorption coefficient, as well as linear shape of the beam of laser radiation. Moreover, the HPDL lasers are distinguished by relatively low price, high durability (above 10 000 h), do not require additional service apart from cleaning of the optical system, are easy to operate and mobile.

At present the high power diode lasers are used inter alia for soldering, hardening, welding, remelting, alloying, fusion, as well as for various applications of the surface processing of the metal alloys, also including the magnesium alloys.

Mutual intensive mixing of the materials (matrix, strengthening) takes place in the pool as a result of convectional and gravitational movements and as a result of pressure of the laser beam [52, 53].

The characteristic feature of the laser alloying process is the occurrence of high temperature gradient at the border of the melted layer and substrate, which as a result leads to rapid quenching and solidification of the liquid metal. The rate of cooling obtained within these conditions reach 10^{11} K/s, whereas the rate of solidification repeatedly exceeds 20 m/s, which in case of certain materials may cause self-hardening of the thin layer of the substrate material [54, 55].

The surface layer obtained in the laser alloying process indicates the structure and properties that are different in comparison to the structure and properties of the substrate material and the alloying material. Morphology of the obtained quasi-composite layer is distinguished by large homogeneity and correct dispersion of the particles introduced into the entire melting depth, except for the very thin layer of diffusion saturation.

The properties of the alloyed surface layer depend on the substrate, alloying material and the parameters of the alloying process, nevertheless the obtained surface layer almost always rich with the alloying components is distinguished by hardness, fatigue strength and better tribological and anticorrosion properties that are greater than the substrate's, with a simultaneous increase of roughness, at the result of which processing is frequently performed on the components after alloying, aiming at smoothening of the surface.

The following parameters decide about the conditions of the laser alloying process: power density of the laser beam and the time of exposure of the laser beam to the material, which oscillates between the thousand and decimal parts of the second. Proper selection of these conditions ensures the required geometrical features and mechanical properties of the obtained surface layer. Along with increase of the power density of the laser beam or decrease of the scanning rate the thickness of the obtained layer rises, in case of lower power density of the laser

beam or greater scanning rates the alloying depth, and as a result also the thickness of the formed surface layer decreases. These values should be included in the proper range, as in case of too excessive power density of the laser beam or too lower scanning rate, the alloyed material begins to sublime, leaving slight pits on the surface. If the power density of the laser beam is too low or if the scanning rate is too high, the structure of the alloyed layer may turn out to be nonuniform. Proper selection of the alloying material according to the substrate is also important, due to the temperature of melting and sublimation, which for the purpose of homogeneous mixing should be included in the narrow range of values. Plasma and material evaporation generally occur during melting.

Plasma impacts the remelting in two ways, on the one hand it screens the pool against further absorption of energy from the laser beam, by which it inhibits sublimation, whereas on the other hand it leads to mixing of the melted components by means of pressure. What is more, the laser beam causes formation of the funnel cavity in the pool of the liquid metal, which is ionised gas, and the continuously disturbed, unsteady equilibrium is maintained at the border liquid metal - plasma. In order to control the influence of plasma on the pool of liquid metal, various technological methods for its activation or neutralisation are applied. One of the methods for limitation of influence of plasma on the pool of liquid metal is blowing plasma cloud by the stream of the inert gas. The introduced gas (e.g. argon) is often additionally heated, which prevents deterioration of the energetic effect. Whereas intensification of the plasma impact is conducted by means of blowing of the plasma cloud, but with a simultaneous repeated directing of the primarily reflected laser radiation to the processing zone by the system of flat mirrors or mirror bowl [51-55].

Development of the advanced information technology tools, including the methods of artificial intelligence, numerical methods, mathematical modelling and computational intelligence makes that they are more commonly used in various fields of science and technology. These trends have also been noticeable in the field of material engineering for many years, due to wide application possibilities, enabling to solve new issues, as well as those regarded as the classical ones. Both modelling as well as computer simulation allow for full integration of the knowledge on the materials science IT tools, at the same time ensuring model compatibility after simulation with the results of the experiment, substantially eliminating the necessity of conducting expensive and time-consuming experimental studies in favour of the computer simulation, which has also been confirmed within the scope of own tests. Therefore it seems to be obvious that the intelligent prediction with the use of the artificial intelligence tools is a further step bringing the present engineer closer towards the better understanding of the matter of their research.

In material engineering various types of calculation methods are used, allowing for approximation and prediction of the phenomena taking place in the materials during manufacturing, technological processing and exploitation of the engineering materials in different working conditions. Among the techniques used in the generally defined computer assistance (CAx) the stochastic methods may be included e.g. Monte Carlo method, numerical methods for solving mathematical equations e.g. finite element method (FEM), widely understood artificial intelligence methods e.g. genetic algorithms, artificial neural networks or fuzzy logic. Increasingly popular are the hybrid systems combining several methods, so as to obtain the results that reflect the actual phenomena by far considerable extent. Numerical methods are also used in other fields of knowledge and it would be very difficult now to indicate at least one field of science, in which the application possibilities of the computer assistance have not been used.

Neural networks constitute the numerical modelling technique, able of mapping the complex functions. At present the neural networks have non-linear character, which allows the user for free and easy formation of the non-linear models, describing the features of the modelled objects. An advantage of the neural networks is the fact that they enable to look for numerical models for unfamiliar phenomena and processes, where the network user does not have to declare in advance any required form of the searched model, and even does not have to be sure that any mathematically describable dependency exists [56-61].

Neural networks constitute mapping of the basic structures that are present in brain. Based on the anatomical studies carried out on a human brain it results that the brain mainly consists of very large number of elementary nerve cells - neurons. Artificial neuron constitutes the basic elementary cell of neural network. While making attempt to map the basic assumptions of functioning of the biological nervous systems the inventors of the neural networks defined the artificial neuron in the following way:

- certain number of input signals reaches the neuron. These are the values of the primary data, transmitted to the network from the outside as data for calculations conducted in the network or indirect signals coming from the outputs of other neurons comprising the network,
- all the values are introduced to the neuron by means of connection with a certain weight; such weights have to correspond to the value of synapse in the biological neuron,
- every neuron also has a single threshold value, specifying how strong its stimulation has to be so that it would come up to its activation,
- the weighted sum of inputs is calculated in the neuron (which denotes the sum of values of the inlet signals multiplied by proper weighting coefficients), and they the threshold value is subtracted from the sum. The additional value obtained by such a method specifies neuron simulation,
- the signal representing the total neuron simulation is transformed by the set function of neuron activation (which is also called sometimes as a function of neuron transition). The value is calculated by the activation functions constitutes the final initial value of the neuron [62].

Single neurons may be grouped into layers in such a way, so that they all could have joint input signals. Every layer has so many outputs as the number of neurons that it holds. All the layers may be connected to each other by outputs while constructing multilayer neural network. Among the neural layers building the neural network the following may be distinguished: input layer, hidden layers and output layer [56,63,64].

Input layer receives the data from the outside of the network. The number of neurons in this layer is strictly determined by the number of input variables, which have to be taken into consideration while solving a specific task. Neurons in this layer do not have their own inputs and do not perform any data

processing. Size of the output signal in this layer is specified by the value of the input signal of the network.

Output layer generates output signal of the network constituting the solution to the tasks established for the network. The number of neurons in this layer depends on the number of the required tasks. The output signal of the output neurons is a function of input signals coming from the input layer (in case of two-layer networks) or hidden layer (L-1) (in case of multilayer network) [57,63,65]. The results delivered by the output layer always have approximate character. Accuracy of this signal may be diverse, however the accuracy of many significant digits cannot be guaranteed.

Results of multiplication may be adopted as very good, is the accuracy of the answer is better than two significant digits (error in such a case amounts up to several per cent). Due to such limitations the tasks should be defined in such a way so that the answer could have "character of classification" to a proper category - for example it could be required that the network would specify whether the nucleation temperature of the alloy ACAlSi7Cu4 after adding 2% Cu "will slightly increase", "will increase substantially", "will be constant", "will slightly decrease", "will decrease substantially" [64].

Hidden layers form additional structure processing input signals (received by the input layer) in such a manner that the output layer could find the required answer in easier way. The effect of functioning of the neurons in the hidden layers reveals only indirectly, by the value of the answer that is sent to the neurons of the output layer.

Characteristic feature of the neural networks is the possibility of teaching them by means of the so-called learning algorithms, which enable adaptation of the network parameters to the specificity of the problem being solved. The degree of complexity of the neural network and efficiency of learning characterise the learning algorithms. The applied learning algorithms determine the basic division of the neural networks due to the learning methods. Two types of learning algorithms are distinguished:

- algorithms realising supervised learning - with a teacher. Such algorithms modify the weights and threshold values making use of the learning data sets including both the input values as well as the required output values,
- algorithms realising unsupervised learning - without any teacher. Such algorithms modify the weights and threshold values making use of the learning data sets including only the input values (in case of such algorithms the output values in the data sets are not required, and in case of their occurrence they are ignored) [56,57,64,65].

In order to compare and verify the correctness of the results obtained on the basis of the tests the computer analysis has been conducted, enabling determination and/or prediction of the phenomena taking place in the materials, including in the magnesium cast alloys Mg-Al-Zn, with the use of the neural networks. Within the scope of the computer simulations the following has been carried out: modelling of the selected parameters of the structure and mechanical properties on the basis of the temperature of the phase transformations and the rate of cooling, optimisation of the conditions of the heat treatment, as well as determination of the roughness range and modelling of the mechanical properties of the surfaces of the magnesium alloys processed by means of laser fusion.

2. Experimental procedure

2.1. Materials and their heat treatment

The influence of the thermal treatment (precipitation hardening) on the structure and properties of the magnesium cast alloys was analysed on the basis of the following magnesium cast alloys MCMgAl12Zn1, MCMgAl9Zn1, MCMgAl6Zn1, MCMgAl3Zn1 with a chemical composition given in Table 1.

Casting of the alloys was conducted in the crucible induction furnace Flux 12 with the use of protective bath, equipped with two ceramic filters with the used melting temperature adequate for the manufactured material 750±10°C. Due to preserving the metallurgical cleanliness of the melted metal, refinement by means of the inert gas with an industrial name Emgesalem Flux 12 was performed. For the purpose of improvement of the quality of the alloy surface, the protective layer Alkon M62 was used. The material was poured into the dies with bentonite filler material due to advantageous sorption properties and formed in the shape of plates with the dimensions 250x150x25. The casted alloys were subject to thermal treatment in the electric vacuum furnace Classic 0816 Vak in the protective atmosphere of argon.

The applied thermal treatment was according to the established scheme (Tab. 2).

Table 1.
Chemical composition of analysed magnesium alloys

The mass concentration of elements of analysed alloys, %						
Al	Zn	Mn	Si	Fe	Mg	Reszta
12.1	0.62	0.17	0.047	0.013	86.96	0.09
9.09	0.77	0.21	0.037	0.011	89.79	0.092
5.92	0.49	0.15	0.037	0.007	93.33	0.066
2.96	0.23	0.09	0.029	0.006	96.65	0.035

Table 2.
Conditions of the heat treatment of tested alloys

Indication of the heat treatment	Heat treatment		
	Temperature, °C	Time, h	Cooling method
0	As-cast		
1 - solutioning	430	10	water
2 - solutioning	430	10	air
3 - solutioning	430	10	furnace
4 - aging	190	15	air

The newly-developed multicomponent magnesium cast alloys Mg-Al-Zn with a diversified concentration of the alloying components, and particularly aluminium, changing in the range from 3 up to 12%, as well as Zn and Mn, with a constant

concentration of micro additives Pb, Ce, Zr, Sn and Be, ensuring achievement of the required structure at the raw condition and after thermal treatment, was manufactured during the process of casting to the sand moulds.

2.2. Thermal analysis of magnesium alloys

Thermal-derivative analysis was performed based on the example of the alloys Mg-Al-Zn (Tab. 1) with the use of the UMSA device (Universal Metallurgical Symulator and Analyzer) presented in figure 1 [66-73]. Performance of the thermal analysis with the use of UMSA device consisted in melting, soaking and quenching of the sample with correctly assumed quenching rate. The samples in the shape and dimensions presented in Figure 2 were inductively heated up to the temperature 700±1°C with the use of the induction coil (Fig. 2, par. 2) fed by the generator of the induction device (Fig. 1, par. 3) with maximum power of 5 kW. Melting was conducted in a tightly closed chamber, to which protective gas was supplied in the form of argon with a flow rate 2.4 l/min, so as to avoid self-ignition of the magnesium alloy. In order to achieve appropriate quenching rates of the tested material, the samples were cooled by means of argon supplied by the nozzles situated at the coil (Fig. 2, par. 2). The flow rate of the argon quenching the sample was controlled by control and measurement system, functioning based on the principle of measurement of the temperature of the flowing gas on the inlet and outlet of the valve. The flow of the gas was selected experimentally and applied to the entire experiment.

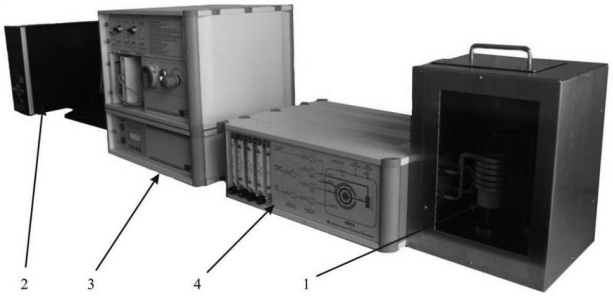

Fig. 1. UMSA device: (1) sample chamber, (2) supervisory computer, (3) temperature control, (4) gas flow control

The rate of quenching was calculated based on the dependence:

$$CR = \left(\frac{T_{Liq} - T_{Sol}}{t_{Sol} - t_{Liq}} \right) \qquad \left(\frac{^{o}C}{s} \right) \tag{1}$$

where:
T_{Liq} -liquidus temperature,
T_{Sol} -solidus temperature,
t_{sol} - time registered at the moment when solidus temperature was reached,
t_{Liq} - time registered at the moment when liquidus temperature was reached.

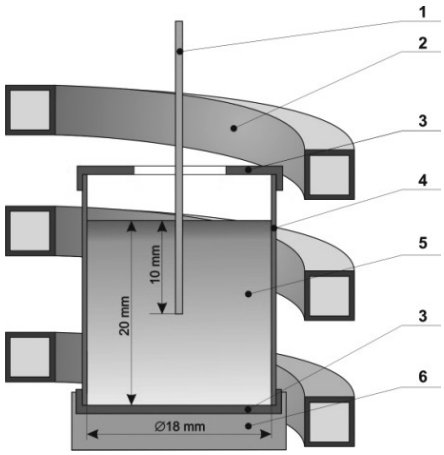

Fig. 2. Schematic of the UMSA Thermal Analysis Platform experimental set-up: 1 - low thermal mass thermocouple, 2 - heating and cooling coil, 3 - thermal insulation, 4 - steel foil, 5 - test sample, 6 - ceramic base

For the purpose of obtaining the rate of quenching:

- ≈ 0.6°C/s the sample was quenched with no forced quenching,
- ≈ 1.2°C/s argon with a flow rate of 30 l/min was flowing through the quenching system,
- ≈ 2.4°C/s argon with a flow rate of 125 l/min was flowing through the quenching system.

In order to establish the dependence between the temperature and time of the structural changes, liquidus and solidus temperature, temperature of eutectic nucleation and the phase containing Mn and Al and the phase Mg_2Si for the given alloy, three complete cycles of melting and solidification of the samples were performed. The first melting ensured very good contact of the thermoelement with the sample's metal, the second and the third one constitute the proper experiment guaranteeing repeatability of the test results.

On the basis of the thermal-derivative analysis characteristic points describing thermal phenomena taking place during alloy crystallisation were determined, defining the values of temperature and time read from the curves of thermal-derivative analysis. An exemplary curve of thermal-derivative analysis with marked points describing thermal phenomena was presented in Figures 3 and 4 and in Table 3. The points of the characteristic transformations occurring during crystallisation were specified as the points of tangent at the place of cutting the base curve by the curve. Designation of the adopted points was presented in Table 3 and the abbreviated method of their determination in Table 4.

While projecting the determined points on the quenching curve, and then on the axis of ordinates and abscissae, the temperatures and periods of formation and solidification of the specific phases during crystallisation were respectively designated. In addition, based on the selected values characterising the differential curve, the latent heat of crystallisation of the specific phases was calculated.

It was assumed that the thermal capacity - $c_p(t)$, of crystallisation of the alloy is a function of time, hence it depends on participation of the solid state, thermal capacity in the liquid state c_{pLiq} and thermal capacity in the solid state c_{pSol}. Thermal capacity

of the alloy during the time was calculated based on the following dependence:

$$c_p(t) = c_{p_{Sol}} \cdot \int_{t_N}^{t} f_s(t)dt + c_{p_{Liq}} \cdot \left(1 - \int_{t_N}^{t} f_s(t)dt\right) \quad (2)$$

where:
f_s - participation of the solid phase, assuming that for $f_s(t \le t_N) = 0$ and $f_s(t \ge t_N) = 1$.

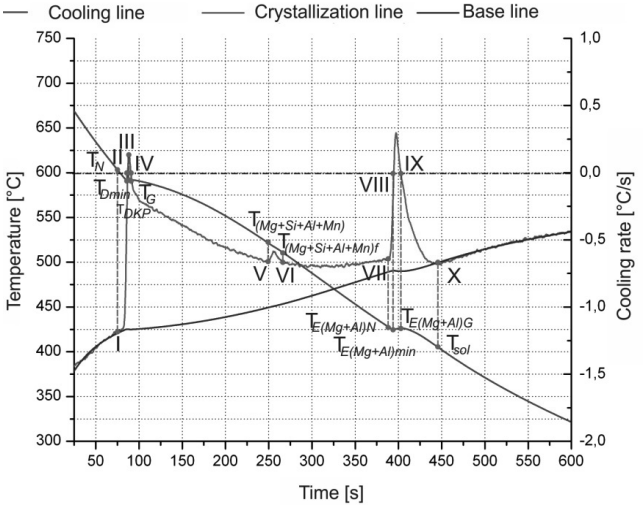

Fig. 3. Representative thermo-derivative curve of MCMgAl9Zn1 magnesium alloy

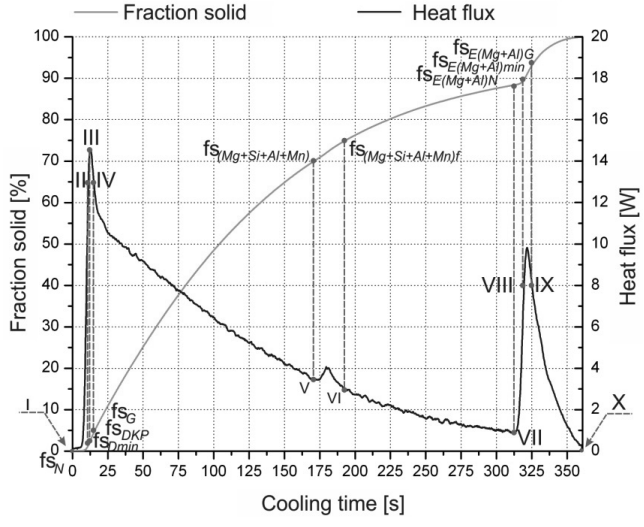

Fig. 4. Representative curves illustrate changes of heat flux and fraction solid of MC MgAl6Zn1

Table 3.
Characteristic points obtained from thermal-derivative analysis

Point	Temperature	Description
I	T_N	Nucleation of α-phase (liquidus temperature)
II	T_{Dmin}	The α-Mg dendrite minimum (undercooling) temperature
III	T_{DKP}	Coherency point
IV	T_G	The α-Mg dendrite growth temperature
V	$T_{(Mg+Si+Al+Mn)}$	Crystallization of α-Mg, Mg_2Si and phases contains Al and Mn
VI	$T_{(Mg+Si+Al+Mn)f}$	End of crystallization of Mg_2Si and phases contains Al and Mn
VII	$T_{E(Mg+Al)N}$	Beginning of nucleation of α(Mg)-γ ($Mg_{17}Al_{12}$) eutectic
VIII	$T_{E(Mg+Al)min}$	The α(Mg)- γ ($Mg_{17}Al_{12}$) minimum (undercooling) temperature
IX	$T_{E(Mg+Al)G}$	The α(Mg)- γ ($Mg_{17}Al_{12}$) eutectic growth temperature
X	T_{sol}	End of solidification (solidus temperature)

Table 4.
Methods of determining the characteristic points of thermoderivative curve

Point	Description	Way in which the point was designated
I	α nucleation temperature	The point of intersection of the tangent line drawn a straight line curve section of the base curve of crystallization
II	α-Mg dendrite minimum temperature	The value of the first derivative equal to zero
III	Coherency point	The first derivative achieves a maximum value
IV	The α-Mg dendrite growth temperature	The first derivative reaches zero again
VIII	The α(Mg)- γ ($Mg_{17}Al_{12}$) minimum (undercooling) temperature	The value of the first derivative equal to zero
IX	The α(Mg)- γ ($Mg_{17}Al_{12}$) eutectic growth temperature	The first derivative reaches zero again
X	Solidus temperature	Crystallization curve overlaps with a base curve

Thermal capacity in the liquid state c_{pLiq} and thermal capacity in the solid state c_{pSol} was calculated based on the chemical compositions presented in Table 1 with the use of the program Thermo-Calc Software [74].

The entire latent heat of crystallisation of the tested alloys was calculated based on the dependence [75-78]:

$$Q = c_p \cdot m \cdot \int_{t_N}^{t_{sol}} \left[\frac{dT}{dt} - \left(\frac{dT}{dt} \right)_c \right] \quad (3)$$

where:
c_p - thermal capacity of the alloy,
m - sample mass, kg.

2.3. Structure and properties of the coatings on the substrate from the Mg-Al-Zn alloys applied from the gas phases by means of chemical and physical CVD and PVD methods

In order to establish the dependence between the structure and properties of the applied hybrid coatings, namely the system soft substrate - gradient transition layer, with a liquid change of one or several of its components from the substrate of its external surface - and the external coating, coverings were conducted in the process of cathodic evaporation by the electric arc and in the process of chemical deposition from the gas phase with plasma assistance on the substrate from the magnesium cast alloys Mg-Al-Zn, with the following configuration: Ti/TiCN/CrN, Ti/TiCN/TiAlN, Cr/CrN/CrN, Cr/CrN/TiN, Ti/TiSiN/TiSiN and Ti/DLC/DLC [39,79].

Due to specificity of the material such as magnesium alloys, and in particular due to their low melting temperature the coating application process was performed in the range up to 180°C [35,36,40] with the use of two methods: chemical deposition with plasma assisted CVD (PACVD) and PVD cathodic arc evaporation (CAE). The PACVD process, in which relatively low temperature of surface processing may be obtained, was used for manufacturing of the carbon coatings type DLC in the atmosphere of acetylene C_2H_2 and with a set pressure. The second method was realised with the use of the DREVA ARC400 device of the German company Vakuumtechnik with a cathodic arc evaporation method. The device is equipped with three independent sources of metal pairs. Before application of the coatings the substrates were chemically cleaned with the use of the washing and irrigating process in ultrasonic cleaners and cascade washing machines and dried with a stream of hot air. Moreover, they were cleaned with the use of Ar ions with a voltage of substrate polarisation 800/200 V during 20 min. The discs of the diameter 65 mm, cooled by water, containing pure metals (Cr, Ti) and alloys TiAl and TiSi were used for application of the coatings by means of PVD method. The coatings were applied in the atmosphere of the inert Ar gas and the reactive N_2 gases, so as to achieve nitrides and the mixture N_2 and C_2H_2 for the purpose of obtaining carbonitride layers. The gradient change of the concentration of the chemical composition on the cross section of the layers was achieved by the change of dose ratios for the reactive gases or change of voltage of the evaporation current of the discs on the arc sources. The set conditions of the coating application process were listed in the Table 5. During the PVD layer application process the substrates made of the magnesium cast alloys moved against the sources of pairs, making rotary movements, so as to obtain coatings with uniform thickness and at the same time preventing occurrence of the phenomenon of the so-called smudge on the coated surfaces.

Table 5.
The deposition conditions studied layers

Coating parameters	Type of the achieved coating and the applied coating technique					
	PVD					CVD
	Ti/Ti(C.N)-gradient/CrN	Ti/Ti(C.N)-gradient/(Ti.Al)N	Cr/CrN-gradient/CrN	Cr/CrN-gradient/TiN	Ti/(Ti.Si)N-gradient/(Ti.Si)N	Ti/DLC-gradient/DLC
Base pressure [Pa]	$5x10^{-3}$	5×10^{-3}	5×10^{-3}	$5x10^{-3}$	$5x10^{-3}$	$1x10^{-3}$
Working pressure [Pa]	0.9/1.1-1.9/2.2	0.9/1.1-1.9/2.8	1.0/1.4-2.3/2.2	1.0/1.4-2.3/2.2	0.89/1.5-2.9/2.9	2
Argon flow rate measurement, cm^3/min	80*	80*	80*	80*	80*	80*
	10**	10**	80**	80**	20**	-
	10***	10***	20***	20***	20***	-
Nitrogen flow rate measurement, cm^3/min	225→0**	0→225**	0→250**	0→250**	0→300**	-
	250***	350***	250***	250***		
Acetylene flow rate measurement, cm^3/min	0→170**	140→0**	-	-		230
Substrate bias voltage, V	70*	70*	60*	60*	70*	500
	70**	70**	60**	60**	100**	
	60***	70***	60***	100***	100***	
Target current, A	60	60	60	60	60	-
Process temperature, ºC	<150	<150	<150	<150	<150	<180

Table 6.
Properties of used powders

Property		WC	TiC	VC	NbC	SiC	TaC	Al_2O_3
Density, kg/m^3		15.69	4.25	5.36	7.6	3.44	15.03	3.97
Hardness, HV		3400	1550	2850	2100	1600	1725	2300
Melt temperature, °C		2870	3140	2830	3500	1900	3880	2047
Grain sieze, µm	min.	0.7-0.9	< 1.0		<10	<10	<10	1-5
	max.	>5	>6.4	>1.8	<45	<75	<45	80

2.4. Laser treatment of magnesium alloys

Analysis of the surface processing impact with the HPDL laser was conducted on the magnesium cast alloys Mg-Al-Zn, in the surface of which titanium, tungsten, vanadium, niobium, silicon and tantalum carbides and aluminium oxides were fused (Tab. 6).

Laser treatment of the magnesium cast alloys (fusion) was performed by means of the technique of feeding the powder in a continuous manner to the melted pool area by dosing the powder with the use of fluidisation feeder. The powder feeder was connected to the transporting gas cylinder and powder-feeding nozzle. In the powder-feeding system the rate of feeding of the transporting gas amounted to 5 [l/min].

After initial trial runs the laser power within range 1.2-2.0 kW and rate of fusion of 0.25; 0.50; 0.75; 1.00 m/min were adopted for the tests. The tests indicated that the optimum geometry of the single laser path was obtained during fusion with the rate of 0.75 m/min, except for the Al_2O_3 and NbC powders, for which the optimum rate was respectively set as 0.50 m/min and 0.25 m/min.

As a result of appropriate selection of the fusion conditions it is possible to achieve on the surface a uniform composite made of matrix (Mg alloy) and hard ceramic particles fused. While specifying the product conditions several essential factors have to be taken into account, among which the most important ones are as follows: difference of the density between the particles of the applied carbides or oxide (TiC, WC, VC, SiC, NbC, Al_2O_3) and the alloy matrix; as well as the difference of absorption of the beam's energy between the applied powders and magnesium cast alloys Mg-Al-Zn.

Fusion of the carbide powders and Al_2O_3 into the magnesium cast alloys MCMgAl12Zn1, MCMgAl9Zn1, MCMgAl6Zn1 and MCMgAl3Zn1 took place with the use of HPDL laser Rofin DL 020 (Tab. 7). The used laser is a high-power universal device, used in the material engineering, inter alia for surfacing, welding, melting and surface fusion. The used laser composed of inter alia: working rotary Table moving in the XY plane, nozzle with powder feeder for enrichment or surfacing, protective gas nozzle, laser head, feeding and cooling systems, and computer system controlling the laser's operation and location of the rotary Table.

The fusion was conducted in the argon shield, in order to protect the substrate against oxidising. The sample that was subject to laser fusion was located in the protective gas shield blown from the two nozzles, one directed pivotally to the laser processed sample, and the second one directed perpendicularly to the pool area. The flow rate of the shielding gas (Argon 5.0) amounted to 12 l/min. The distance of the nozzle from the sample did not exceed 20 mm.

Table 7.
Technical data of HPDL Rofin DL 020

Wavelength, nm	808-940
Power range, W	100-2000
Focal length, mm	82
Power density range, kW/cm²	0.8-36.5
Laser beam spot dimensions, mm	1.8 x 6.8

On one surface of the perpendicularly situated samples one or two paths were executed after laser fusion, with diverse laser power and rate of fusion.

2.5. Neural networks

Selection of the optimum conditions for the thermal treatment for the tested magnesium cast alloys was conducted with the use of computer analysis, including the neural networks.

The applied neural network enabled to develop the model of dependence between:

- concentration of aluminium, temperature and time of saturation, cooling medium, and hardness,
- concentration of aluminium, temperature and time of saturation, temperature and time of aging, and hardness.

The set of data for saturation and aging was divided at random into three subsets: learning, validation and test. In case of the network calculating hardness after saturation the number of cases amounted to respectively: 68, 20, 20, whereas in case of network calculating hardness after aging 231, 100, 101.

Data from the learning set were used for modification of the network weights, data from the validation set for the network assessment during the learning process, whereas the other part of values (test set) was intended for independent specification of the network efficiency after full accomplishment of the procedure for its formation. The results used during the process of learning and testing of the network were subject to normalisation. Calibration was used towards deviation from the minimum value in accordance with the mini-max function. The mini-max function transforms the field of variables to the interval (0,1). The type of networks, number of neurons in the hidden layer (layers), method

and learning parameters were specified while observing the influence of these quantities on the adopted evaluation indicators for network quality.

The following quantities were used as the basic evaluation indicators for the model quality:

- mean network prognosis error,
- standard deviation quotient,
- Pearson correlation coefficient.

The standard deviation quotient was adopted as an essential quality indicator for the model built with the use of the neural network for the errors and data. Correctness of the model adopted by the network may be considered only when the prognoses presented by the network are subject to smaller error than the simple estimation of the unknown output value. The easiest way to estimate the output value is to adopt the mean value from the output data for the learning set and to present it as a prognosis for the data not presented during the learning process. In this case the mean error is equal to the standard deviation for the output value in the learning set, and the standard deviation quotient adopts value amounting to one. The smaller the network prediction error, the lower values the standard deviation quotient adopts, reaching zero for the "perfect" prognosis. The one-direction network type MLP (multilayer perceptron) with one hidden layer and 5 neurons in it was set as optimum, both for the network calculating hardness after saturation and aging. The applied error function and logistic activation function was adopted in the form of sum of squares, using the learning method based on the conjugate gradient algorithm, which allowed for presentation of the examples from the learning set through the 101 training epochs for the network calculating hardness after saturation and 195 epochs the network calculating hardness after aging.

Neural networks were also applied for determination of the temperature of phase transformations based on the mass concentration of aluminium and the quenching rate. Simulation of the cast processes requires knowledge of the specific temperature values, therefore neural network models were developed, using which the value of the specific temperature may be calculated based on the mass concentration of aluminium and rate of quenching. One-direction networks type MLP with 2 neurons in the input layer were developed for calculation of the nucleation temperature of the α phase, maximum nucleation temperature of the α phase and solidus temperature. The minimax variable conversion technique was applied for the input and output data. The number of the network layers was specified as three layers with 8 neurons in the hidden layer. Activation functions in the input and output layers were specified as linear with saturation, in case of the layer hidden as the logistic, whereas the linear PSP functions were applied for all the layers. The networks were taught with the methods of backpropagation (50 learning epochs) and conjugate gradients (23 learning epochs) for the network determining the temperature T_N, with backpropagation method (50 learning epochs) and conjugate gradients (3 learning epochs) for the network determining the temperature T_G and with backpropagation method (50 learning epochs) and conjugate gradients (73 learning epochs) for the network determining the temperature T_{sol}.

Neural network were also used so as to determine the mechanical properties of the surface layers after laser surface processing with the set: mass concentration of aluminium, rate of fusion, laser power and types of the particles fused. Three regression characteristics were the basis for assessment of the network quality: mean absolute error, standard deviation quotient and Pearson correlation coefficient. The standard deviation quotient is the measuring instrument for the model quality used for solving regression problems. It is determined as standard deviation quotient of predication errors and standard deviation quotient of the initial variable. The lower value of the measuring instrument, inversely proportional to the variance indicates the better predication value.

In the first instance the neural network was designed after calculation of hardness based on laser fusion parameters. Experimental data were used for the design, making allowance for the type of the applied powder, concentration of aluminium in the alloy, laser power and rate of fusion - as initial variables - and HRF hardness - as initial variable. The set of data was divided into subsets: learning (48 cases), validation (23 cases) and test (24 cases).

As a result of design and optimisation one-direction network type MLP (multilayer perceptron) was selected, with 4 neurons in the input layer - corresponding to the input variables: type of the applied powder (nominal variable), concentration of aluminium in the alloy, laser power and rate of fusion (numerical variables) and one numerical output variable (HRF hardness). Conversion method One-of-N was applied for the nominal input variable, and for the numerical input variables and the output variable the minimax variable conversion method was used. The number of the network layers was specified as three layers with 2 neurons in the hidden layer. Activation function in the input and output layers was specified as linear with saturation, and in the hidden layer as logistic, whereas the linear PSP functions were used for all the layers. The networks were taught with the methods of backpropagation (50 learning epochs) and conjugate gradients (62 learning epochs).

In Table 8 the error values, standard deviation quotients and correlation coefficients of the designed neural network were presented, which constituted the basis for the network evaluation.

Table 8.
Regression statistics of neural network calculating hardness value in data sets

Indicators of quality evaluation model	Data set		
	Training	Validating	Testing
Average error, HRF	5.35	6.49	5.90
Quotient of the standard deviations	0.43	0.44	0.46
Pearson's correlation coefficient	0.90	0.90	0.89

Similarly to calculation of hardness of the surface layer after laser fusion, the neural network for calculation of roughness of the surface layer was also developed. Experimental data were used so as to build the network model, making allowance for the type of the applied powder, concentration of aluminium in the alloy, laser power and rate of fusion - as input variables - and roughness R_a - as output variable. The set of data was divided into three subsets: learning (61 cases), validation (22 cases) and test (22 cases). Three regression characteristics constituted the basis for the assessment of the network quality: mean absolute error, standard deviation quotient and Pearson correlation coefficient.

As a result of design and optimisation one-direction network type MLP (multilayer perceptron) was selected, with 4 neurons in the input layer - corresponding to the input variables: type of the applied powder (nominal variable), concentration of aluminium in the alloy, laser power and rate of fusion (numerical variables) and one numerical output variable (roughness R_a). Conversion method One-of-N was applied for the nominal input variable, and for the numerical input variables and the output variable the minimax variable conversion method was used. The number of the network layers was specified as three layers with 5 neurons in the hidden layer. Activation function in the input and output layers was specified as linear with saturation, and in the hidden layer as logistic, whereas the linear PSP functions were used for all the layers. The networks were taught with the methods of backpropagation (50 learning epochs) and conjugate gradients (59 learning epochs).

3. Results and discussion

3.1. Structure and properties of Mg-Al-Zn heat treated alloys

The results of the metallographic examinations made using light and scanning microscopy (Figs. 5-16), as well as based on the analysis of surface distribution of elements and X-ray quantitative microanalysis, and X-ray phase analysis (Figs. 17-19, Table 9) indicate that the casting magnesium alloys: MCMgAl12Zn1, MCMgAl9Zn1, MCMgAl6Zn1, MCMgAl3Zn1 in their cast state are characterized by microstructure typical for solid solution α, constituting the alloy matrix, and an intermetallic phase γ - $Mg_{17}Al_{12}$ in a lamellar form, localized mainly at grain boundaries). Moreover, in the vicinity of intermetallic separation phase γ, the presence of acicular eutectic form was revealed (α + γ).

In the structure of the examined cast magnesium alloys, in addition to $Mg_{17}Al_{12}$ phase of separations, gray phases can also be observed, characterized by angular contours with smooth edges in the form of hexagonal-shaped particles (Figs. 7, 8). Based on results of the chemical composition using energy-dispersive X-ray spectroscopy (EDS Figs. 18, 19, Table 9), and the literature data, it was found that it is the Mg_2Si phase which, while separating, increases hardness of the casts.

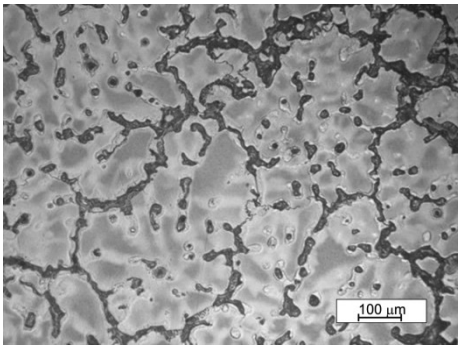

Fig. 5. Structure of MCMgAl12Zn1 in as-cast state

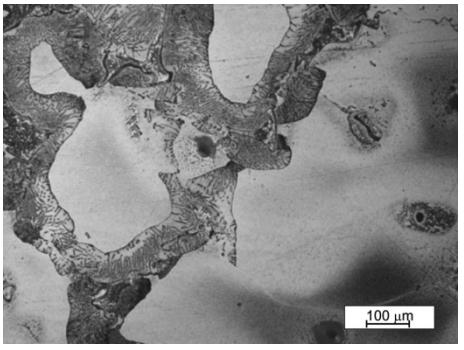

Fig. 6. Structure of MCMgAl9Zn1 in as-cast state

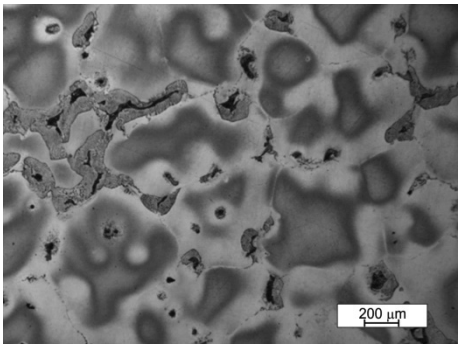

Fig. 7. Structure of MCMgAl6Zn1 in as-cast state

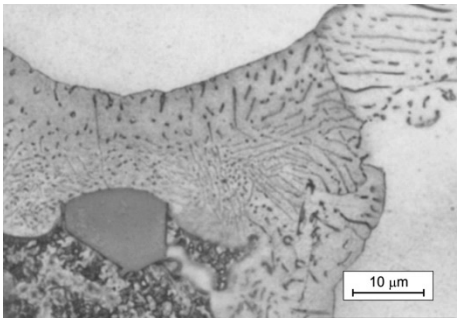

Fig. 8. Structure of MCMgAl9Zn1 in as-cast state

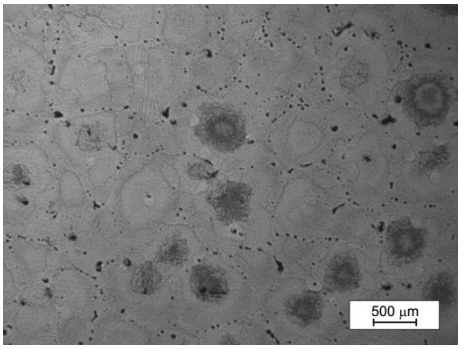

Fig. 9. Structure of MCMgAl3Zn1 after solutioning with cooling in air

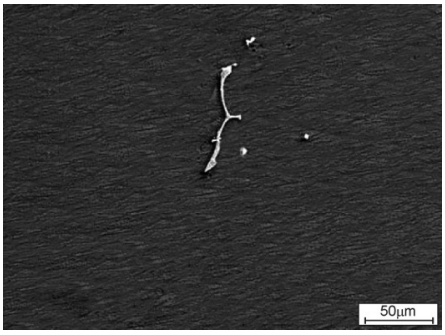

Fig. 10. Structure of MCMgAl3Zn1 after solutioning with cooling in air

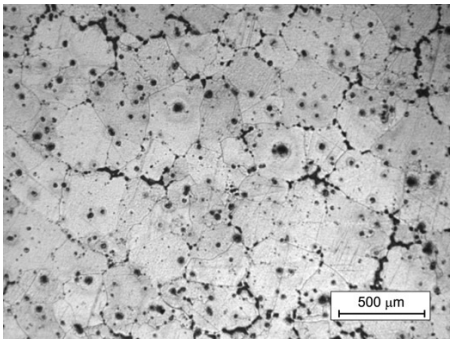

Fig. 11. Structure of MCMgAl12Zn1 after solutioning with cooling in water

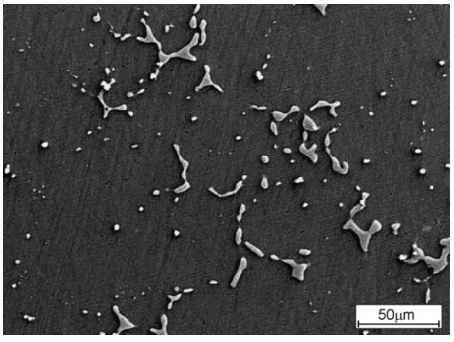

Fig. 12. Structure of MCMgAl12Zn1 after solutioning with cooling in water

As a result of the study of surface distribution of elements, and the X-ray quantitative microanalysis taken using energy-dispersive X-ray spectroscopy the presence of the main alloying elements, i.e., Al, Mn, Zn was confirmed, as well as Fe and Si included in the cast magnesium alloys in the cast state, and after heat treatment (Figs. 18, 17, Table 9), and information was obtained about the mass and atomic concentration of each element in the spot tested microareas of the matrix and separations. In addition, confirmation of introduction of Pb, Ce and Cu into the alloy identified in the γ phase was also obtained (Fig. 19, Tab. 9).

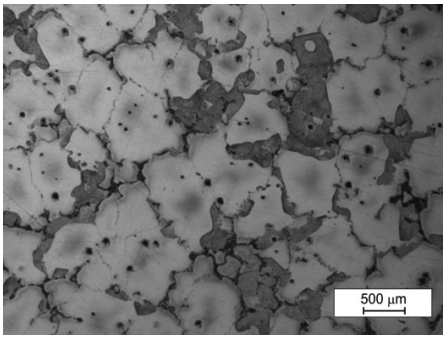

Fig. 13. Structure of MCMgAl9Zn1 after solutioning with cooling in furnace

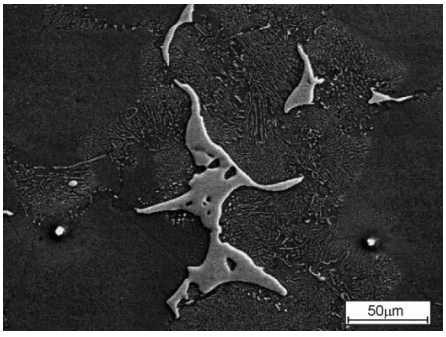

Fig. 14. Structure of MCMgAl9Zn1 after solutioning with cooling in furnace

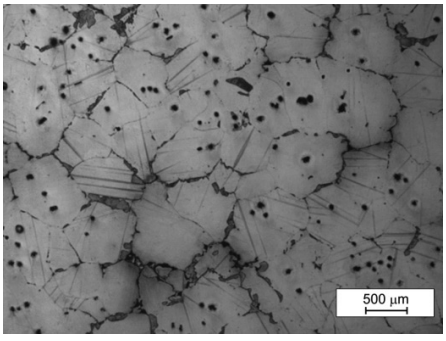

Fig. 15. Structure of MCMgAl9Zn1 after aging treatment

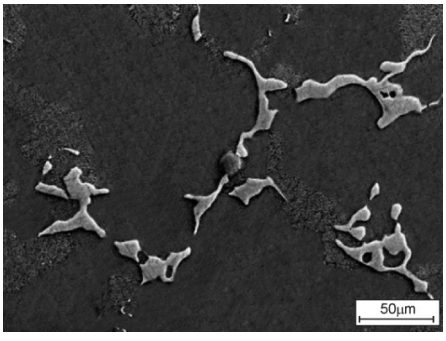

Fig. 16. Structure of MCMgAl9Zn1 after aging treatment

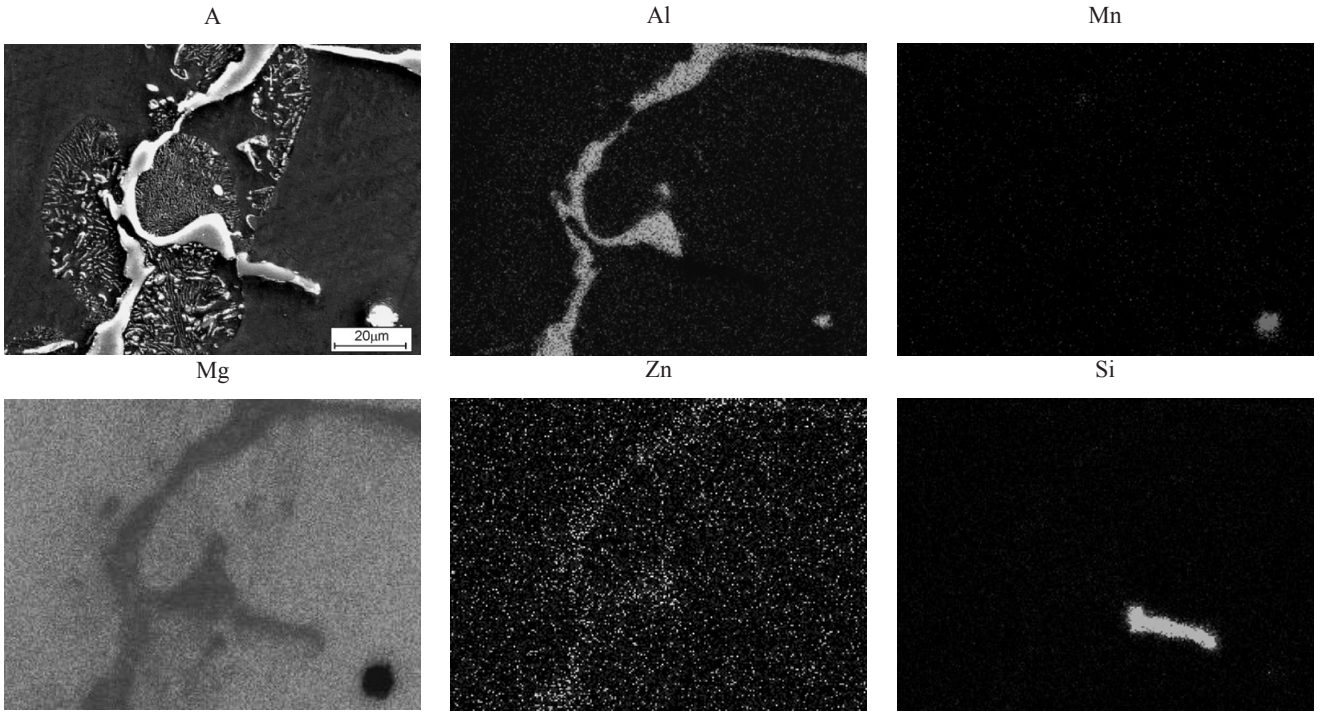

Fig. 17. The area analysis of chemical elements alloy MCMgAl6Zn1 after cooling in furnace: image of secondary electrons (A) and maps of elements' distribution

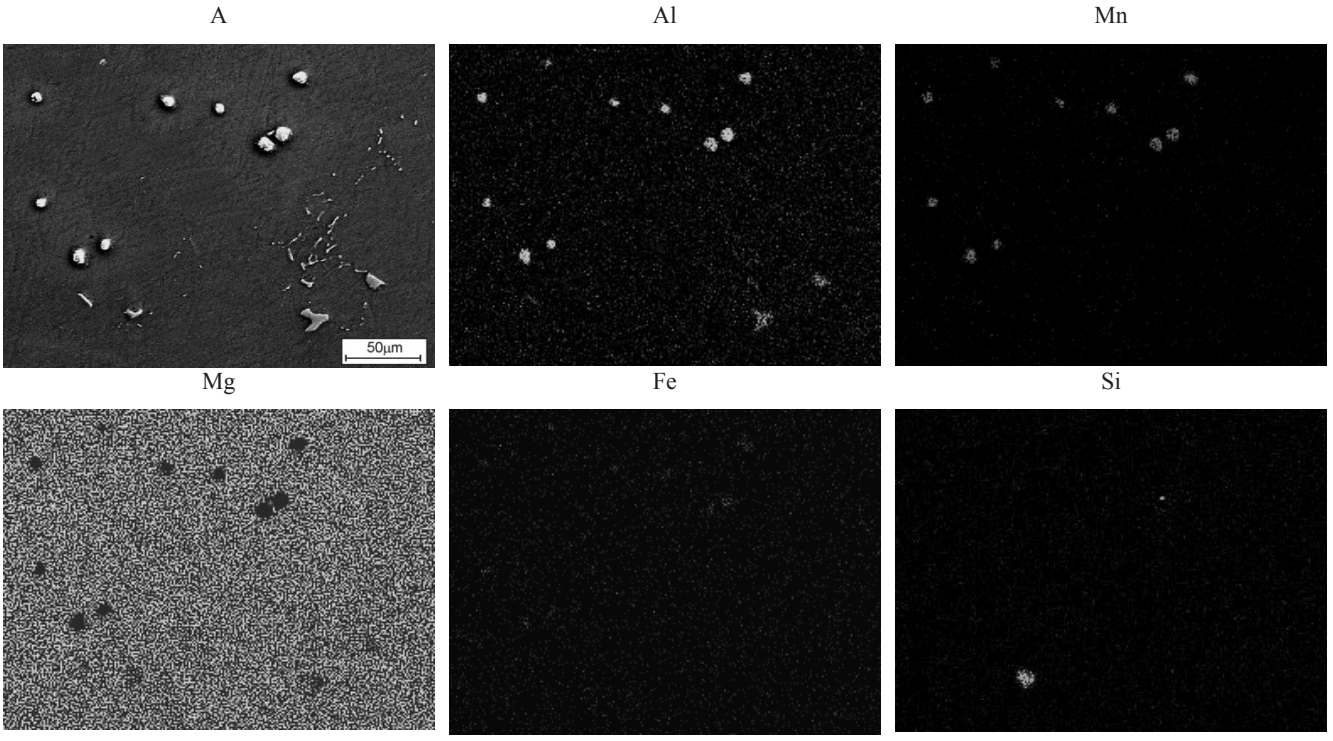

Fig. 18. The area analysis of chemical elements alloy MCMgAl6Zn1 after cooling in air: image of secondary electrons (A) and maps of elements' distribution

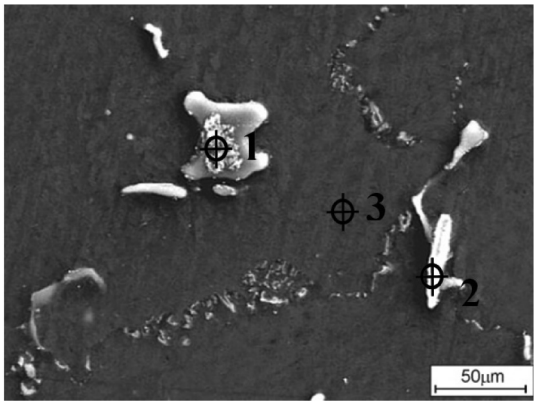

Fig. 19. Structure of MCMgAl6Zn1 after solutioning with cooling in furnace

Table 9.
Results of the quantitative analysis of chemical composition magnesium cast alloy MCMgAl6Zn1 after cooling in the furnace

Element	The concentration of main element, %	
	Mass	Atomic
Analysis 1		
Mg	51.23	61.63
Al	24.36	29.25
Zn	5.54	5.23
Mn	0.11	0.06
Si	0.17	0.2
Fe	0.08	0.05
Cu	0.72	0.36
Pb	17.79	3.22
Analysis 2		
Al	50.32	60.88
Mn	37.05	34.53
Zn	0.78	0.28
Si	0.46	0.3
Fe	0.4	0.11
Cu	0.39	0.2
Pb	0.57	0.21
Ce	10.03	3.49
Analysis 3		
Mg	91.89	93.14
Al	6.94	6.34
Zn	0.86	0.23
Ni	0.07	0.03
Ce	0.11	0.02
Cu	0.13	0.05

Following solutioning and cooling in water and air, in MCMgAl9Zn1, MCMgAl6Zn1, MCMgAl3Zn1 alloys, the trace presence of γ phase ($Mg_{17}Al_{12}$) was noted in the structure, as well as single Mg -Si phase separations, and Mn-Al-Fe phase, often occurring in spheroidal or acicular forms. Eutectic separations have not been noted in the structure (Figs. 9 and 10). On the other hand, in the MCMgAl12Zn1 alloy several areas of γ phase and eutectics not dissolved in solid solution were observed (Figs. 11 and 12).

Following solutioning and cooling in the furnace, the structure of solid solution α was revealed in materials MCMgAl12Zn1, MCMgAl9Zn1, MCMgAl6Zn1 areas of γ secretion from with numerous areas of the secondary γ phase separation (eutectic-like morphology areas), moreover, γ phase separation was also observed ($Mg_{17}Al_{12}$) located at grain boundaries, and a light gray phase usually located within the γ phase grain boundaries (Figs. 13, 14). The MCMgAl3Zn1 alloy, after solutioning and cooling in the furnace, is characterized by few γ phase separations, unevenly distributed in the structure.

Using aging with cooling in air after solutioning causes separation of evenly distributed $Mg_{17}Al_{12}$ phase dispersive particles, occurring also in the form of pseudoeutectic areas *) (Figs. 15, 16).

Both in the matrix alloy as well as the eutectic area and in the areas of large separations formed at the borderlines of phases identified as $Mg_{17}Al_{12}$, prevalence of magnesium and aluminium was noted, as well as low concentration of Zn (Fig. 17).

Chemical analysis of surface elements distribution, and quantitative microanalysis of transverse microsections of magnesium alloy casts done by EDS also points at the marked increase in concentration of magnesium, silicon, and aluminium, manganese and iron in certain areas, which indicates the occurrence of separations in the alloy structure containing Mg and Si, characterized by angular contours and phases with a high concentration of Mn and Al with irregular structure, frequently occurring spheroidal or acicular forms (Figs. 17 and 18).

Figure 20 shows X-ray diffractograms of tested magnesium alloys after heat treatment. Using of X-ray phase analysis of qualitative and quantitative methods, it was found that in the tested materials there is a phase γ ($Mg_{17}Al_{12}$) and a phase α-Mg constituting the matrix of alloys. Volume shares of the phase separations γ in the alloy structures of: MCMgAl12Zn1, MCMgAl9Zn1, MCMgAl6Zn1 depend on the concentration of aluminium introduced as the primary alloying addition, assuming its maximum value of 11.9 % for the MCMgAl12Zn1 alloy in the state after aging and the minimum value - 1.6 % for MCMgAl9Zn1 alloys in the state after aging and MCMgAl6Zn1 alloys after casting.

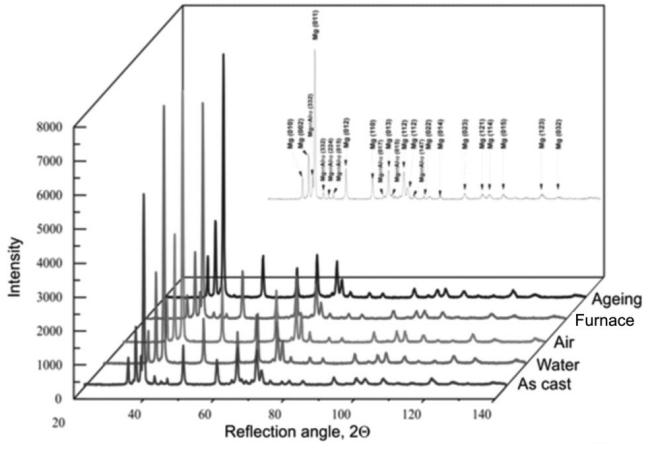

Fig. 20. X ray diffraction pattern of the MCMgAl9Zn1 magnesium cast alloy

Too small volume share of other phases present in the material, as well as phases γ -$Mg_{17}Al_{12}$ for cases alloys after oversaturation or at low concentration of aluminium: MCMgAl9Zn1, MCMgAl6Zn1, MCMgAl3Zn1, does not allow for their clear identification on X-ray diffractograms.

As a result of tests on thin film in a transmission electron microscope, it was found that the structure of the newly developed experimental MCMgAl12Zn1 cast of magnesium alloys, MCMgAl9Zn1, MCMgAl6Zn1, MCMgAl3Zn1 in the state after oversaturation consists is a supersaturated solid solution of α-Mg. In the supersaturated solid solution there are low density dislocations (Fig. 21). Tests performed on thin films of alloys after aging demonstrate that the structure of magnesium alloy casts in the state is a solid solution of α-Mg with evenly spaced secondary phase separations γ -$Mg_{17}Al_{12}$ (Figs. 23, 24). In the solid solution, consisting a matrix of magnesium alloy casts after aging, there are dislocations forming clusters and tangled networks with a much higher density as compared to the solutioning condition (Fig. 22). Generating these dislocations is probably connected to tension produced in the matrix by separating intermetallic phase particles $Mg_{17}Al_{12}$. Dispersive separations present in the separation of the solid solution in aged magnesium alloys have, in most of the cases, a preferential crystallographic orientation with the matrix. Some of them (Figs. 23, 24) show the following relationships:

$$(1\,\bar{1}\,01)\ \alpha\text{-Mg} \parallel (10\,\bar{1})\ Mg_{17}Al_{12}$$
$$[11\,\bar{2}\,0]\ \alpha\text{-Mg} \parallel [111]\ Mg_{17}Al_{12}$$

as given by S. Guldberg and N. Ryum [80] for those also present in the eutectic structure of Mg alloys containing 33% Al. Some separations of the investigated supersaturated and aged magnesium alloys exhibit an orientation in which the plane of the {110} $Mg_{17}Al_{12}$ family are deflected at about 10° from the planes from family {$1\,\bar{1}\,01$}solid solution of α-Mg (Fig. 24), while others are even more deflected from a dependant given by S. Guldberg and N. Ryum [80]. Solidification of phase γ -$Mg_{17}Al_{12}$ are usually shaped as rods and lamellae, and the dominant direction of growth are directions typical or family <110> α–Mg (Figs. 23, 24).

As a result of tests of micro areas on thin films of the alloy MCMgAl9Zn1 (Fig. 25) by radiation quantitative microanalysis using EDS energy-dispersive X-ray spectroscopy, it was found that part of the phase causing aging of the magnesium alloys is primarily Mg (more than 84% in atomic count), and aluminium (15% in atomic count). High concentrations of magnesium and aluminium is also maintained in the alloy matrix assuming the value of, respectively, ~90% Mg in atomic count and Al ~10 % in atomic count.

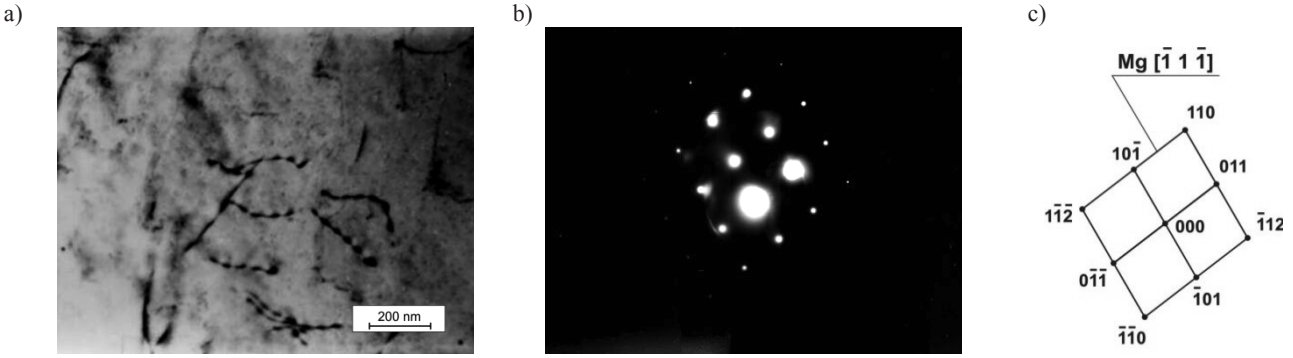

Fig. 21. TEM images of the MCMgAl9Zn1 alloy after solutioning at 430°C in 10 h and cooled in water: a) bright field; b) diffraction pattern of area shown in a); c) part of solution for diffraction pattern shown in b

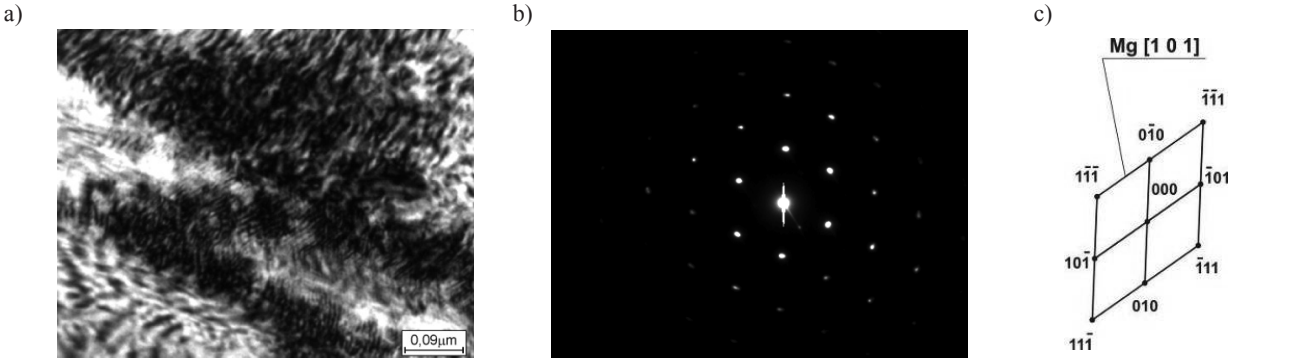

Fig. 22. TEM images of the MCMgAl9Zn1 alloy aging: a) bright field; b) diffraction pattern of area shown in a); c) part of solution for diffraction pattern shown in b

a)

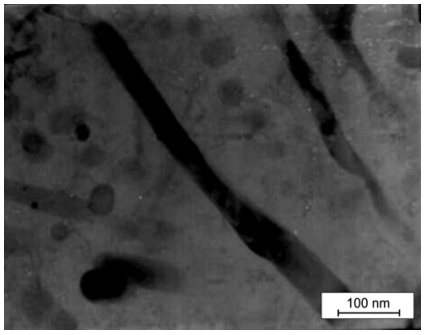

b)

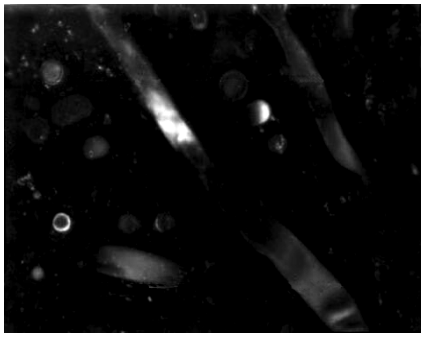

c)

d)

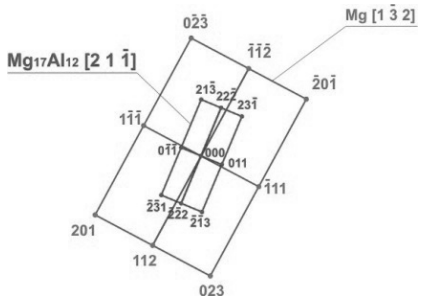

Fig. 23. TEM images of the MCMgAl9Zn1 alloy after aging at 190°C in 15 h and cooled in air: a) bright field; b) dark field with reflex ($21\bar{3}$) $Mg_{17}Al_{12}$ phases c) diffraction pattern of area shown in a); d) part of solution for diffraction pattern shown in c

a)

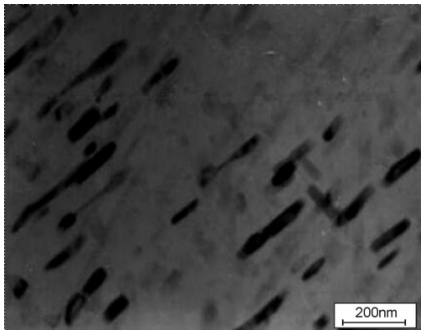

b)

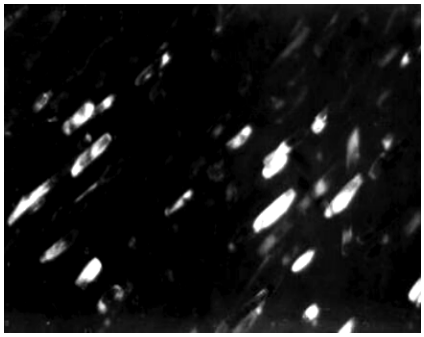

c)

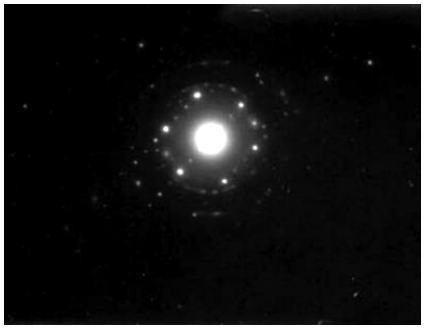

d)

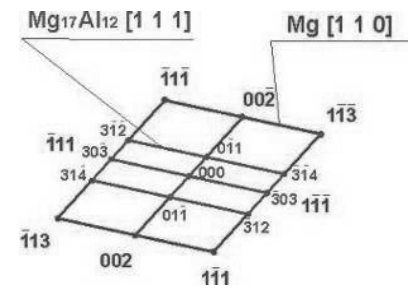

Fig. 24. TEM images of the MCMgAl9Zn1 alloy after aging at 190°C in 15 h and cooled in air: a) bright field; b) dark field with reflex ($\bar{3}\bar{1}4$) $Mg_{17}Al_{12}$ phases c) diffraction pattern of area shown in c); d) part of solution for diffraction pattern shown in c

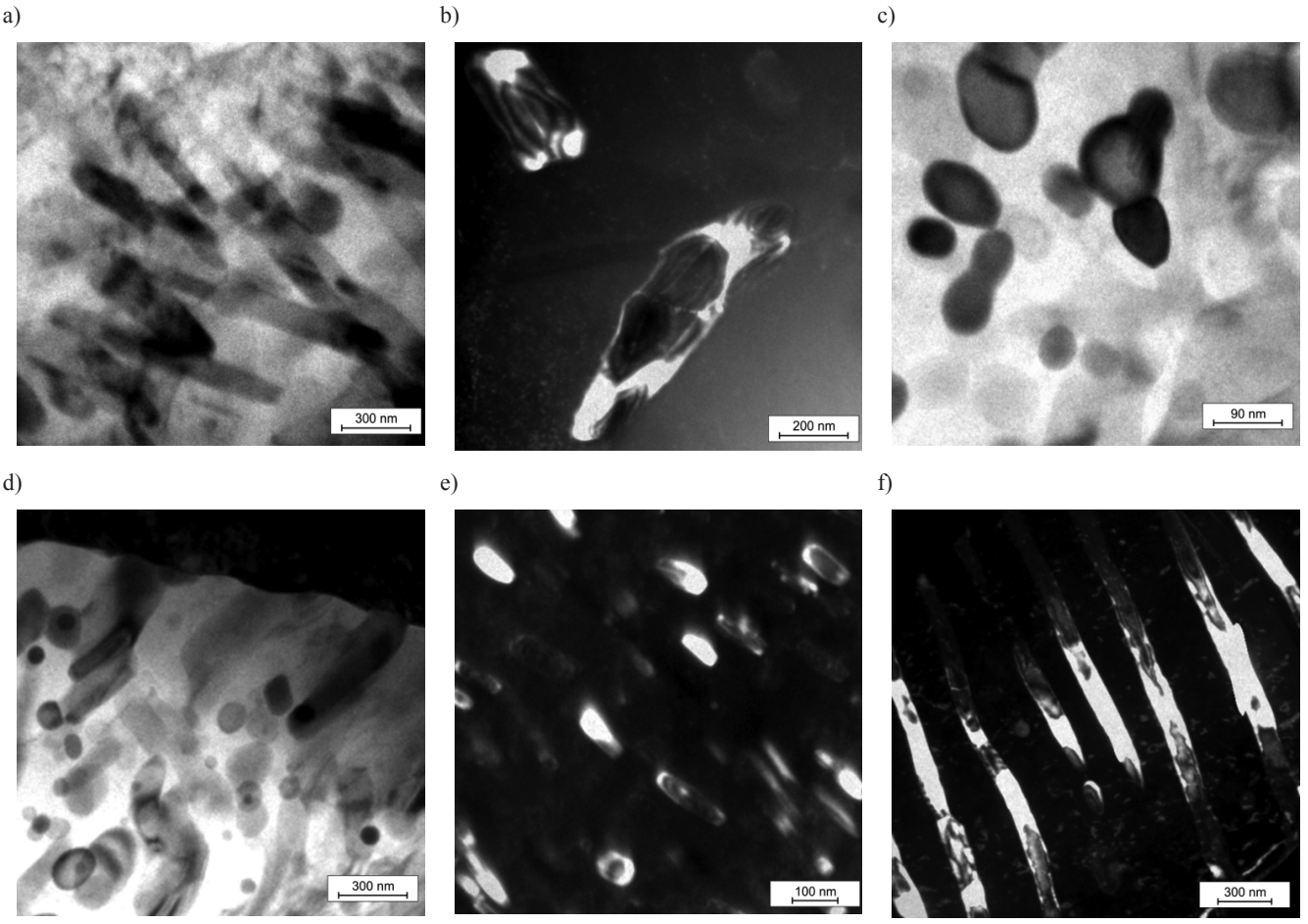

Fig. 25. Representative TEM pictures of MCMgAl9Zn1 cast magnesium alloy after aging in 190°C at 15h and cooled in air with visible γ-$Mg_{17}Al_{12}$ a) ,b), c), d) bright fields, e) ,f) dark fields

With a view of a better characterization of the effect of heat treatment and aluminium concentration on magnesium alloy casting, pictures were taken of fracture structures after a static tensile test, presented in Figures 26-29. The studies found that the MCMgAl12Zn1, MCMgAl9Zn1 andMCMgAl6Zn1 alloys, when cast are characterized by mixed fractures, and in the case of MCMgAl3Zn1 alloys, a ductile fracture can be clearly seen (Fig. 26). Subjecting alloys to heat-treatment by means of solutioning and water and air cooling has increased plasticity of the alloys, as can be seen in the majority of cases in the ductility of most of the fractures, and an increase in the values of narrowing and elongation (Fig. 27). On the other hand, MCMgAl12Zn1 alloys, heated and cooled in the furnace, and subjected to aging, and MCMgAl9Zn1 alloys, heated and cooled in the furnace, where there has been a noticeable increase in hardness compared to baseline and a slight decrease in the values of the narrowing and elongation exhibit a brittle fracture (Fig. 28). In alloys cast from MCMgAl6Zn1 and MCMgAl3Zn1, a mixed fracture has been found (Fig. 29).

Surface morphology of the test samples after corrosion test in the state before and after heat treatment show numerous pitting and cracks of the surface layer of the material with irregular shape (Fig. 30-35), in the largest number noticeable in the case of oversaturation and cooling with the furnace, developing around solidifications, which causes surface discontinuity and, consequently, large weight loss (Figure 31). MCMgAl6Zn1 and MCMgAl3Zn1 casting magnesium alloys are characterized by the smallest visible destruction of the surface layer (Fig. 33-35).

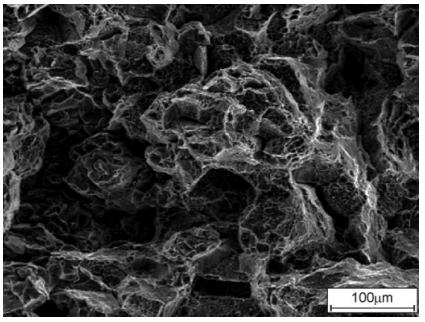

Fig. 26. The fracture surface of MCMgAl3Zn1 as-cast state

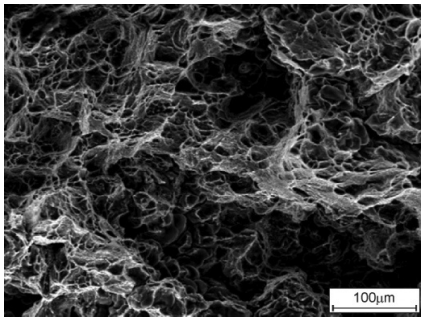

Fig. 27. The fracture surface of MCMgAl9Zn1 after solutioning and cooled in air

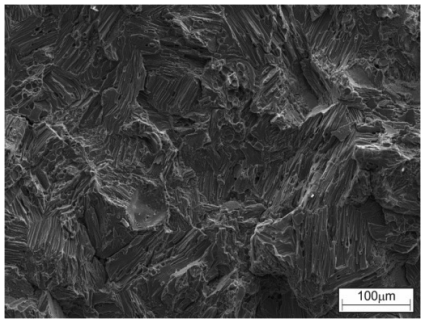

Fig. 28. The fracture surface of MCMgAl12Zn1 after solutioning

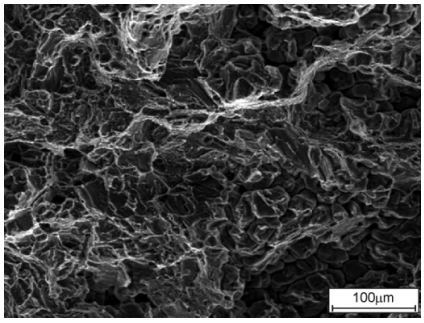

Fig. 29. The fracture surface of MCMgAl6Zn1 after solutioning and cooled with furnace

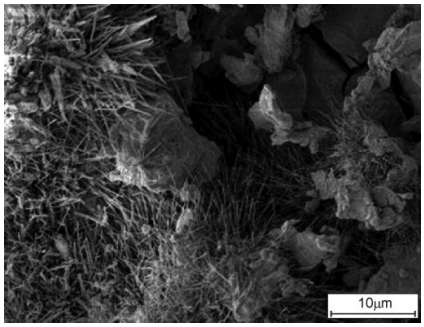

Fig. 30. Surface structure of MCMgAl12Zn1 after solutioning and cooled in air after corrosion test

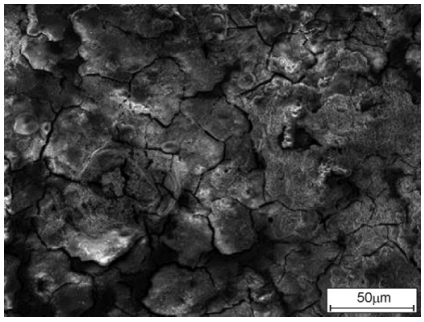

Fig. 31. Surface structure of MCMgAl12Zn1 after solutioning and cooled in air after corrosion test

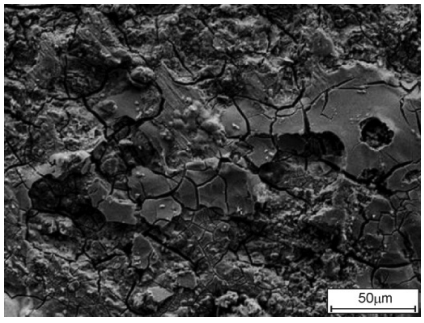

Fig. 32. Surface structure of MCMgAl9Zn1 after corrosion test

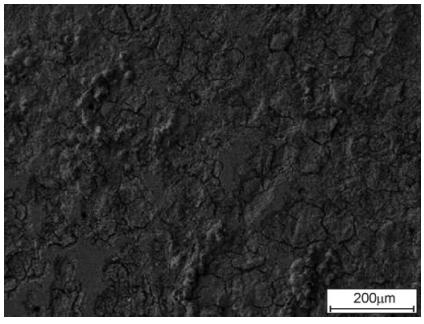

Fig. 33. Surface structure of MCMgAl6Zn1 after solutioning and cooled in water after corrosion test

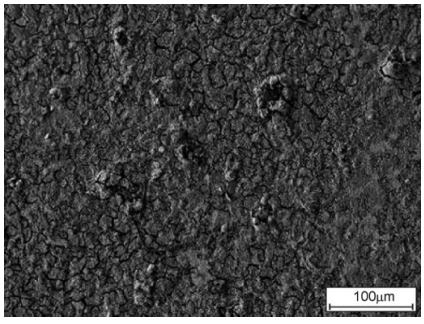

Fig. 34. Surface structure of MCMgAl3Zn1 as-cast state after corrosion test

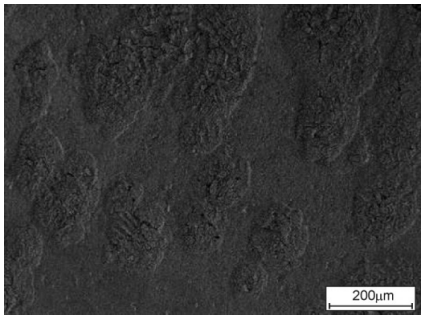

Fig. 35. Surface structure of MCMgAl3Zn1 after solutioning and cooled in air after corrosion test

Corrosion products were also revealed on the surfaces of the samples, forming dense agglomerates in characteristic needle-like shapes, in most cases within the pits (Fig. 30). Analysis of the chemical composition micro-areas (EDS) confirms the presence of corrosion products on the surfaces of samples (Fig. 36).

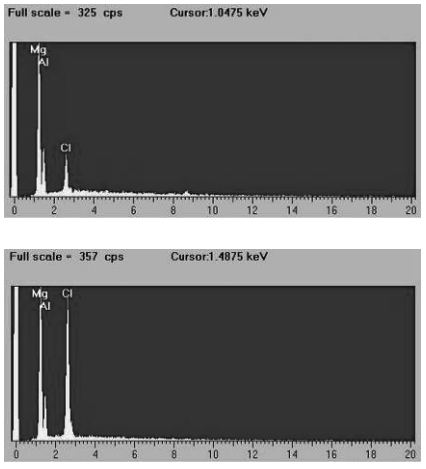

Fig. 36. EDS spectra from regions of corrosion products

The influence of aluminium concentration and type of heat treatment on the hardness of the cast magnesium alloys is shown in Figure 37. Hardness increases with the increase in concentration of aluminium in the analysed alloys from 3 to 12%. The highest hardness of 75.4 HRF in cast alloy is noted in MCMgAl12Zn1 castings. It is more than twice the hardness of MCMgAl3Zn1 alloy 30.6 HRF. Submission of the material to heat treatment (oversaturation and aging) caused an increase in hardness. MCMgAl12Zn1, MCMgAl9Zn1, and MCMgAl6Zn1 alloys reached the highest hardness after aging: 94.6, 75.1, and 53.2 HRF, respectively, and after oversaturation and cooling with the furnace: 85.1, 71.2 and 51.84 HRF. For cases after oversaturation, hardness slightly decreases compared to baseline. For MCMgAl3Zn1 alloy castings the highest hardness are exhibited by samples after oversaturation with water cooling, 40.7 HRF, in other cases the hardness results are similar.

The influence of aluminium concentration and the type of heat treatment on the tensile strength of cast magnesium alloys is shown in Table 10 and Fig. 38. The results of static tensile tests allow to determine and compare the strength and plastic properties of the tested castings of magnesium alloys in their cast condition and after heat treatment. On the basis of performed tests, it was found that the highest tensile strength in the cast condition is to be found in MCMgAl3Zn1 MCMgAl6Zn1 alloys: 192.1 and 191.3 MPa, respectively, which also have the greatest elongation in the cast condition - 11.6 and 15.2% respectively. It was also shown that increasing Al concentration from 6 to 12% reduces the tensile strength in the cast condition to 170.9 MPa. Heat treatment i.e., oversaturation with furnace cooling and aging causes an increase in tensile strength (Table 10).

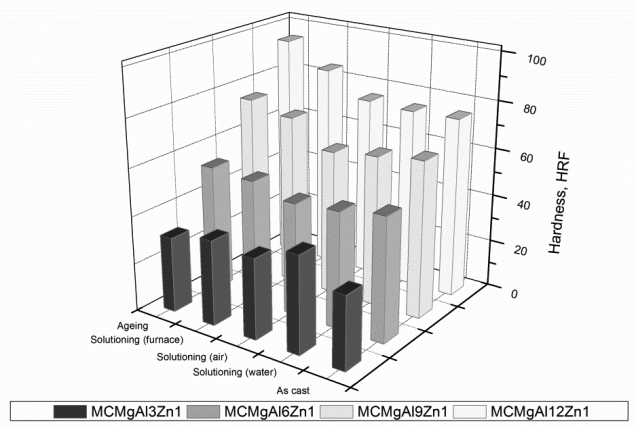

Fig. 37. Results of HRF hardness measurements of magnesium cast alloys

The maximum tensile strength of 294.8 MPa was obtained for the MCMgAl12Zn1 alloy after aging. A significant (50%) increase in tensile strength after aging for the samples of MCMgAl9Zn1 was also noted. The smallest increase in tensile strength after heat treatment was obtained for materials MCMgAl3Zn1 and MCMgAl6Zn, respectively 30.3 and 12.4 MPa. Differences in tensile strength values for alloys after oversaturation with cooling in water and in air are maximum 6 MPa.

The maximum plasticity strength of 129.4 MPa in the cast condition was noted in samples with 12% concentration of aluminium - MCMgAl12Zn1 (Table 10). After heat treatment, the value of the highest plasticity strength is noted in MCMgAl12Zn1, MCMgAl6Zn1 MCMgAl9Zn1 alloys, and after oversaturation with the furnace cooling, it takes the values of 153.7, 158.9 and 96.3 MPa, respectively, slightly higher than in case of aged materials, where it is at the levels of 149.6, 143.8 and 92.03 MPa.

Increasing the concentration of aluminium to 12% decreases the elongation of the tested alloys to the value of 2.97 %, five times lower compared to the elongation MCMgAl3Zn1 alloy castings (Fig. 38). Solutioning with cooling in water and in air causes an increase in the value of elongation even up to 100% for MCMgAl9Zn1 and MCMgAl12Zn1 alloys. Alloys after solutioning with cooling with the furnace and aged are characterized by a slight decrease in elongation compared to the cast condition.

Table 10.
Results of R_m and $R_{p0,2}$ measurements of magnesium cast alloys

	Aging		Solutioning (furnace)		Solutioning (air)		Solutioning (water)		As-cast state	
	R_m, [MPa]	$R_{p0,2}$, [MPa]	R_m, [MPa]	$R_{p0,2}$, [MPa]	R_m, [MPa]	$R_{p0,2}$, [MPa]	R_m, [MPa]	$R_{p0,2}$, [MPa]	R_m, [MPa]	$R_{p0,2}$, [MPa]
MCMgAl3Zn1	203.7	83.5	209.8	84.5	205.5	85.4	210.2	87.	191.3	84.8
MCMgAl6Zn1	222.4	92	214.1	96.3	200.5	85.2	201.5	87.8	192.1	90.7
MCMgAl9Zn1	275.3	140.4	266.6	158.9	247.7	132	241.6	126.1	182.4	121.2
MCMgAl12Zn1	294.8	149.6	276.1	153.7	251	141.5	248.6	136.9	170.8	129.4

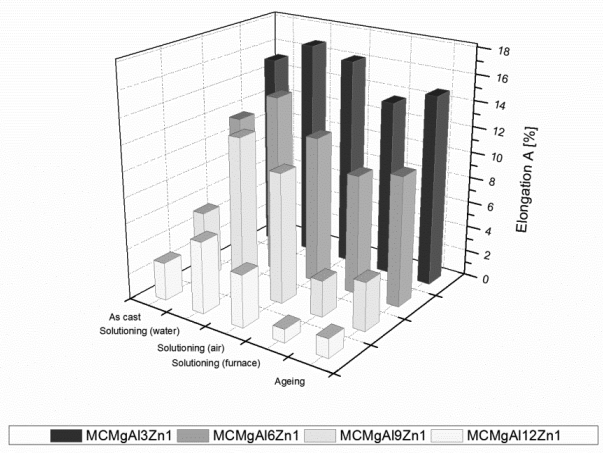

Fig. 38. Results of elongation A measurements of magnesium cast alloys

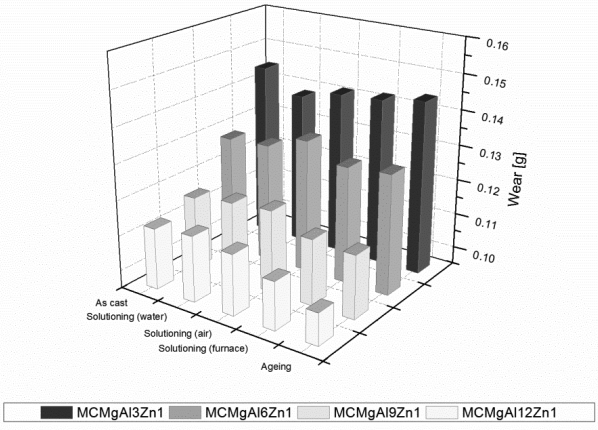

Fig. 39. The results of consumption measurement of magnesium alloys - load 12 N

In order to compare the abrasion resistance under conditions simulating the operating conditions of casting of magnesium alloys, abrasion tests were performed in the metal-metal system. The results of the concluded abrasion tests show that the lowest mean weight loss in the cast condition, and in the condition after heat treatment, at increasing load from 6 to 12 N, occurs in MCMgAl12Zn1 alloys (Fig. 39). These alloys have the best tribological properties among the tested materials. In contrast, the greatest loss of mass in the analysed cases in the original condition and after heat treatment was found to be for the MCMgAl3Zn1 alloy. The largest and smallest abrasion resistance of tested magnesium alloys, revealing itself in an average weight loss, corresponds to the results of hardness of these materials. The results show that heat treatment of tested materials increases their resistance to abrasion wear.

In order to determine the effects of concentrations of aluminium, and the effect of heat treatment on the corrosion resistance of tested Mg alloys, corrosion tests were performed using electrochemical potentiodynamic method in 3% aqueous solution of NaCl. As a result, corrosive wear of the surfaces of the tested materials was identified depending on the weight share of aluminium, as well as on the condition prior to heat treatment (cast material) and the solutioning state, annealed and solidification hardened.

On the basis of potentiodynamic tests, polarization curves were arrived at (Figs. 40-42) as well as anode loops for casting magnesium alloys in the cast condition and after heat treatment. These curves indicate that the tested materials are pit corroding, and Mg-Al-Zn magnesium cast alloys are particularly vulnerable to it. On the basis of the anodic polarization curves, using Tafel extrapolation method in the vicinity of corrosion potential, quantitative data were determined describing the phenomenon of electrochemical corrosion in the tested alloys: corrosion potential value E_{kor} (mV), polarization resistance Rp (kΩ·cm^2) and the density of corrosion current i_{kor} (μA/cm^2) (Table 11). The course of anodic polarization curves, and the corrosion current density value, are evidence of dissolution rate of the tested surfaces. The results obtained in the course of corrosion tests, defining both the tested magnesium alloys and the environment in which the tests were performed, can not be considered separately. Such values as corrosion potential E_{kor} or corrosion current density i_{kor}, can be used to compare properties of the tested materials in both as cast condition and after heat treatment, since all the measurements were performed under the same conditions.

Analysis of the anodic polarization curves, potential and corrosion resistance and corrosion rate, confirms that the best corrosion resistance in the cast condition is to be found in samples characterized by 3% concentration of aluminium - MCMgAl3Zn1 for which the corrosion potential is -1578.4 mV, corrosion resistance 1.290 kΩ·cm^2, and current density in the passive range 3.43 μA/cm^2. In the course of anodic scanning for the MCMgAl3Zn1 alloy, corrosion current density i_{kor} is in most cases less (excluding after aging) in relation to the alloys with a higher Al concentration, which indicates good corrosion resistance of the material.

Table 11.
Results of E_{kor}, R_p and i_{kor} measurements of magnesium cast alloys

		MCMgAl3Zn	MCMgAl6Zn	MCMgAl9Zn	MCMgAl12Zn
As-cast state	E_{kor}, mV	-1578.4	-1621.2	-1551.7	-1548.3
	R_p, kΩ·cm^2	1.29	0.832	0.397	0.36
	i_{kor}, μA/cm^2	3.43	4.6	13.75	14.3
Solutionig (water)	E_{kor}, mV	-1561.1	-1609.2	-1555.6	-1561.1
	R_p, kΩ·cm^2	2.42	1.19	0.31	0.291
	i_{kor}, μA/cm^2	1.83	3.27	15.8	17.4
Solutioning (air)	E_{kor}, mV	-1542	-1586.8	-1537.4	-1539.3
	R_p, kΩ·cm^2	2.54	1.56	0.269	0.171
	i_{kor}, μA/cm^2	1.3	3.1	18.9	22.1
Solutioning (furnace)	E_{kor}, mV	-1594.5	-1642.8	-1573.3	-1577.7
	R_p, kΩ·cm^2	1.25	0.942	0.215	0.159
	i_{kor}, μA/cm^2	4	6.1	21.1	23.8
Aging	E_{kor}, mV	-1539.3	-1555.2	-1522.6	-1518.4
	R_p, kΩ·cm^2	2.26	3.4	1.13	0.402
	i_{kor}, μA/cm^2	1.41	1.3	8	9.6

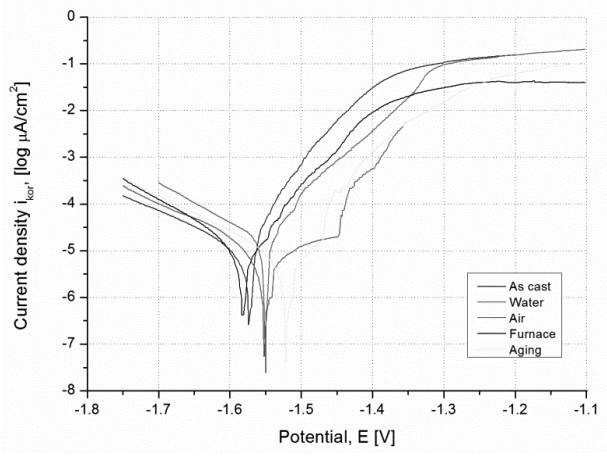

Fig. 40. Anodic curves of the MCMgAl3Zn1 magnesium cast alloys

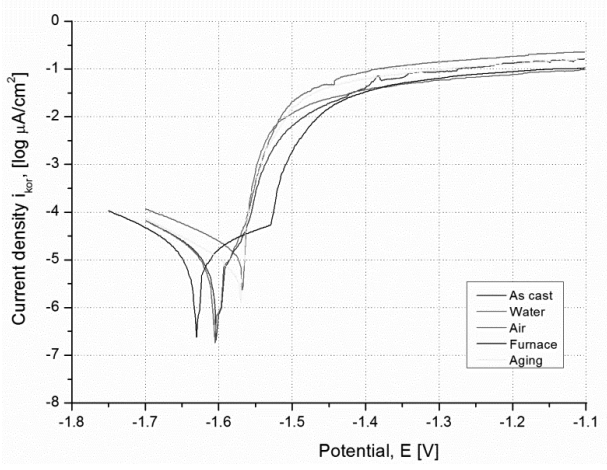

Fig. 41. Anodic curves of the MCMgAl6Zn1 magnesium cast alloys

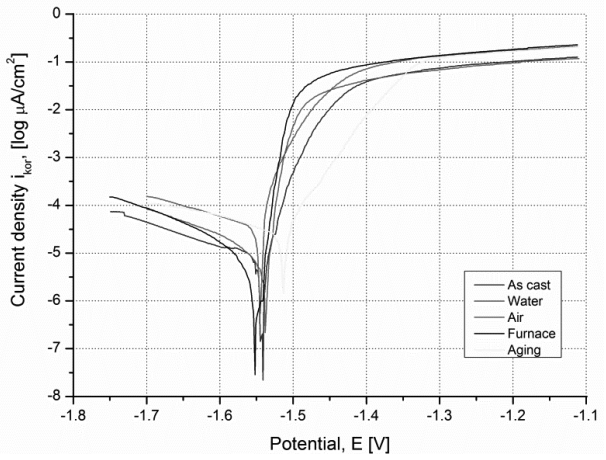

Fig. 42. Anodic curves of the MCMgAl12Zn1 magnesium cast alloys

MCMgAl6Zn1 alloys are also characterized by a slight decrease in corrosion parameter values with respect to the MCMgAl3Zn1 samples. In contrast, a clear deterioration of corrosion resistance when the polarization resistance decreases, while increasing current density was found for MCMgAl12Zn1, MCMgAl9Zn1 alloys (Table 11).

Identical corrosion resistance tests of casting magnesium alloys were performed after heat treatment. The lowest corrosion current density i_{kor}, thus the smallest anodic dissolution of magnesium casting alloys with varying concentrations of aluminium and related best corrosion resistance after heat treatment is to be found in MCMgAl3Zn1 alloys.

In contrast, the weakest resistance to aggressive impact factor, which is related to the growth of damage both into and on the surface of the material is to be found in MCMgAl12Zn1 alloys (Table 11). This is equivalent to acceleration of corrosion in a corrosive solution. Analysis of the results obtained for the alloys with 12, 9 and 6% aluminium concentration confirmed corrosion resistance increase parallels after hardening of the materials, compared to cast alloys, as well as those subjected to solutioning.

The worst parameters describing the phenomenon of pitting corrosion in all the analysed are to be noted in samples after solutioning and cooling with the furnace (Table 11).

3.2. Results of thermal-derivative and structural tests of Mg-Al-Zn alloys

Examples of cooling and crystallization curves of Mg-Al-Zn - cooled at different rates are shown in Figures 43 and 44.

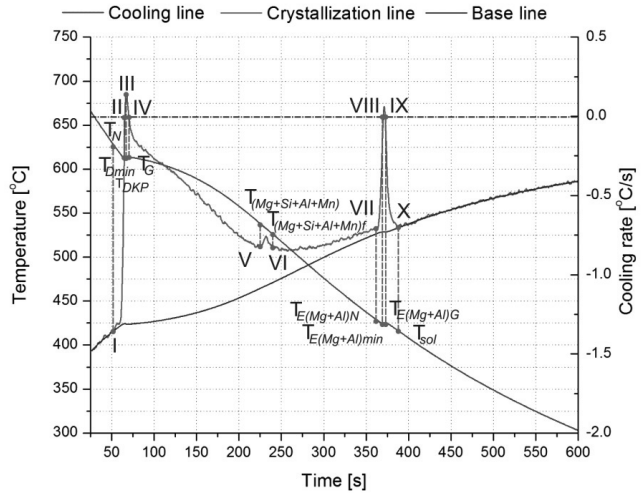

Fig. 43. Representative cooling, crystallization and base line of MCMgAl6Zn1 cooled with 0.6°C/s

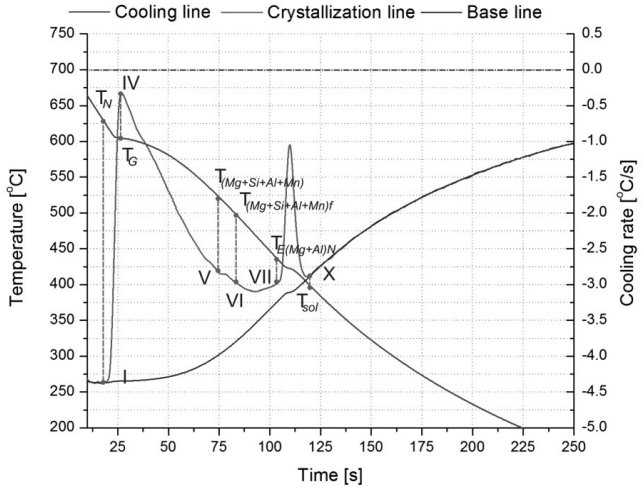

Fig. 44. Representative cooling, crystallization and base line of MCMgAl6Zn1 cooled with 2.4°C/s

Analysing the course of crystallization of alloys, based on the obtained curves, it was found that at temperature T_N α phase nucleation process begins. On the crystallization curve, the effect is manifested by inflection at point I, and a momentary decrease in the cooling rate. Decrease in the cooling rate of the residual liquid is caused by the heat supplied by the α phase nuclei, whose value is less than the heat radiated to the environment by cooling liquid metal. The process ends at point II, where crystallization temperature reaches the minimum - T_{Dmin}, in which α phase crystal growth begins. At this point, the value of the derivative equals zero for the first time. The cooled alloy, due to generation of crystallization heat, warms the remaining liquid to temperature T_{DKP} (point III). Further growth of crystals causes the increase in temperature of the remaining liquid to the maximum crystallization temperature in phase α - T_G (item IV). Further cooling of the alloy initiates the crystallization phases rich in silicon, aluminium and manganese, which emit additional heat, revealing in the crystallization curve with clear thermal effects defined as $T_{(Mg+Si+Al+Mn)}$ and $T_{(Mg+Si+Al+Mn)f}$ (point V and VI). As a result of further cooling of the alloy, after temperature T is reached $T_{E(Mg+Al)N}$ there is nucleation of eutectic α+γ (point VII). Cooled alloy reaches temperature $T_{E(Mg+Al)min}$ (point VIII), and then, the temperature raises to the maximum crystallization temperature of the eutectic $T_{E(Mg+Al)G}$ (point IX). Alloy crystallization ends at point X where it reaches the value of T_{sol}. Due to the nature of the analysed results, i.e., slight differences in the temperature values, and in order to capture the subtle differences in measurement readings using K-type thermocouple and an analysing system, recording of values was used taking onto account the nearest two decimal places.

Figure 45 and Table 12 shows the effect of cooling rate and concentration of magnesium to the α phase nucleation temperature - T_N. As is apparent from the tests, what decides about the nucleation temperature is both concentration of aluminium (lowers the α phase nucleation temperature in accordance with liquidus line) and the rate of cooling (increases the α phase nucleation temperature). For example, with MCMgAl3Zn1 alloy, increasing the cooling rate from 0.6 to 1.2°C/s brings about α phase nucleation temperature from 633.16 to 635.39°C, and further increase of the cooling rate to 2.4°C/s brings about temperature increase to 640.32°C.

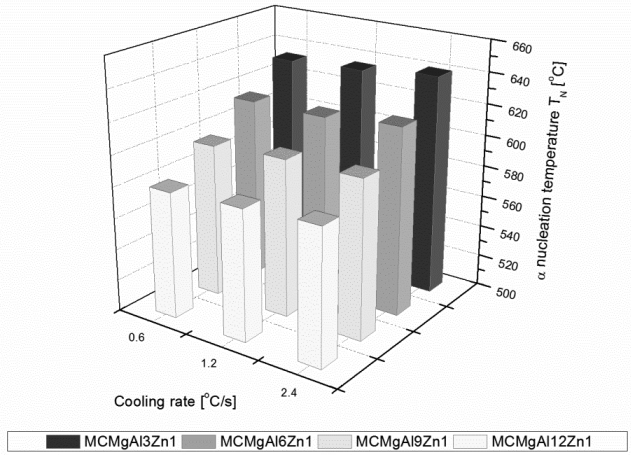

Fig. 45. Influence of cooling rates on α nucleation temperatures of analysed magnesium alloys

Table 12.
Comparison of characteristic temperatures of analysed magnesium alloys after thermal analysis

Alloy	Cooling rate, °C/s	T_N, °C	T_G, °C	T_{sol}, °C	ΔT_N, °C
MCMgAl3Zn1	0.6	633.16	630.85	508.96	2.31
	1.2	635.39	630.42	502.03	4.97
	2.4	640.32	629.71	492.28	10.61
MCMgAl6Zn1	0.6	615.88	611.92	419.47	3.96
	1.2	615.74	610.33	415.44	5.4
	2.4	619.77	608.14	401.66	9.72
MCMgAl9Zn1	0.6	597.97	592.91	413.01	2.39
	1.2	600.74	592.79	412.19	4.81
	2.4	600.89	592.01	404.11	8.88
MCMgAl12Zn1	0.6	580.76	576.03	420.86	2.86
	1.2	583.51	572.87	416.11	9.37
	2.4	586.2	575.09	417.04	14.32

Based on the calculation of the values obtained from the thermal-derivational analysis, the degree of liquid supercooling was determined during the crystallization of solid solution α. It was found that the liquid subcooling value is primarily dependent on the rate of cooling applied in the experiment. The value of liquid supercooling of the crystallizing phase α was determined by the following equation:

$$\Delta T_{DN} = T_N - T_{D\min} \tag{4}$$

where:
T_N - nucleation temperature,
T_{Dmin} - phase growth temperature α.

Figure 46 and Table 12 shows the effect of cooling rate and mass concentration of magnesium on the value of maximum temperature (T_G) of crystallization of phase α. The tests have shown that the change in the cooling rate does not change the maximum crystallization temperature of phase α. The results demonstrated that the value of temperature T_G decreases with increasing aluminium concentration. For example, for alloys cooled at a rate of 0.6°C/s, increase in concentration of aluminium from 3 to 6% causes lowering of the maximum crystallization temperature of phase α from 630.85 to 611.92°C, and further increase in concentration of aluminium to 9% results in a decrease in temperature to 592.91°C. The lowest value of maximum crystallization temperature of phase α, being 576.03°C, was determined for the alloy containing 12% aluminium.

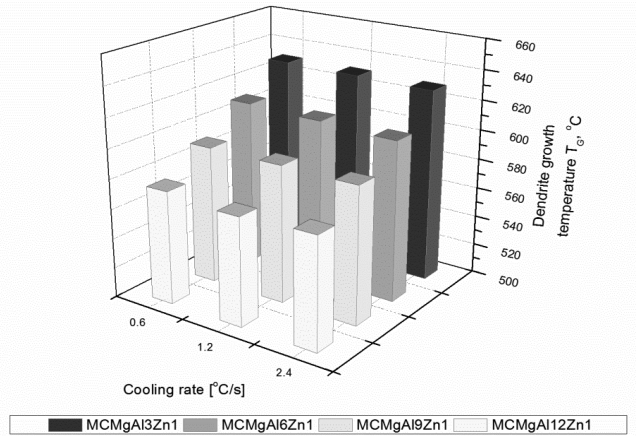

Fig. 46. Influence of cooling rates on dendrite growth temperatures of analysed magnesium alloys

The influence of the mass concentration of aluminium and the cooling rate on the value of the solidus temperature (T_{sol}) is shown in Figure 47 and in Table 12. As is clear from the analyses, both the increase in mass concentration of aluminium and in the cooling rate will decrease the temperature T_{sol}. For example, for the alloy MCMgAl6Zn1, an increase in cooling rate from 0.6 to 1.2°C/s reduces the solidus temperature from 419.47°C to 415.44°C, and further increase the cooling rate to 2.4 °C/s results in lowering the temperature T_{sol} to 401.66°C.

Table 13 shows the effect of cooling rate and the effect of aluminium mass concentration on the value of heat emitted during alloy crystallization. On the basis of the calculations, it was found that variable concentration of aluminium has the greatest impact on the increase in heat (Q_c) generated during the crystallization of the alloy. Increase in aluminium concentration in the studied alloys increases the heat value Q_c. In case of increasing of the cooling rate, a slight increase in the generated crystallization heat was noted, except for the alloy MCMgAl3Zn1.

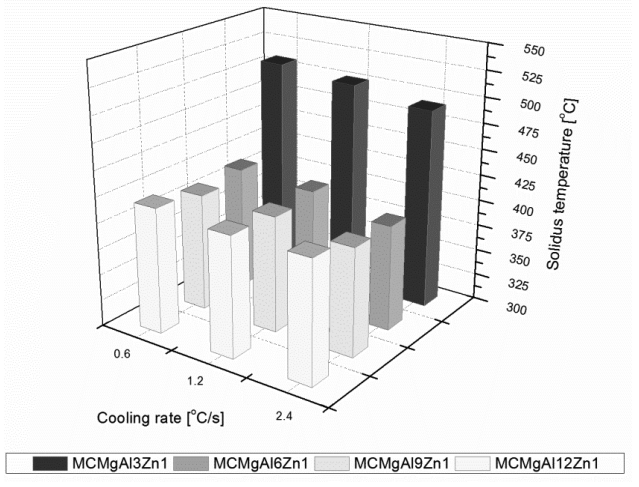

Fig. 47. Influence of cooling rates on solidus temperatures of analysed magnesium alloys

Table 13.
Comparison of latent heat of crystallization process of analysed magnesium alloys

Alloy	Cooling rate, °C/s	Q_c, J
MCMgAl3Zn1	0.6	1380.27
	1.2	1421.49
	2.4	1457.64
MCMgAl6Zn1	0.6	1404.53
	1.2	1529.03
	2.4	1592.57
MCMgAl9Zn1	0.6	1562.39
	1.2	1537.68
	2.4	1638.6
MCMgAl12Zn1	0.6	1300.27
	1.2	1650.67
	2.4	1573.44

The results of metallographic examinations using a light microscope are shown in Figure 48.

a)

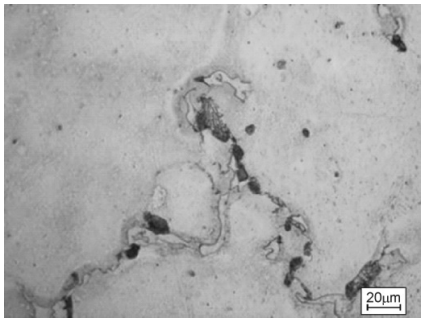

b)

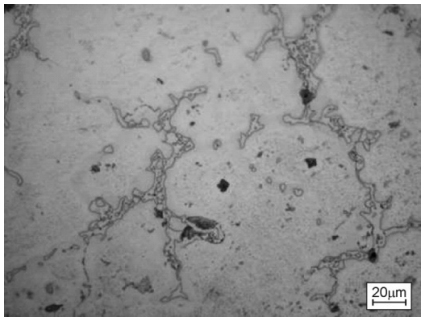

Fig. 48. Structure of MCMgAl6Zn1 cooled with: a) 0.6; b) 2.4°C/s

The analysed alloys: MCMgAl3Zn1, MCMgAl6Zn1, MCMgAl9Zn1, MCMgAl12Zn1 have the structure of a solid solution α with solidification of phase γ($Mg_{17}Al_{12}$) at grain boundaries and areas of lamellar mixture α+γ. The so-called abnormal eutectic (pseudo-eutectic) zones are observed, solidification of phases containing Al and Mn and Mg_2Si phase, the share of which is dependent on mass concentration of Al and increases with its increase. The shape of the individual solidifications varies with the change in cooling rate (Fig. 48).

Table 14 and Figure 49 show the effect of cooling rate and mass concentration of aluminium on grain size.

Table 14.
Grain size of analysed magnesium alloys after thermal analysis

Alloy	Cooling rate, °C/s	Grain size Z, µm	Confidence interval		Standard deviation	Error, %
			-95%	+95%		
MCMgAl3 Zn1	0.6	179.26	154.38	204.14	20.04	11.18
	1.2	125.48	115.20	135.75	8.28	6.6
	2.4	85.4	77.11	93.68	6.67	7.82
MCMgAl6 Zn1	0.6	190.3	177.87	202.74	10.01	5.26
	1.2	137.05	123.54	150.56	10.88	7.94
	2.4	86.28	80.27	92.29	4.84	5.61
MCMgAl9 Zn1	0.6	143.53	114.83	172.24	23.12	16.11
	1.2	74.46	59.24	89.69	12.26	16.47
	2.4	66.73	52.8	80.66	11.22	16.82
MCMgAl1 2Zn1	0.6	110.39	83.01	137.76	22.05	19.97
	1.2	112.26	109.59	114.94	2.15	1.92
	2.4	84.58	74.73	94.44	7.94	9.39

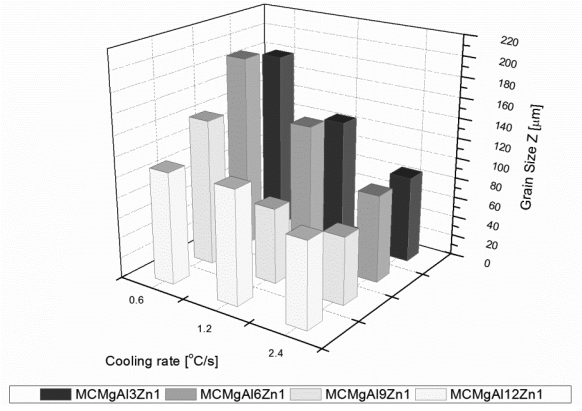

Fig. 49. Results of grain size measurements of analysed magnesium alloys

Tests have shown that increasing cooling rate decreases the grain size for each of the tested alloys. As a result of the tests it was found that the largest grain (190.3 μm) is characteristic for MCMgAl6Zn1 alloy (Tab. 14). Changing the cooling rate from 0.6 to 2.4°C/s causes a halving of the grain size. A similar relationship was found with respect to other analysed alloys used in the experiment. Increasing aluminium mass concentration causes a slight reduction in grain size (Fig. 49).

As a result of thin film observation in transmission electron microscopy (Figs. 50 and 51), it was found that the structure of the magnesium casting alloys MCMgAl3Zn1, MCMgAl6Zn1, MCMgAl9Zn1 and MCMgAl12Zn1 cooled at cooling rates used in the experiment consists in α-Mg solid solution with solidifications of phase γ-$Mg_{17}Al_{12}$. Solidifications of phase γ are mainly part of the eutectic, and occur in the form of large particles located mainly at grain boundaries.

As a result of element surface distribution tests and X-ray quantitative microanalysis, using EDS spectrography and backscattered electrons, the presence of the main alloying elements, that is Al, Zn, Mn and Si included in Mg-Al-Zn casts was confirmed. Moreover, information was obtained about mass and atomic concentrations of individual elements in the studied microareas.

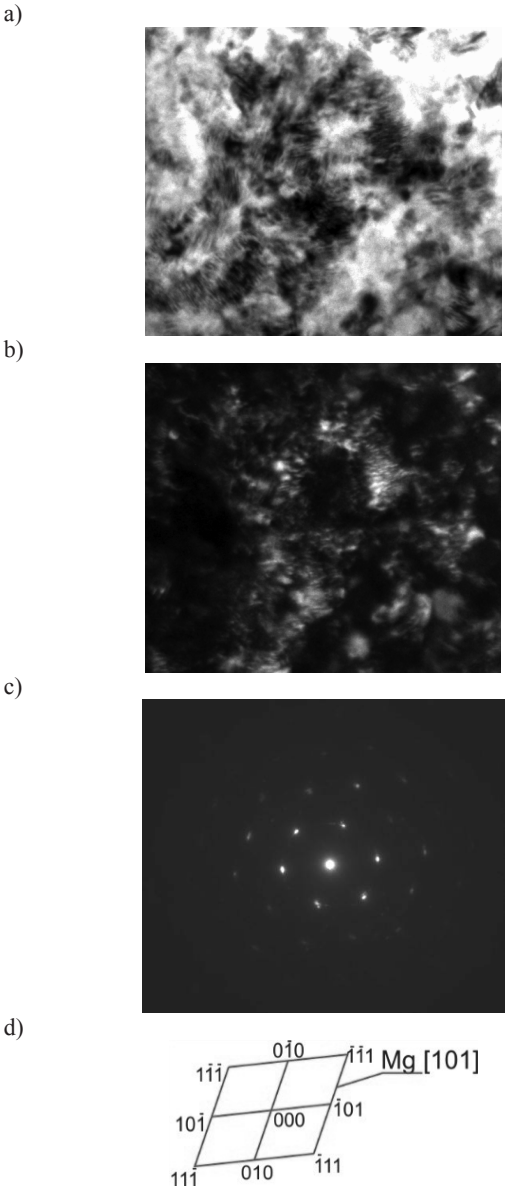

Fig. 50. TEM images of the MCMgAl6Zn1 alloy cooled at 0.6°C/s a) bright field; b) dark field; c) diffraction pattern of area shown in a); d) part of solution for diffraction pattern shown in c

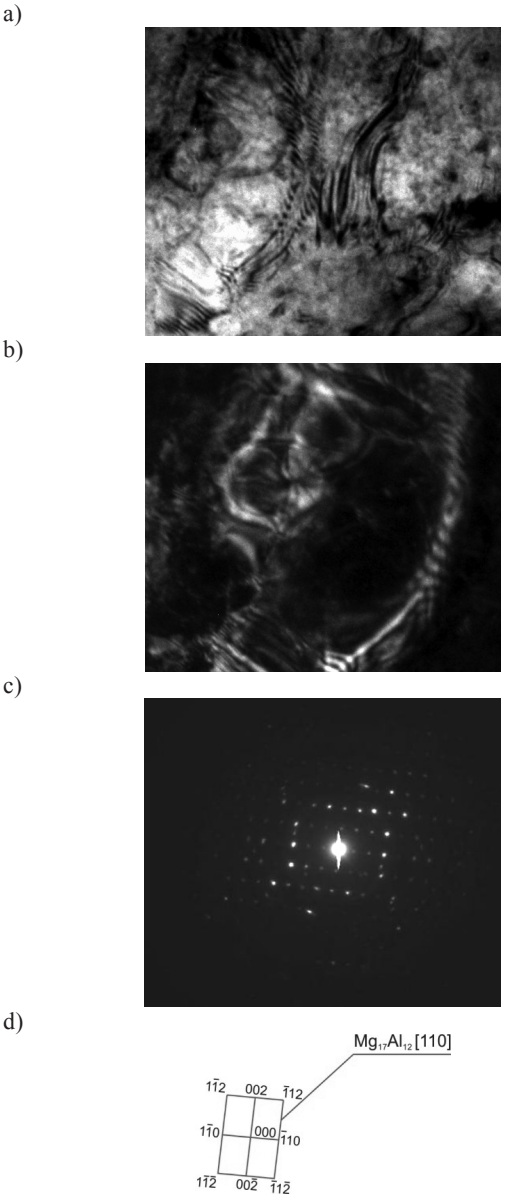

Fig. 51. TEM images of the MCMgAl6Zn1 alloy cooled at 0.6°C/s a) bright field; b) dark field; c) diffraction pattern of area shown in a); d) part of solution for diffraction pattern shown in c

Observations of the structure made by a scanning electron microscope and X-ray microanalysis quantitative and qualitative confirm the presence in the tested eutectic alloys α+γ, solidifications of phase Mg_2Si angular shaped, as well as phases containing Al and Mn, irregularly shaped and occurring largely in the acicular form (Figs. 52 and 53).

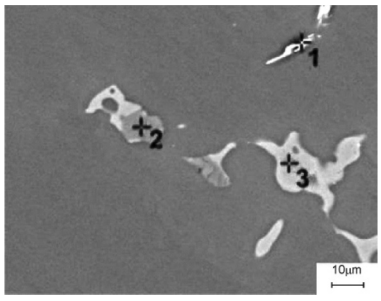

Fig. 52. Structure of MCMgAl6Zn1 alloy cooled at 0.6°C/s

a)

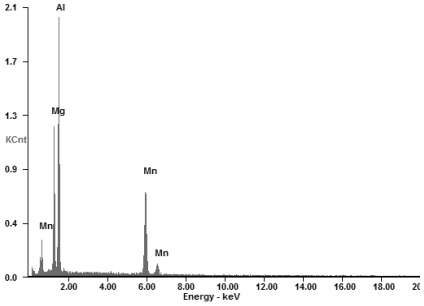

b)

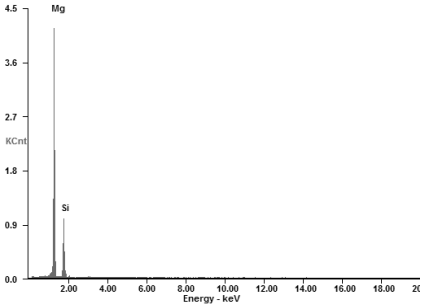

c)

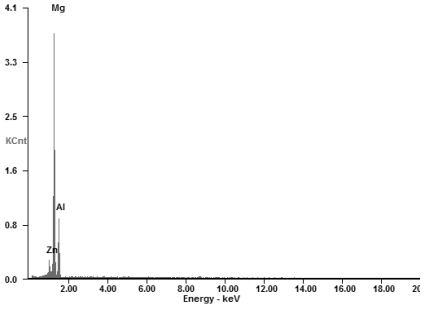

Fig. 53. EDS spectra of the MCMgAl6Zn1 cooled at 0.6°C/s: a) analysis 1, b) analysis 2, c) analysis 3 from Fig. 52

Chemical analysis of the surface distribution of elements (Fig. 54) and quantitative microanalysis performed on transverse polished sections of magnesium alloy casts using EDS (Table 15) confirms increased concentration of magnesium, silicon, aluminium and manganese in the tested microregions, which proves the occurrence of solidifications in the alloy structures containing Mg and Si, and phases with a high concentration of Al and Mn.

Table 15.
Results of the quantitative analysis of chemical composition magnesium cast alloy MCMgAl6Zn1 cooled at 0.6°C/s

Analysis	Element	The mass concentration of main elements, %	
		mass	atomic
1	Mg	21.71	28.93
	Al	40.74	48.92
	Mn	37.55	22.15
2	Mg	65.18	68.38
	Si	34.82	31.62
3	Zn	6.5	2.61
	Mg	60.17	64.97
	Al	33.33	32.42

Figure 55 shows X-ray diffractograms of MCMgAl6Zn1 alloy, cooled at rates assumed in the experiment. Using of X-ray phase qualitative analysis it was found that in the tested alloys there is a phase γ($Mg_{17}Al_{12}$) and a phase α-Mg constituting the matrix of alloys. X-ray qualitative phase analysis did not confirm the occurrence of Mg_2Si type and phases containing Al and Mn, which may indicate that the share of these solidifications is below the minimum detection capability appropriate for the X-ray method.

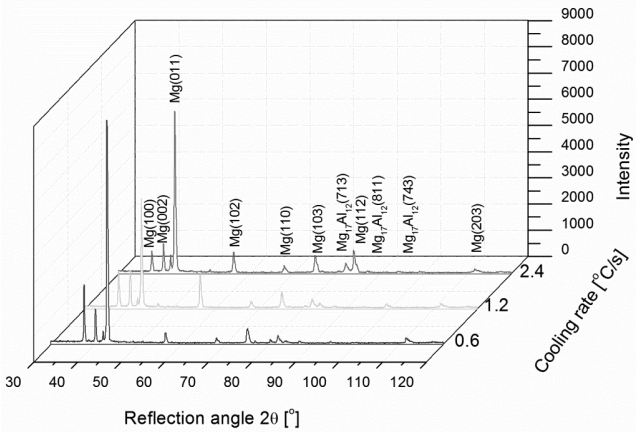

Fig. 55. X ray diffraction pattern of the MCMgAl6Zn1 magnesium cast alloy cooled with different cooling rates

Both the results of the phase composition and the chemical composition of Mg-Al-Zn alloy casting confirm that the cooling rate does not affect the phase composition of the tested alloys.

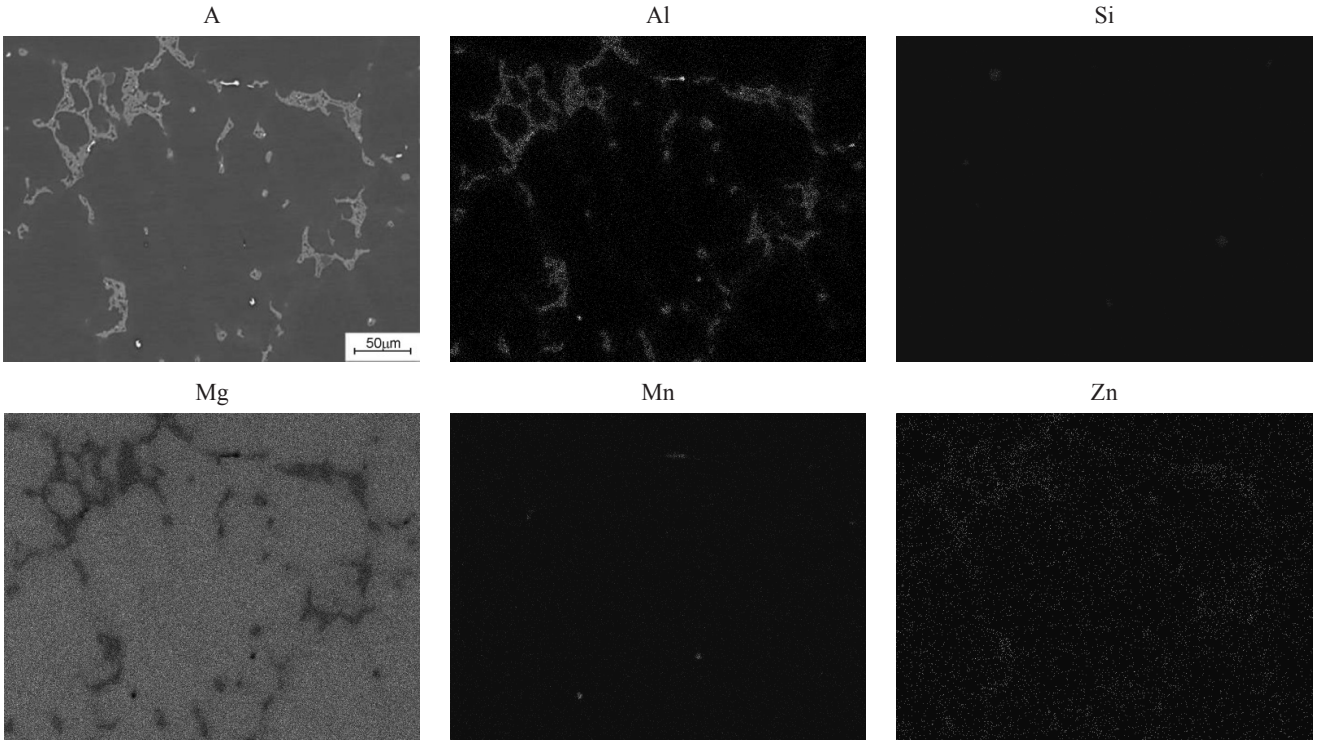

Fig. 54. The area analysis of chemical elements alloy MCMgAl6Zn1 cooled with 1.2°C/s: image of secondary electrons (A) and maps of elements' distribution

Table 16.
Results of HRF, R_c and $R_{c0,2}$ measurements of analysed magnesium alloys after thermal analysis

	Cooling rate, °C/s	MCMgAl3Zn	MCMgAl6Zn	MCMgAl9Zn	MCMgAl12Zn
Hardness HRF	0.6	21.3	43.87	59.27	71.48
	1.2	25.97	46.02	62.5	72.43
	2.4	19.53	50.18	64.94	74.2
Ultimate compressive strength R_c, MPa	0.6	245.94	296.71	281.31	256.08
	1.2	268.36	304.03	289.8	260.09
	2.4	275.78	303.53	316.04	273.69
Yield strength $R_{c0,2}$, MPa	0.6	73.86	99.22	133.84	125.89
	1.2	86.93	103.3	107.46	150.26
	2.4	77.86	91.74	104.86	164.03

Table 16 shows the impact of mass concentration of aluminium and the cooling rate on hardness of the tested alloys. On the basis of the tests, a linear increase in hardness with increasing concentration of aluminium was noted, including MCMgAl6Zn1, and MCMgAl12Zn1 MCMgAl9Zn1 alloys with the increase in cooling rate. As to MCMgAl3Zn1 alloy, an increase in hardness of up to 26 at a cooling rate 1.2°C/s was noted. Increasing the cooling rate to 2.4°C/s results in a decrease in hardness to 19.6 HRF. The highest hardness at 74.2 HRF was obtained for MCMgAl12Zn1 alloy, cooled at a rate of 2.4°C/s.

It was found that the highest value of the compressive strength of 296.7 MPa is typical for MCMgAl6Zn1 alloy, and the lowest at 245.9 Mpa is typical for MCMgAl3Zn1 alloy (alloys cooled at a rate of 0.6°C/s). Changing the cooling rate in the analysed alloys increases their compressive strength. The largest increase in R_c value, with increasing cooling rate was found for alloys MCMgAl3Zn1 and MCMgAl9Zn1. Increasing the cooling rate to a maximum increases compressive strength in MCMgAl3Zn1 alloys. MCMgAl9Zn1 to the values of 275.8 and 316 MPa, respectively, and for MCMgAl6Zn1 materials. Regarding MCMgAl12Zn1, by average of 10-15 MPa.

The influence of aluminium concentration and cooling rate on yield strength limit in compression is shown in Table 16. Based on the tests, it was found that mass concentration of aluminium has the biggest impact on yield strength. With the increase in the concentration of aluminium in the tested alloys, also the value of the yield strength increases. The lowest value of the yield strength of 73.9 MPa can be found in MCMgAl3Zn1alloy, and the highest, at 133.8 MPa, in MCMgAl9Zn1 alloy. Regarding alloy MCMgAl12Zn1, a change in the cooling rate from 0.6°C/s to

2.4°C/s causes an increase in yield strength limit from 125.9 to 164 MPa. The opposite situation occurs in case of MCMgAl9Zn1. With the increase in the cooling rate the value of the yield strength decreases from 133.8 to 104.9 MPa. For alloys MCMgAl3Zn1 and MCMgAl6Zn1 a change the cooling rate does not change the yield strength.

3.3. The structure and properties of coatings on Mg-Al-Zn alloy substrate applied from vapour phase by CVD and PVD chemical and physical methods

As a result of metallographic tests under a scanning electron microscope, it was found that the surface morphology of coatings made with PVD technique clearly shows a heterogeneity related to the presence of a number of microparticles in the form of drops in the structure which, consequently, may also influence the mechanical, physical and chemical properties of the examined surface. The largest surface inhomogeneity, in comparison to the other tested surface coatings, is to be found in such coatings as Ti/TiCN/TiAlN and Ti/TiCN/CrN, in which a number of solidified droplets was identified (Figs. 56, 57). The occurrence of these morphological defects is related to the essence of the process of cathodic arc evaporation. The observed droplets are clearly differentiated in terms of shape and size, depending on the process conditions and the nature of the metal vapour source used (Figs. 56-59). The occurrence of hollows was also determined, which are formed by solidified drops dropping out after the PVD process finishes (Figs. 56-59). In the case of the DLC coating obtained on the surface by the PACVD process, it is also possible to identify small droplets, often in spheroidal form of (Fig. 60). The results of tests performed using energy-dispersive X-ray spectroscopy indicate that, atomically, the identified droplets in ~95 % consist of carbon (Table 17). The surface morphology of DLC coating differs significantly from the surface morphology obtained in the classic high-temperature CVD processes whose characteristic feature is the presence of, ex., a network of microcracks, corrugated surfaces or surfaces with spherical shapes.

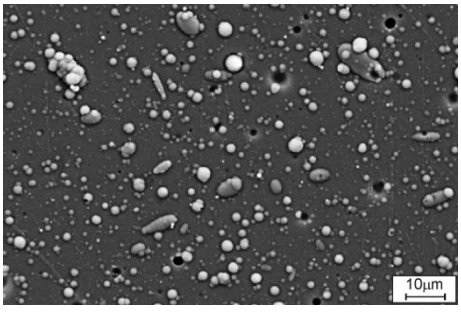

Fig. 56. Surface topography of Ti/TiCN/TiAlN layer deposited onto MCMgAl6Zn1

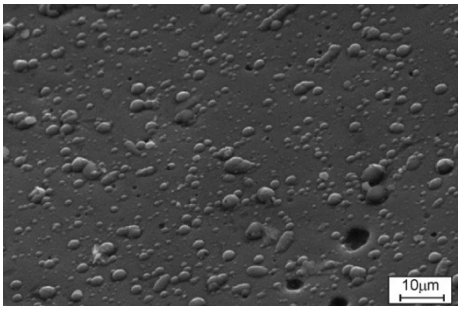

Fig. 57. Surface topography of Ti/TiCN/CrN layer deposited onto MCMgAl6Zn1

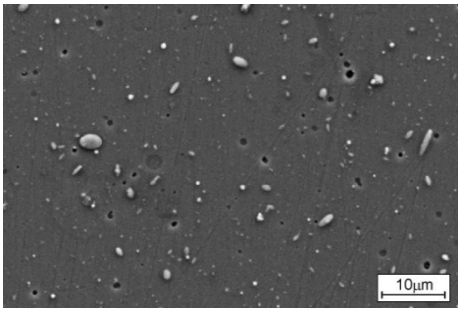

Fig. 58. Surface topography of Cr/CrN/CrN layer deposited onto MCMgAl9Zn1

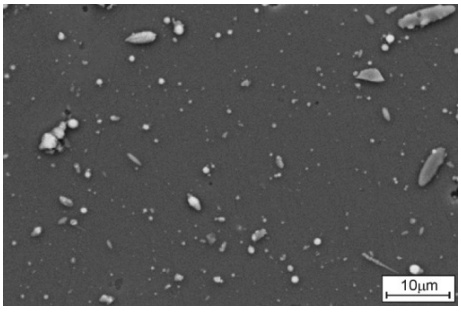

Fig. 59. Surface topography of Ti/TiSiN/TiSiN layer deposited onto MCMgAl12Zn1

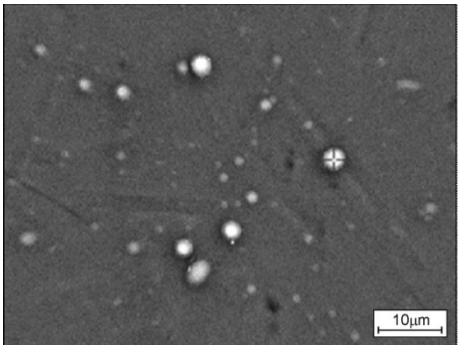

Fig. 60. Surface topography of Ti/DLC/DLC layer deposited onto MCMgAl12Zn1

Table 17.
Results of the quantitative analysis of chemical composition Ti/DLC/DLC layer deposited onto MCMgAl12Zn1

Element	The mass concentration of main elements, %	
	mass	atomic
C	84.11	95.21
Mg	4.38	2.11
Ti	10.31	2.68

On the basis of fractographic tests of fractures of specimens of magnesium alloys with analysed surface coatings, using scanning electron microscopy, a clear transition zone between the substrate and the coating can be identified. The resulting coatings have a compact structure with no visible delamination and defects, they are uniformly applied and adhere tightly to the substrate (Figs. 61, 62). Observation of fractures confirms that the Ti/TiCN/TiAlN and Ti/TiCN/CrN coatings exhibit a layered structure, with a distinct transition zone between the gradient coating and the wear protective coating, obtained by the use of separate sources of metal pairs (Figs. 63, 64). In the case of Cr/CrN/CrN, Ti/TiSiN/TiSiN coatings, no visible differences were identified on the cross-section (Figs. 65, 66).

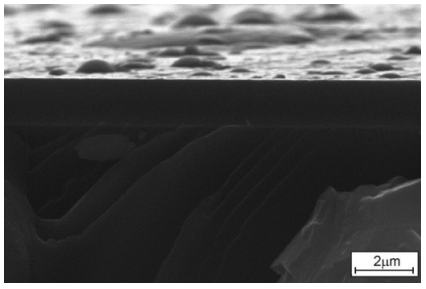

Fig. 61. Fracture topography of Ti/DLC/DLC layer deposited onto MCMgAl12Zn1

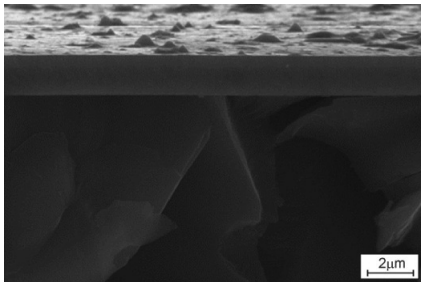

Fig. 62. Fracture topography of Cr/CrN/CrN layer deposited onto MCMgAl12Zn1

The layer of titanium nitride in the case of Cr/CrN/TiN coating has a column-like structure (Fig. 67, 68). Moreover, it was found that multilayer carbon coatings, type Ti/DLC/DLC obtained by CVD, because of the similarity of the phase composition of both the gradient and antiwear coating, show no clear transition zone between the different coatings. Around the thin adhesive coating, whose task is to improve the adhesion of the coating to the substrate, a characteristic bright, continuous layer of titanium has been identified, confirmed by EDS analysis.

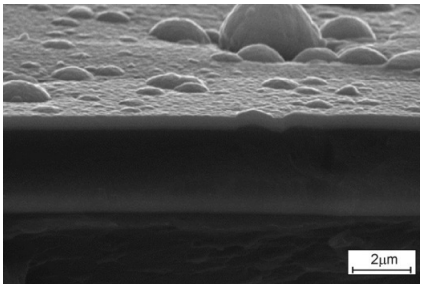

Fig. 63. Fracture topography of Ti/TiCN/CrN layer deposited onto MCMgAl6Zn1

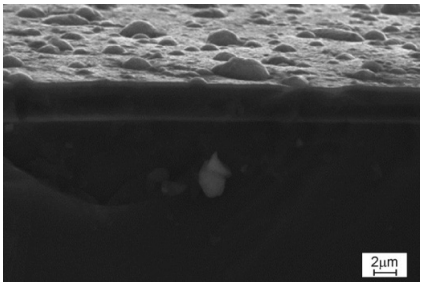

Fig. 64. Fracture topography of Ti/TiCN/TiAlN layer deposited onto MCMgAl9Zn1

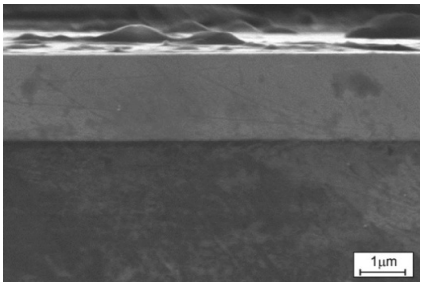

Fig. 65. Fracture topography of Cr/CrN/CrN layer deposited onto MCMgAl6Zn1

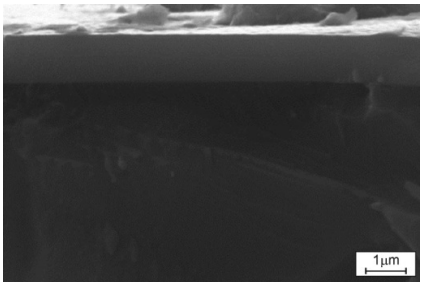

Fig. 66. Fracture topography of Ti/TiSiN/TiSiN layer deposited onto MCMgAl9Zn1

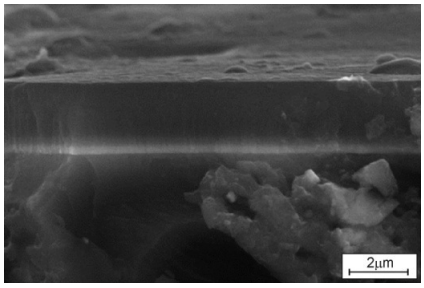

Fig. 67. Fracture topography of Ti/DLC/DLC layer deposited onto MCMgAl9Zn1

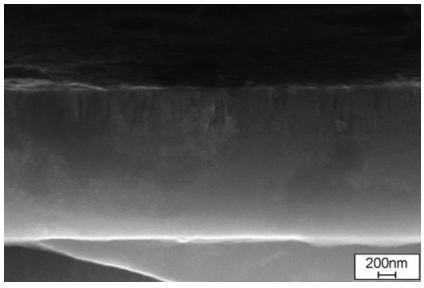

Fig. 68. Fracture topography of Cr/CrN/TiN layer deposited onto MCMgAl9Zn1

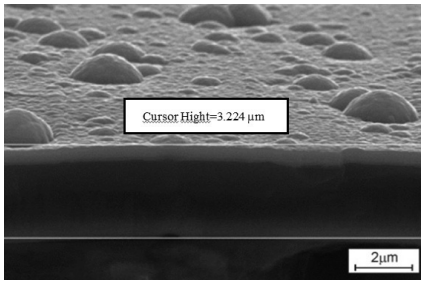

Fig. 69. Fracture topography of Ti/TiCN/CrN layer deposited onto MCMgAl6Zn1

In the case of such coatings as Ti/DLC/DLC and Cr/CrN/CrN laid on analysed magnesium alloys, it was found that the gradient layers of those coatings, DLC and CrN respectively, show structure classified as T according to the Thornton model (Figs. 67, 70). Basing on metallographic observation of surfaces and fractures of coatings produced on casting magnesium alloys, with varying the concentration of alloying elements, in particular aluminium - variable from 3 to 12% - it is difficult to determine significant differences in the nature of layers depending on the substrate used.

In order to measure the thickness of the applied coatings, metallographic observations have been performed of fractures of tested samples under scanning electron microscope. Measurement of coating thickness at different areas of observed fractures confirmed the uniformity of layers. In the case of Ti/TiCN/TiAlN and Ti/TiCN/CrN coatings, where a clear layered structure has been identified, it was possible to measure the thickness of the individual layers. The gradient layer thickness is not bigger than 2.5 µm, while the top antiwear layer thickness is about 0.6 µm (Fig. 69). The thickness of the other layers, i.e. Cr/CrN/CrN, Cr/CrN/TiN, Ti/TiSiN/TiSiN and Ti/DLC/DLC did not exceed 2.6 µm, respectively, ~1.8; ~1.8; ~1.4; ~2.5 µm (Figs. 70-72).

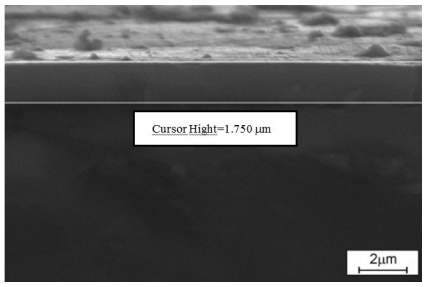

Fig. 70. Fracture topography of Cr/CrN/CrN layer deposited onto MCMgAl3Zn1

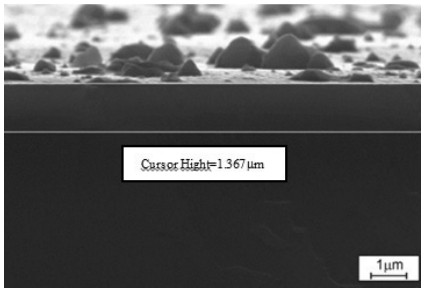

Fig. 71. Fracture topography of Ti/TiSiN/TiSiN layer deposited onto MCMgAl9Zn1

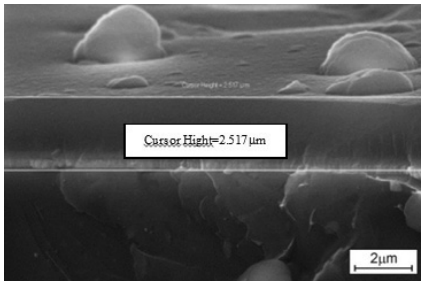

Fig. 72. Fracture topography of Ti/DLC/DLC layer deposited onto MCMgAl6Zn1

The diffractive test results obtained using a high resolution transmission electron microscope confirmed that, in keeping to the assumptions, it was possible to identify the following phases: TiN, CrN and graphite, respectively, occurring in the surface layer of coatings: Ti/TiCN/TiAlN, Ti/TiCN/CrN, Cr/CrN/CrN, Ti/TiSiN/TiSiN, Cr/CrN/TiN and Ti/DLC/DLC (Fig. 73-76). It should be emphasized that the TiN phase isomorphism which is a precondition of substitution of atomic positions of titanium by aluminium or silicon, respectively, (Ti, Al)N and (Ti, Si)N prevented diffractional distinctions of phases TiAlN and TiSiN.

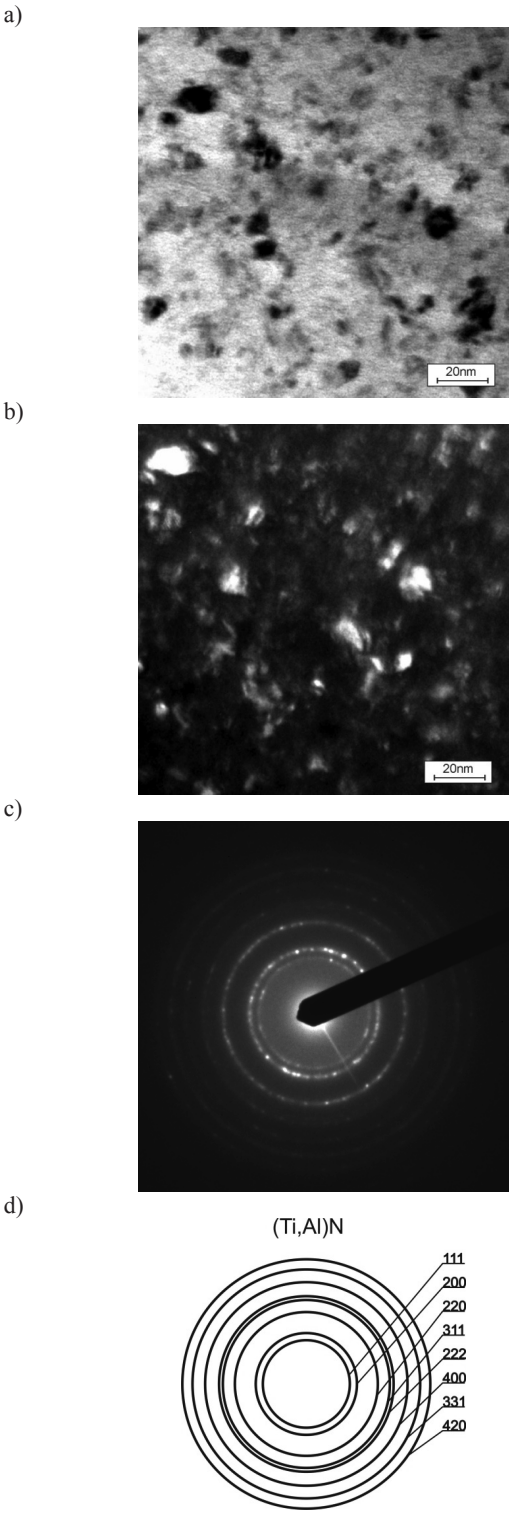

Fig. 73. TEM images of Ti/TiCN/TiAlN layer deposited onto MCMgAl6Zn1 a) bright field; b) dark field; c) diffraction pattern of area shown in a); d) part of solution for diffraction pattern shown in c

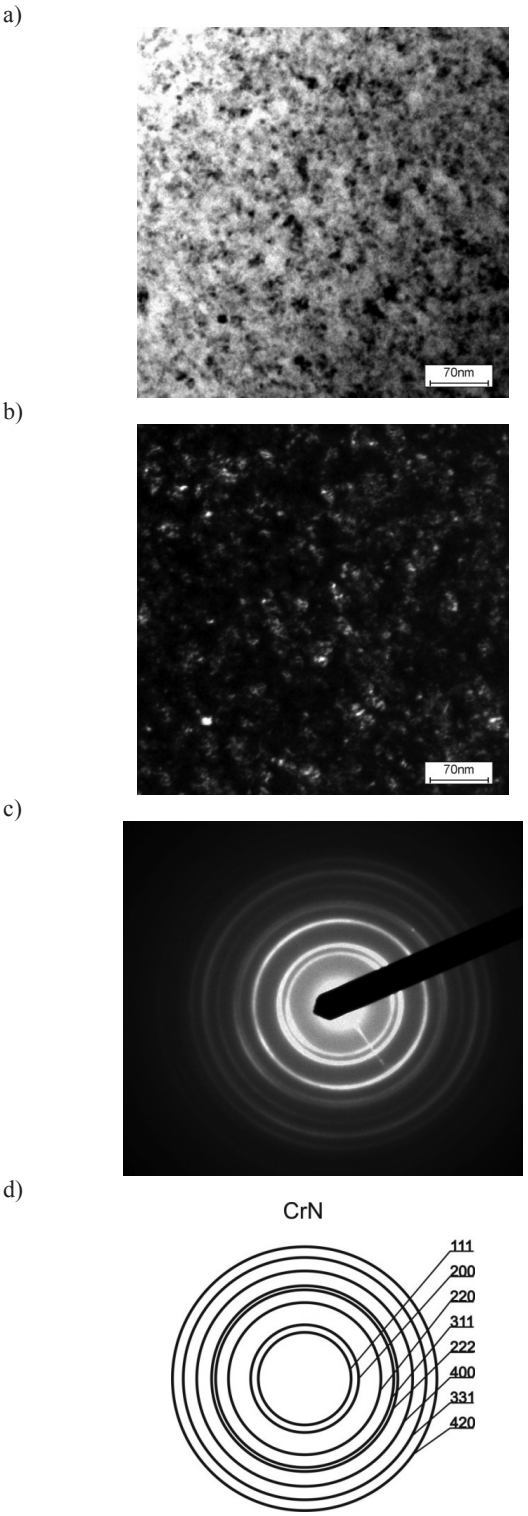

Fig. 74. TEM images of Cr/CrN/CrN layer deposited onto MCMgAl3Zn1 a) bright field; b) dark field; c) diffraction pattern of area shown in a); d) part of solution for diffraction pattern shown in c

In all cases of analysed coatings manufactured on lightweight magnesium alloys it has been proved that they have a nanocrystalline nature within the studied areas (Figs. 73-76). Inside the Ti/TiSiN/TiSiN type coating it was also possible to observe solidified metal droplets, the presence of which results from the nature of the process of cathodic arc evaporation (Figs. 75, 76).

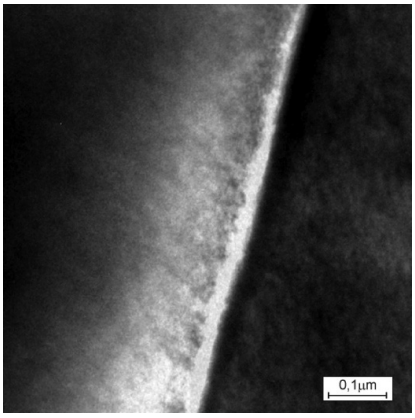

Fig. 75. The boundary of the surface Ti/TiSiN/TiSiN layer deposited onto MCMgAl9Zn1, bright field

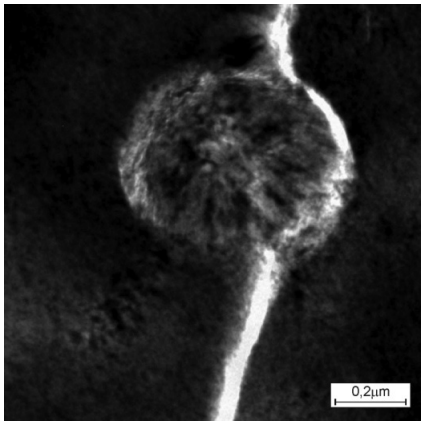

Fig. 76. The structure of the solidified Ti/TiSiN/TiSiN coating metal drops deposited onto MCMgAl9Zn1, bright field

In the case of TiN phase, its regular network structure has been confirmed, belonging to the Fm3m (225) space group having identity periods equal to a=b=c=0.424173 nm. Also, the CrN phase, both for the type of Ti/TiCN/CrN coating, and Cr/CrN/CrN was identified as regular, belonging to the Fm3m (225) group, with identity periods equal to a=b=c=0.414 nm. The electron diffraction image from the TiCN/CrN coating proves the occurrence of fine-grained structure with crystallites of not bigger than ≤10 nm (Fig. 78). The diffraction tests also confirmed the occurrence of Ti/DLC/DLC coating in areas of examined outer layers, produced in the PACVD process of crystallizing graphite in the hexagonal cell belonging to the P63mc (186) group with the following network parameters a=b=0.2 nm, c=0.679 nm, while identification of the radius of first circle visible in the resulting diffraction (Fig. 79) allowed the unambiguous confirmation of the presence of the graphite phase.

a)

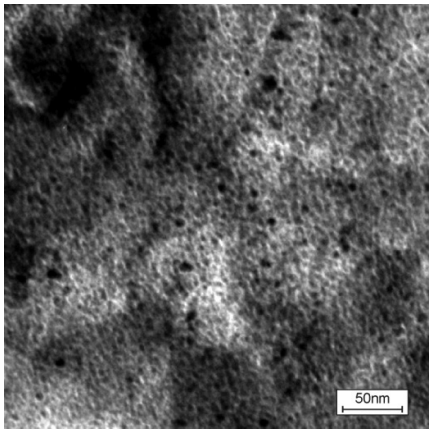

b)

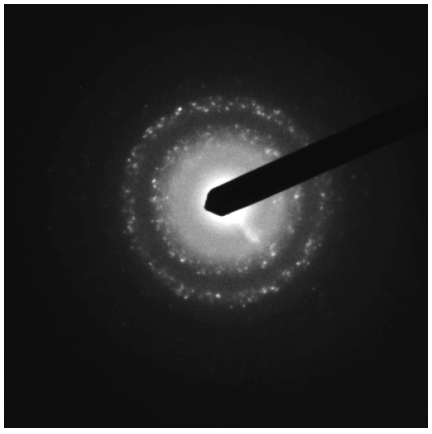

Fig. 78. TEM images of Ti/TiCN/TiAlN layer deposited onto MCMgAl6Zn1 a) bright field; b) diffraction pattern of area shown in a

Crystallite size and dispersion of the applied coating was determined based on the structure obtained using the dark-field techniques. It was found that the coatings were compact, with high homogeneity of crystallites, and have little scatter in terms of their size - in the range of 10 to 20 nm (Fig. 73-79). The only exception is the TiN phase in the Cr/CrN/TiN coating, where crystallite size was measured at the level of 200 nm (Fig. 80, 81). As a result of quality tests using X-ray microanalysis under TEM, done using energy-dispersive X-ray spectroscopy, in the analysed areas of coating, and at the phase border, the presence of elements such as titanium, chromium, silicon, carbon, nitrogen was confirmed, forming part of the tested coatings (Fig. 80, 81).

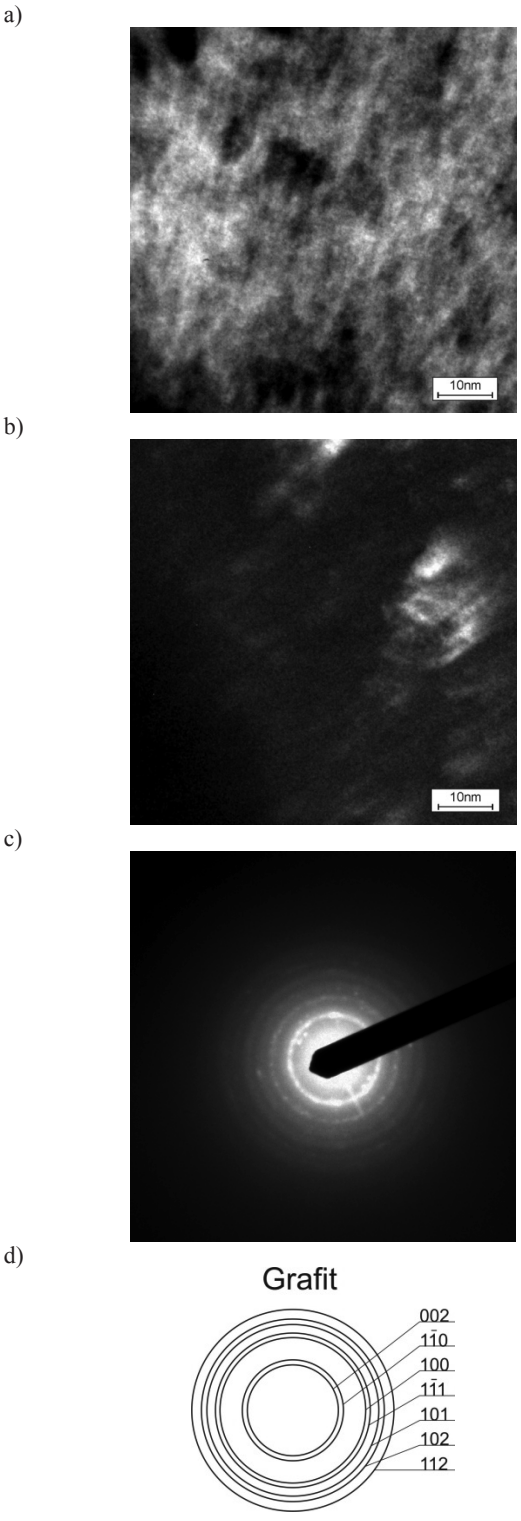

Fig. 79. TEM images of Ti/DLC/DLC layer deposited onto MCMgAl6Zn1 a) bright field; b) dark field; c) diffraction pattern of area shown in a); d) part of solution for diffraction pattern shown in c

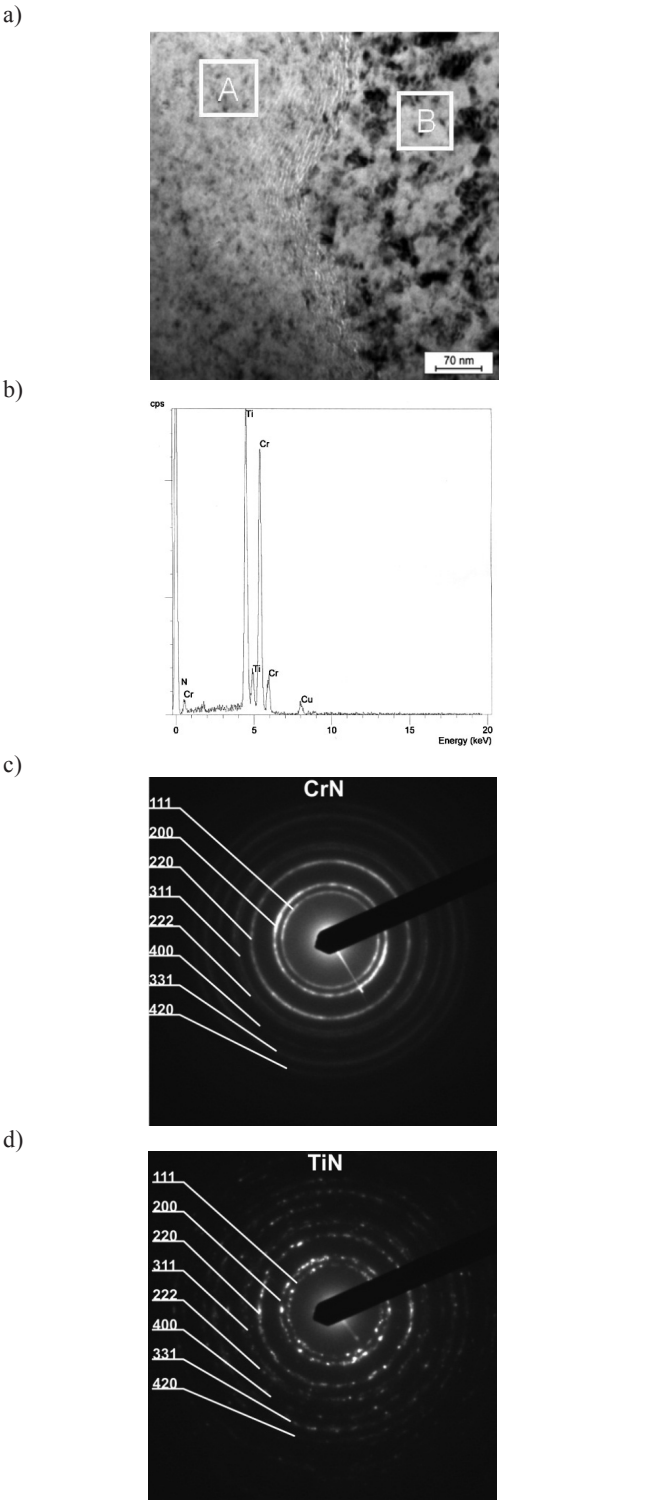

Fig. 80. TEM images of Cr/CrN/TiN layer deposited onto MCMgAl9Zn1 a) bright field; b) graph as a function of the intensity of the scattered X-rays from the area C shown in Figure a) c) diffraction pattern of area shown in a, area a; d) part of solution for diffraction pattern shown in a, area b

a)

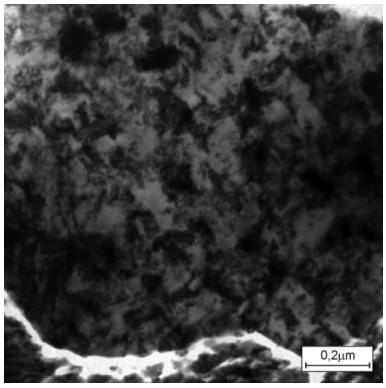

b)

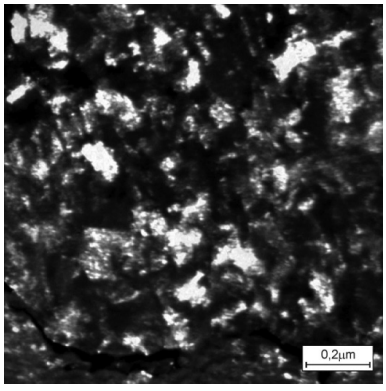

c)

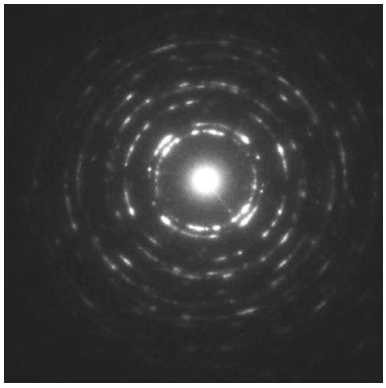

d)

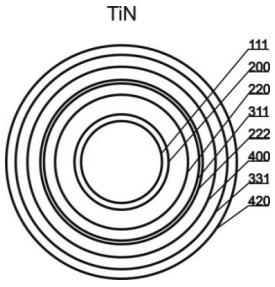

Fig. 81. TEM images of Cr/CrN/TiN layer deposited onto MCMgAl9Zn1 a) bright field; b) dark field; c) diffraction pattern of area shown in a); d) part of solution for diffraction pattern shown in c

As a result of quality and quantitative tests using X-ray microanalysis, done using energy-dispersive X-ray spectroscopy confirmed the presence of the main alloying elements, Mg, Al, Zn, Ti, Cr, C, N, Si, both included in the casting of tested magnesium alloys and prepared as a coating (Figures 82-85, Table 18), and information was obtained about the mass and atomic concentration of each element in spot tests in microareas of the coating and applied coatings.

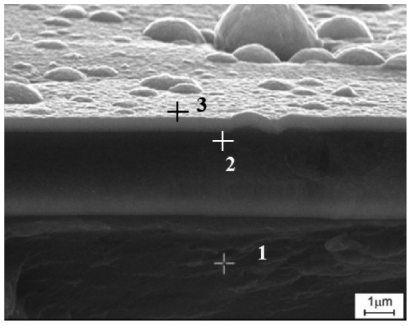

Fig. 82. Fracture topography of Ti/TiCN/CrN layer deposited onto MCMgAl6Zn1

a)

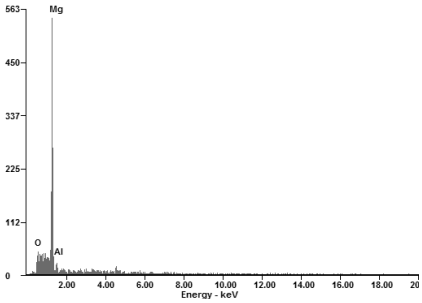

b)

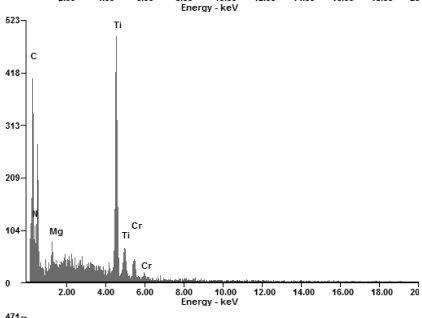

c)

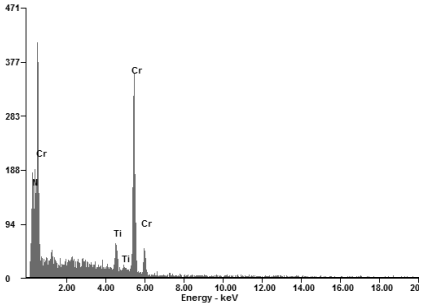

Fig. 83. EDS spectra of Ti/TiCN/CrN layer deposited onto MCMgAl6Zn1 alloy: a) analysis 1, b) analysis 2, c) analysis 3 from Fig. 82

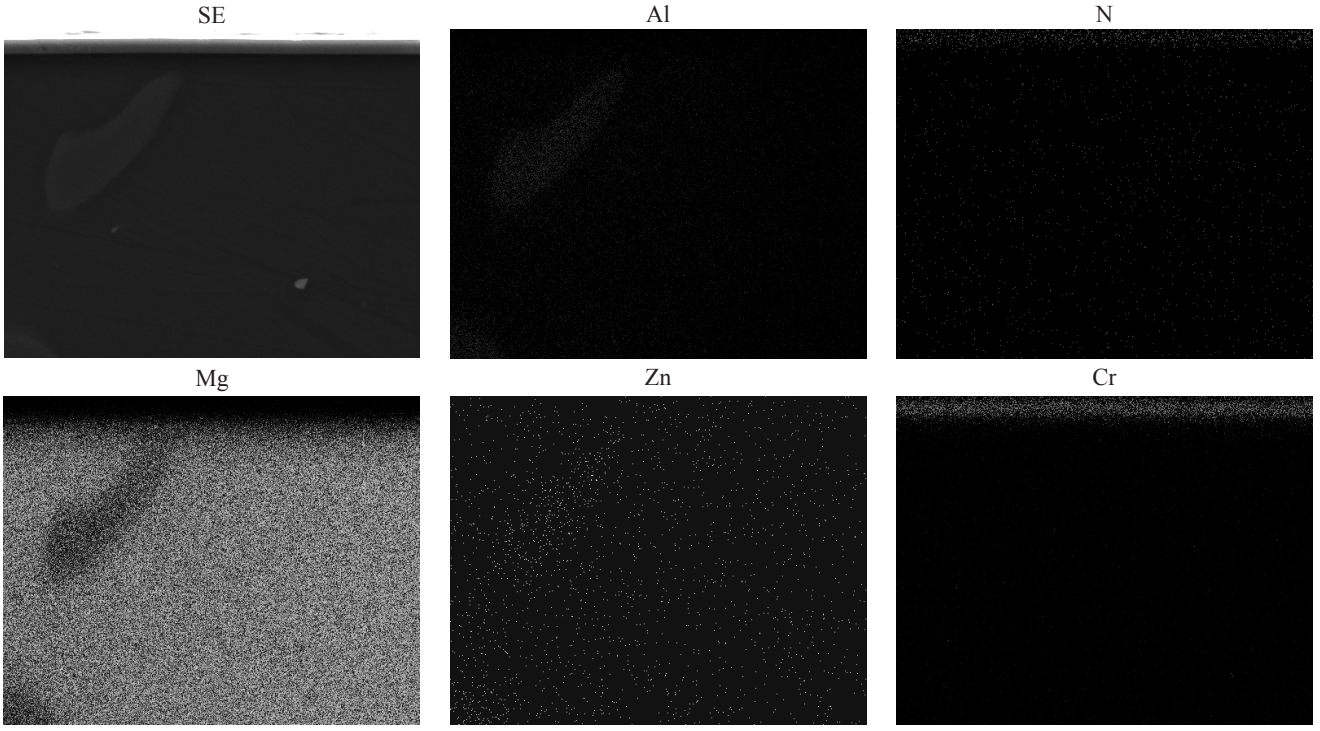

Fig. 84. Fracture topography of Ti/TiCN/CrN layer deposited onto MCMgAl6Zn1 magnesium alloy: image of secondary electrons (A) and maps of elements' distribution

In view of the fact that EDS analysis in the case of concentration measurements of the so-called light elements for which the energy <1 keV (C, N), due to the strong absorption, is fraught with relatively large measurement error, the described values should be treated as estimates only. However, the measurement error in the case of the mass concentration located in the range of 5 to 20% is approximately 4%, and over 20% of mass concentration of the element error is 2%. Since the size of individual elements of the structure is mostly smaller than the diameter of the analysing beam, the chemical composition obtained in the quantitative analysis of can be averaged, resulting in some of the concentration of elements possibly being overstated.

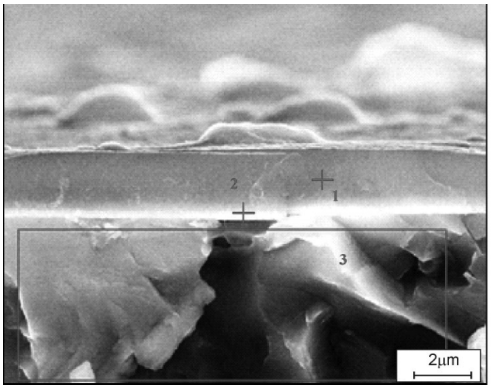

Fig. 85. Cross-section SEM images of the Ti/DLC/DLC coating deposited onto the MCMgAl9Zn1substrate

Qualitative analysis of surface distribution of elements made at the cross-section of tested samples clearly confirms the increase in the concentration of elements on the borders of coatings being formed (gradient/multicomponent) (Fig. 85, Table 18).

Table 18.
The results of quantitative chemical analysis from third 1, 2, 3 areas of coating Ti/DLC/DLC deposited onto substrate from MCMgAl9Zn1 alloy marked in Fig. 85

Element	The mass concentration of main elements, %	
	mass	atomic
	Analysis 1 (point 1)	
C	92.85	96.92
Mg	4.33	2.24
Al	0.52	0.24
Ti	2.29	0.6
	Analysis 2 (point 2)	
C	76.59	89.31
Zn	0.84	0.18
Mg	12.56	7.23
Al	1.55	0.81
Ti	8.46	2.47
	Analysis 3 (point 3)	
Zn	5.67	2.25
Mg	67.38	71.85
Al	26.95	25.9

Analysis of chemical composition, made using GDOES glow discharge spectrometer, confirms the presence of chemical elements included in the analysed layers in the coatings being formed (Fig. 86-88). The nature of changes in the joining area, i.e. the increase in the concentration of elements contained in the substrate, with a rapidly decreasing concentration of elements forming the coating, may indicate the existence of a transition layer between the substrate material and the coating, improving adhesion of coatings applied to the substrate, although these results cannot be interpreted unambiguously due to non-heterogeneous evaporation of material from the surface of the samples. Furthermore, using glow discharge optical spectrometer, the presence of an area of linearly varying concentration of elements contained in the tested coatings was confirmed, which indicates their gradient-like character (Figs. 86-88).

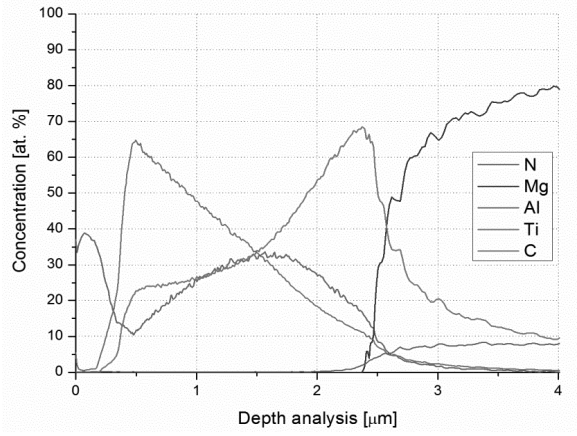

Fig. 86. Changes in concentrations of the chemical components of Ti/TiCN/TiAlN layer deposited onto MCMgAl9Zn1 magnesium alloy

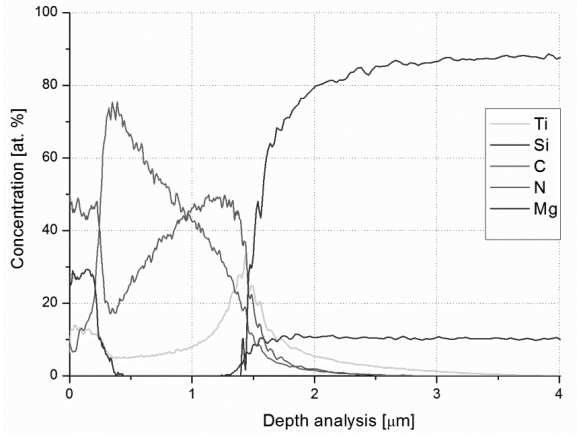

Fig. 87. Changes in concentrations of the chemical components of Ti/TiSiN/TiSiN layer deposited onto MCMgAl9Zn1 magnesium alloy

Qualitative analysis of the phase composition, made using Bragg-Brentano X-ray diffraction technique, helped confirm the correctness of the produced coatings of TiN, (Ti, Al) N, (Ti, Si) N, TiCN, CrN (Figs. 89, 90).

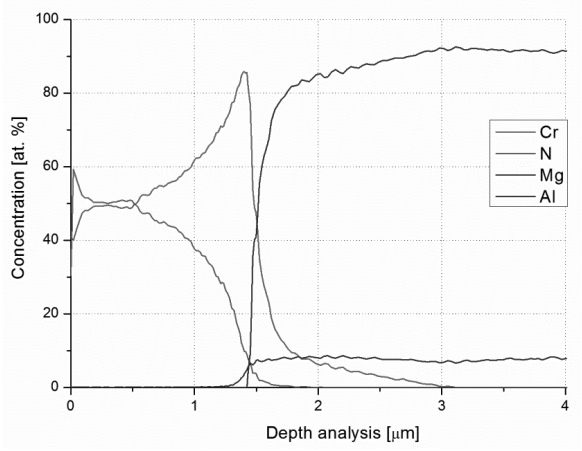

Fig. 88. Changes in concentrations of the chemical components of Cr/CrN/CrN layer deposited onto MCMgAl9Zn1 magnesium alloy

Due to the overlapping of reflections of the substrate material and the coating, relatively small thickness of the individual layers up to 3.5 μm, as well as the identical character of Miller indices (hkl) for TiCN and (Ti, Al)N type coatings hindered the identification of individual phases. The presence of reflections was found originating from phases present in the substrate, i.e. α-Mg and γ-$Mg_{17}Al_{12}$. Scarce volume share of remaining phases present in the substrate material does not allow for their unambiguous identification of X-ray diffractograms. The presence of reflections from the substrate was found at all coating diffractograms, which is caused by the thickness of the coatings, smaller X-ray penetration depth into the material. In order to obtain more accurate information from the analysed coating surface layer, in further tests the technique of diffraction at a constant angle of the primary X-ray beam (SKP) was used. At various angles of incidence of the primary beam, reflections were recorded only from the thin surface layers (Figs. 89, 90).

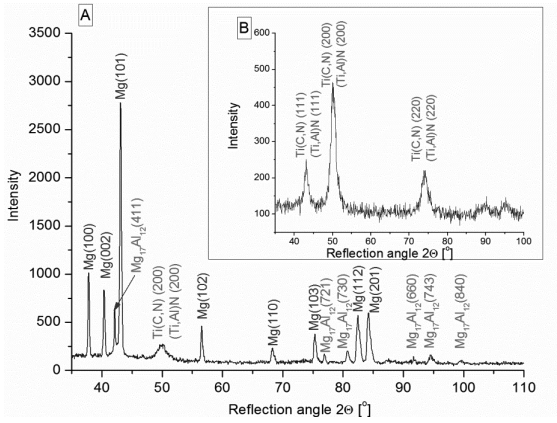

Fig. 89. (A) X-Ray diagrams of the Ti/TiCN/TiAlN layers coated on the MCMgAl9Zn1 magnesium alloy, obtained using the Bragg-Brentano method (B) X-Ray diagrams of the coating performer in a sTable angle of α=4°

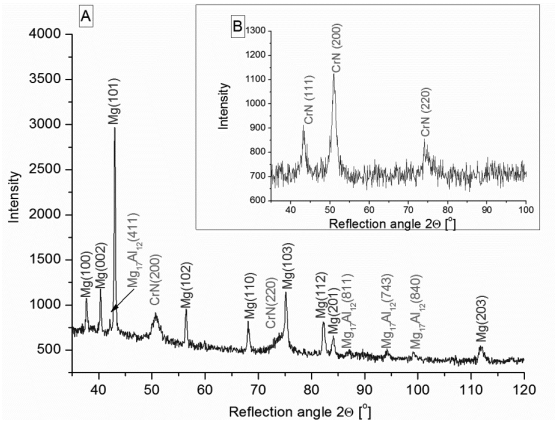

Fig. 90. (A) X-Ray diagrams of the Cr/CrN/CrN layers coated on the MCMgAl6Zn1 magnesium alloy, obtained using the Bragg-Brentano method (B) X-Ray diagrams of the coating performer in a sTable angle of α=4°

Testing roughness R_a casting surfaces of coated magnesium alloys confirms no significant effect of the type of substrate on the parameter of surface roughness, which may indicate that differences in the measured roughness parameters on different substrates from magnesium alloys for different coatings are at most 0.05μm (Table 19). The lowest values of surface roughness in the range of 0.12 to 0.18 μm were measured in coatings with a gradient layer of a chromium nitride, which is probably due to the presence of microparticles in the shape of the solidified droplets on the surface of the coating. The general range of surface roughness of coated materials is in the range 0.12 to 0.32 μm (Table 19).

On the basis of surface microhardness tests of the analysed casting of magnesium alloys, coated and uncoated by tested coatings, there was a significant increase in the microhardness after surface treatment from vapour deposition. The measured microhardness for magnesium alloys casting: MCMgAl3Zn1, MCMgA16Znl, MCMgAl9Zn1, MCMgA112Znl not covered by tested coatings was, respectively, 82, 98, 133 and 153 HV. All of the analysed cases of coatings being formed should be considered separately, but two groups can be distinguished on the basis of hardness tests carried out, i.e. the coatings with microhardness up to 2000 HV CrCrN/CrN, Cr/CrN/TiN and Ti/TiSiN/TiSiN type, and Ti/TiCN/CrN, Ti/TiCN/TiAlN and Ti/DLC/DLC type coatings, characterized by the values of measured hardness at 2000-2700 HV, which also strongly correlates with the resistance of these coatings to abrasion (Table 19).

Identification of abrasion resistance of the tested hybrid coatings on cast magnesium alloy substrate was made on the basis of the abrasion resistance test (ball-on-disk) under conditions of dry friction in the configuration of the horizontal axis of rotation of the disc with the use of tungsten carbide ball as counter-sample. The tests allowed to investigate in a precise manner the wear resistance and friction coefficient for any combination (coating-counter sample), depending on the sweep speed, surface pressure, atmospheric conditions and other factors (Table 20). During the tribological resistance tests of produced coatings, the graphs were drawn, recording the relationship between friction coefficient and/or displacement of the counter-sample in the vertical axis, depending on the number of rotations of the disc or friction distance of the counter-sample until the coating was rubbed through. For all recorded friction coefficient curves, depending on the number of rotations or the friction distance, a similar characteristics was determined, which can be divided into two parts (Fig. 91). In the first part, friction coefficient increased dramatically with the increase of the friction distance. It was assumed to be a transient state of the process of friction. The second part of the graph is similar to the steady state. Rapid changes in the friction coefficient recorded during the test were caused by chipping from the sample and counter-sample.

Table 19.
Results of R_a and microhardness HV measurements of analysed coatings deposited on magnesium alloys

Coating type	Property	MCMgAl3Zn	MCMgAl6Zn	MCMgAl9Zn	MCMgAl12Zn
Cr/CrN/CrN	Roughness R_a, μm	0.12	0.15	0.12	0.13
	Microhardness HV	1913.5	1927.2	1915.25	1925.25
Cr/CrN/TiN	Roughness R_a, μm	0.18	0.18	0.15	0.17
	Microhardness HV	1698.2	1681	1700.725	1684.15
Ti/DLC/DLC	Roughness R_a, μm	0.26	0.25	0.25	0.24
	Microhardness HV	2754.05	2732.8	2693.25	2669.8
Ti/Ti(C,N)/CrN	Roughness R_a, μm	0.27	0.28	0.26	0.25
	Microhardness HV	2019.2	2029.8	2041.75	2021.5
Ti/Ti(C,N)/(Ti,Al)N	Roughness R_a, μm	0.28	0.3	0.27	0.28
	Microhardness HV	2169.7	2180.6	2124.1	2167.7
Ti/(Ti,Si)N/(Ti,Si)N	Roughness R_a, μm	0.32	0.31	0.28	0.26
	Microhardness HV	1770	1763.3	1721.6	1770
Substrate	Microhardness HV	82	98	133	153

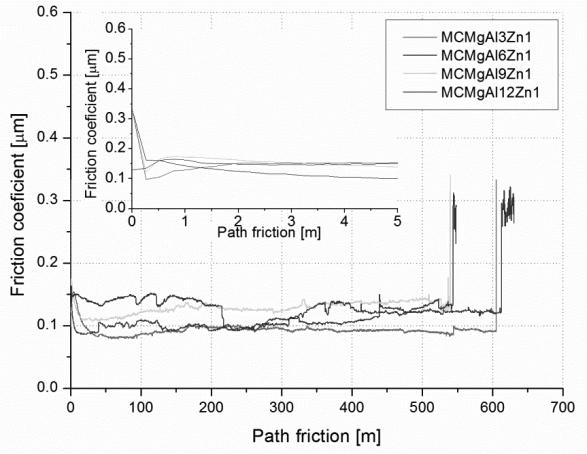

Fig. 91. The dependence of the coating friction coefficient of the counterspecimen path friction obtained from the abrasion resistance ball-on-disk method of Ti/DLC/DLC layer deposited on analysed magnesium alloys

Friction distance values obtained are within a wide range of 5.3 to 630 m (Table 20). Comparing the results of the friction coefficient and friction distance, it was found that the best wear resistance is characteristic for DLC carbon coated materials, which also have the highest microhardness. In accordance with the applied load of 5 N, the average friction coefficient of DLC coatings obtained with planning speed 0.05 m/s was within 0.08-0.15 µm, respectively lower in magnitude compared to friction coefficient of other tested coatings. Such a condition is typical of DLC type coatings consisting of graphite, which is in the process of abrasion acts as a lubricant, depositing on the counter-sample. Furthermore, high speed of travel and the associated heat accumulation makes it easier to create a self-lubricating layer, which further results in a lower friction coefficient [81]. The friction distance results for DLC coatings were at a level exceeding even 70 times the friction distance results for such coatings as Cr/CrN/CrN (Table 20).

The lowest force at which the coating is damaged, called critical load L_C as a measure of adhesion of the coating to the substrate was identified in a scratch test. L_{C1} and L_{C2} coefficients were determined based on the variation of acoustic emission value recorded during the measurement, generated at the interface of the indenter and a test sample, and on the basis of measuring the friction force of the diamond indenter and metallographic observation under a light microscope coupled with a measuring device (Fig. 92, 93).

Table 20.
Results of path friction, friction coefficient min. and friction coefficient max. measurements of analysed coatings deposited on magnesium alloys

Coating type	Parameter	MCMgAl3Zn	MCMgAl6Zn	MCMgAl9Zn	MCMgAl12Zn
Cr/CrN/CrN	Path friction, m	13	22	7.8	8
	Friction coefficient min, µm	0.208	0.308	0.228	0.21
	Friction coefficient max, µm	0.306	0.458	0.383	0.281
Cr/CrN/TiN	Path friction, m	9.4	11.9	7.8	6
	Friction coefficient min, µm	0.11	0.152	0.13	0.14
	Friction coefficient max, µm	0.371	0.425	0.433	0.381
Ti/DLC/DLC	Path friction, m	605	630	540	550
	Friction coefficient min, µm	0.079	0.086	0.107	0.09
	Friction coefficient max, µm	0.154	0.162	0.177	0.164
Ti/Ti(C,N)/CrN	Path friction, m	52.3	57	46.3	48.6
	Friction coefficient min, µm	0.166	0.15	0.22	0.249
	Friction coefficient max, µm	0.386	0.322	0.304	0.335
Ti/Ti(C,N)/(Ti,Al)N	Path friction, m	66	77.7	57.6	59.4
	Friction coefficient min, µm	0.165	0.17	0.178	0.191
	Friction coefficient max, µm	0.221	0.217	0.334	0.31
Ti/(Ti,Si)N/(Ti,Si)N	Path friction, m	11	16.2	8.9	6.6
	Friction coefficient min, µm	0.165	0.151	0.14	0.141
	Friction coefficient max, µm	0.296	0.333	0.391	0.29

The critical load L_{C1} is noted on the chart recording relationships between the friction force, acoustic emission and load, as the first small leap in acoustic emission signal. In contrast, the critical load L_{C2} refers to the point of delamination of coating, where there are cracks, chipping, delamination on the outside and inside of the scratch with uncovering the substrate material; the sound signal also increases. All the results obtained are grouped and presented in Table 21. The highest values of the critical load, L_{C1} and L_{C2} 7 and 19 N, respectively, and thus, the best adhesion of the coating to the substrate was obtained for Ti/DLC/DLC coating formed on the MCMgAl9Zn1 substrate. Other measured values of the critical load demonstrating coating to the substrate adhesion do not exceed 14 N (Table 21).

a)

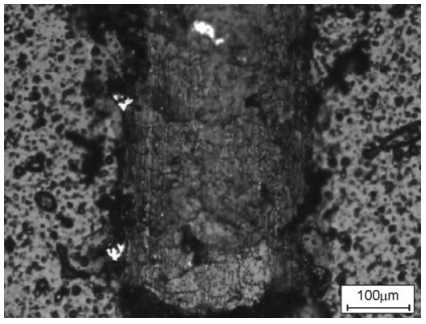

b)

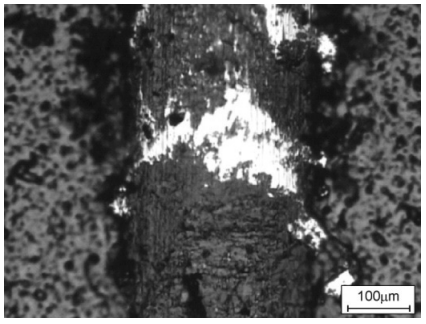

Fig. 92. Scratching traces of the Ti/TiCN/TiAlN layer deposited onto MCMgAl6Zn1 alloys at diamond penetrator at scratch test method at critical load: (a) L_{C1}, (b) L_{C2}

a)

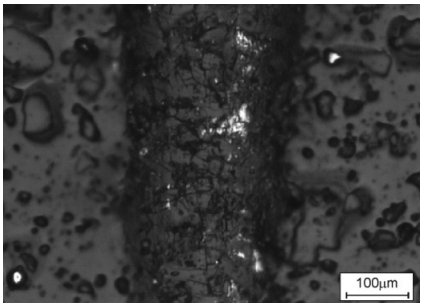

b)

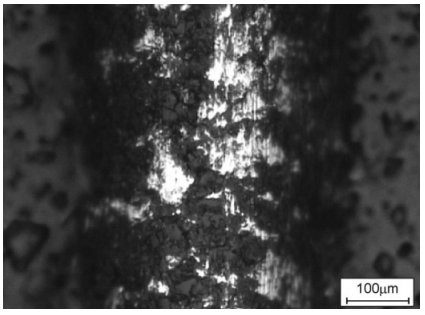

Fig. 93. Scratching traces of the Ti/DLC/ DLC layer deposited onto MCMgAl6Zn1 alloys at diamond penetrator at scratch test method at critical load: (a) L_{C1}, (b) L_{C2}

Pitting corrosion resistance of coatings formed on casting of magnesium alloys was evaluated on the basis of registration of anodic polarization curves, using the potentiodynamic method in 1M aqueous solution of NaCl. The test was initiated from potential $E_{pocz} = E_{OCP-100}$ mV. The change in potential was in the anode direction, at a rate of 1 mV/s After reaching the maximum anode current density of 100 mA/cm^2, the sample was kept polarized at the obtained potential for 1 minute, then the direction of polarization was changed. This method is one of the primary ways of determining corrosion resistance of structural engineering materials. On the basis of the recorded anodic polarization curves, characteristic values describing the resistance to pitting corrosion were determined, i.e. the corrosion potential E_{kor} (mV), polarization resistance R_p ($\Omega \cdot cm^2$), corrosion current density i_{kor} ($\mu A/cm^2$) (Figs. 94, 95, Table 22).

Table 21.
Results of L_{C1} i L_{C2} measurements of analysed coatings deposited on cast magnesium alloys

Coating type	Parameter	MCMgAl3Zn	MCMgAl6Zn	MCMgAl9Zn	MCMgAl12Zn
Cr/CrN/CrN	L_{C1}, N	4	5	5	2
	L_{C2}, N	12	11	12	10
Cr/CrN/TiN	L_{C1}, N	4	5	4	5
	L_{C2}, N	10	14	8	9
Ti/DLC/DLC	L_{C1}, N	4	7	6	5
	L_{C2}, N	12	19	17	15
Ti/Ti(C,N)/CrN	L_{C1}, N	5	4	3	4
	L_{C2}, N	10	13	8	11
Ti/Ti(C,N)/(Ti,Al)N	L_{C1}, N	3.5	4	3	4
	L_{C2}, N	10.5	11	10	10
Ti/(Ti,Si)N/(Ti,Si)N	L_{C1}, N	4	4	5	3
	L_{C2}, N	12	12	11	10

Table 22.
Results of E_{kor}, R_p and i_{kor} measurements of analysed coatings deposited on cast magnesium alloys

Coating type	Parameter	MCMgAl3Zn	MCMgAl6Zn	MCMgAl9Zn	MCMgAl12Zn
Cr/CrN/CrN	E_{kor}, mV	-1560	-1543.2	-1547	-1409.6
	R_p, Ω·cm^2	127.04	98.7	146.87	346.51
	i_{kor}, μA/cm^2	204.66	263.3	177	75
Cr/CrN/TiN	E_{kor}, mV	-1505.8	-1536.6	-1521.3	-1495.4
	R_p, Ω·cm^2	34.54	33.78	78.14	92.91
	i_{kor}, μA/cm^2	752.52	769.69	332.74	279
Ti/DLC/DLC	E_{kor}, mV	-1557.8	-1571.5	-1584.1	-1510.8
	R_p, Ω·cm^2	123.56	206	194.99	896.86
	i_{kor}, μA/cm^2	210.42	126.21	133.34	28.99
Ti/Ti(C,N)/CrN	E_{kor}, mV	-1515.4	-1522.4	-1525.6	-1475.9
	R_p, Ω·cm^2	60.64	26.63	28.13	53.49
	i_{kor}, μA/cm^2	428.76	976.34	924.28	486.1
Ti/Ti(C,N)/(Ti,Al)N	E_{kor}, mV	-1534.5	-1539.2	-1529.4	-1535.3
	R_p, Ω·cm^2	24.06	27.95	13.43	44.81
	i_{kor}, μA/cm^2	1080.63	930.23	1935.96	580.23
Ti/(Ti,Si)N/(Ti,Si)N	E_{kor}, mV	-1567.8	-1586.1	-1534.5	-1531.7
	R_p, Ω·cm^2	19.59	50.33	38.13	16.82
	i_{kor}, μA/cm^2	1327.21	516.59	681.8	1545.7
Podłoże	E_{kor}, mV	-1420.5	-1597	-1571.4	-1555.6
	R_p, Ω·cm^2	111.95	91.64	56.57	81.16
	i_{kor}, μA/cm^2	230	280	460	320

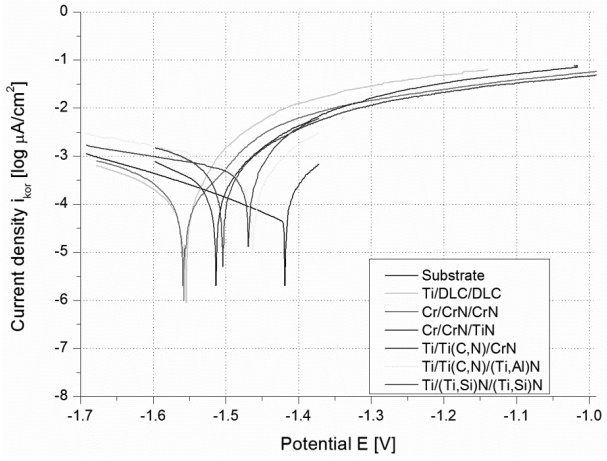

Fig. 94. Anodic curves of analysed coatings deposited on MCMgAl3Zn1 magnesium cast alloys

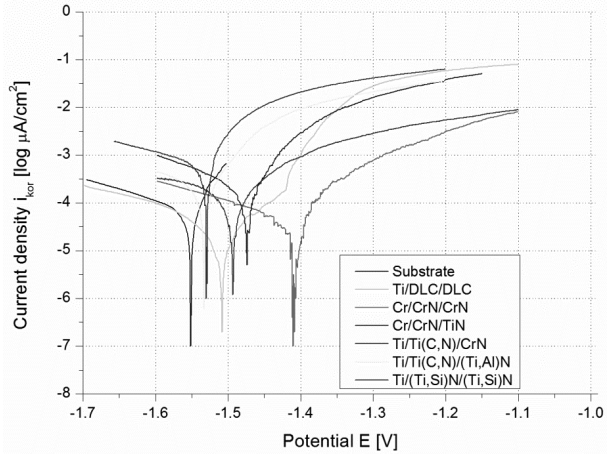

Fig. 95. Anodic curves of analysed coatings deposited on MCMgAl12Zn1 magnesium cast alloys

In the course of potentiodynamic tests, analysing the polarization curves for different magnesium alloys with applied layers it was found that there is no repassivation in the passive range, and the coatings undergo pitting corrosion in the tested environment. On the basis of the recorded electrochemical corrosion test results for casting magnesium alloys: MCMgAl3Zn1, MCMgA16Znl, MCMgAl9Zn1, MCMgA112Znl, covered by analysed types of coatings: Ti/TiCN/CrN, Ti/TiCN/TiAlN, Cr/CrN/CrN, Cr/CrN/TiN, Ti/TiSiN/TiSiN and Ti/DLC/DLC type it was found that the best electrochemical properties, in the course of corrosion tests in 1 M NaCl solution, were characteristic of Ti/DLC/DLC, and Cr/CrN/CrN type coatings, for which the lowest values of corrosion current densities were recorded (Table 22).

Identification of damage to coating resulting from corrosion tests was done on the basis of observations in Zeiss LSM 5 Exciter confocal scanning microscope and Zeiss Discovery V12 SteREO stereoscopic light microscope. Pitting corrosion is generally defined as a type of local corrosion because cavities are often invisible at the stage of their generation, and the measured loss of weight compared to general corrosion is small, but in the long term it also leads to perforation of the surface, and thus, destruction of the element. Nucleation and growth of pits occur in the most vulnerable places in a passive layer (in the areas of potential corrosion centres) forming on the surface of metallic materials, such as in the vicinity of mechanical damages, near

structural solidification, pores, solidified drops of deposited material (CAD PVD), depressions remaining after fall-out drops on grain boundaries. Based on metallographic tests, in the tested structure and surface coatings from casting magnesium alloy, open corrosion pitting was identified, typical for hard passivating materials of different shapes - from cylindrical to hemispherical, depending on the type of coating, substrate, and the corrosive environment and polarization conditions, in the smallest number visible in case of Cr/CrN/CrN and Ti/DLC/DLC coatings (Figs. 96-99). In view of the fact that pitting surface is the anode (pitting environment is the cathode) in the bottom of the pitting corrosion products can be identified following the resulting dissolution of the tested material.

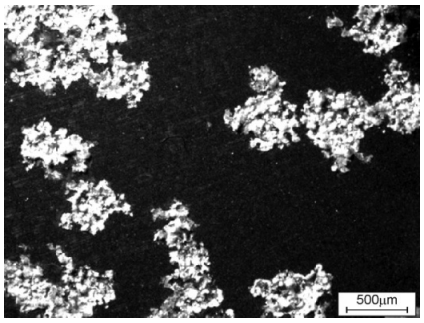

Fig. 96. Surface structure of Cr/CrN/CrN layer deposited onto MCMgAl9Zn1 after corrosion test, mag 15x

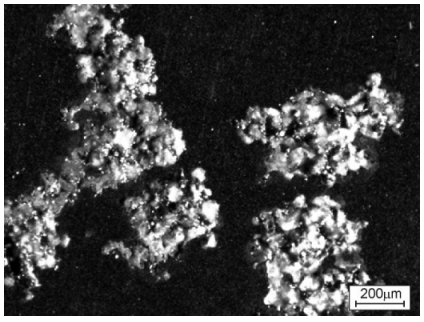

Fig. 97. Surface structure of Cr/CrN/CrN layer deposited onto MCMgAl9Zn1 after corrosion test, mag 30x

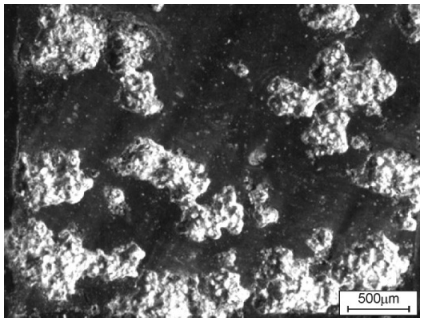

Fig. 98. Surface structure of Ti/DLC/DLC layer deposited onto MCMgAl6Zn1 after corrosion test, mag 15x

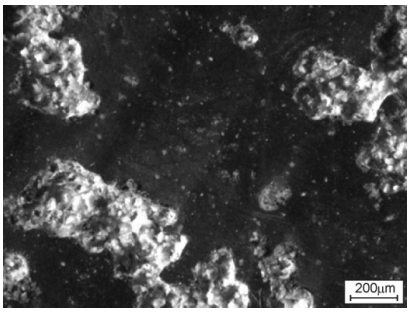

Fig. 99. Surface structure of Ti/DLC/DLC layer deposited onto MCMgAl6Zn1 after corrosion test, mag 30x

3.4. Structure and properties of Mg-Al-Zn after laser treatment

The shape of the stitch face of casting magnesium alloys MCMgAl3Zn1, MCMgAl6Zn1, MCMgAl9Zn1, MCMgAl12Zn1 after carbide laser and aluminium oxide fusing, using HPDL - a high power diode laser is shown in Figures 100-105. There was a significant effect of the process conditions, in particular of the laser beam power and particles of the powders used, on the shape of the face surface topography. After fusing TiC and WC powders, with the use of a feeder, face surface has a high regularity without visible cracks and burrs on the sides of the stitch (Figs. 100, 101). In the case of VC, the melting surface has a flat shape, but with visible discontinuities in the surface layer (Fig. 102). Metallographic examination confirmed that for the SiC particles used, the resulting quasi-composite layer has a protrusion of the melted zone, visible above the substrate material surface (Fig. 103). In contrast to the technique of powder fusing titanium carbide and tungsten carbide, the surface of the tested materials from magnesium alloys obtained by fusing niobium carbide has a high irregularity and visible material flashes to the sides of the stitch (Fig. 104). However, in case of fusing Al_2O_3 powder particles, small cavities can be identified recess in the mid-area of the stitch face for the laser power of 1.6 and 2.0 kW (Fig. 105).

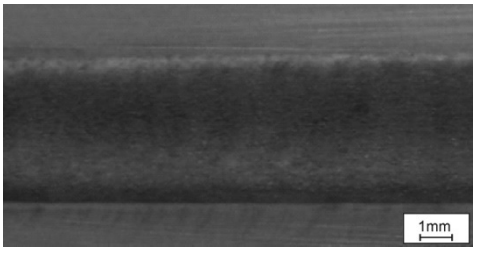

Fig. 100. Surface layer face of MCMgAl3Zn1 alloy after alloying by TiC, laser power 1.2 kW, scanning speed 0.75 m/min

Few irregularities and cavities in the surface layer of the analysed Mg-Al-Zn casting magnesium alloys with laser-melted particles are formed as a result of intense heating of the surface. Depending on the type of substrate, laser power, melting rate, and the powder used, the surface is heated unevenly, which has a direct

impact on the formation of the molten material in the remelting pool. Some of the alloy material is evaporated under high temperature prevailing during the laser treatment, hence the characteristic recesses in the middle of remelting of the obtained layers.

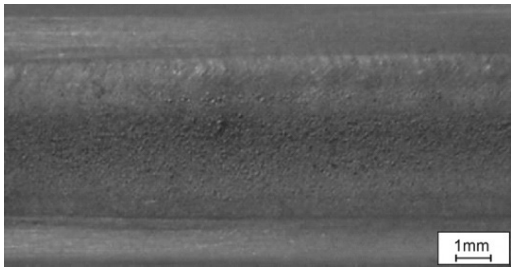

Fig. 101. Surface layer face of MCMgAl3Zn1 alloy after alloying by WC, laser power 1.6 kW, scanning speed 0.75 m/min

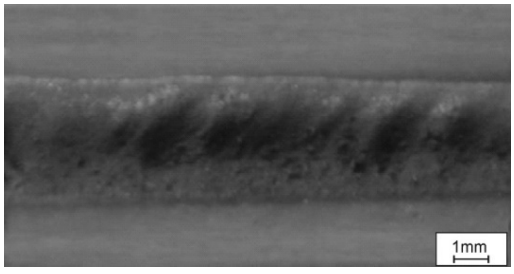

Fig. 102. Surface layer face of MCMgAl3Zn1 alloy after alloying by VC, laser power 1.6 kW, scanning speed 0.75 m/min

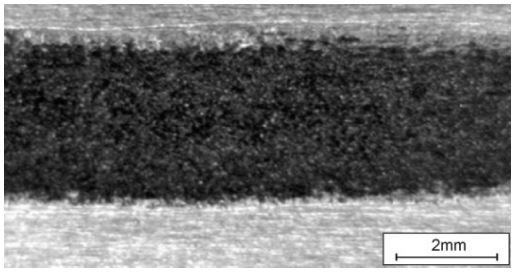

Fig. 103. Surface layer face of MCMgAl3Zn1 alloy after alloying by SiC, laser power 1.6 kW, scanning speed 0.75 m/min

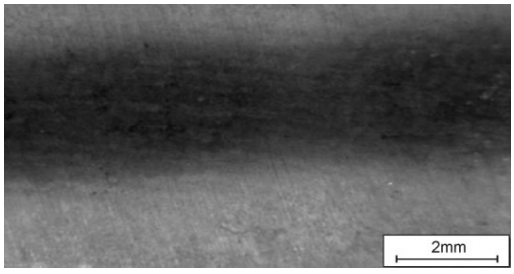

Fig. 104. Surface layer face of MCMgAl3Zn1 alloy after alloying by NbC, laser power 1.6 kW, scanning speed 0.25 m/min

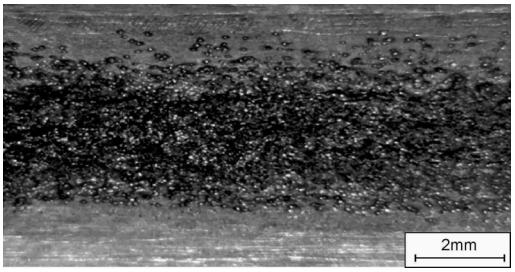

Fig. 105. Surface layer face of MCMgAl6Zn1 alloy after alloying by Al_2O_3, laser power 1.6 kW, scanning speed 0.50 m/min

On the basis of measurement of surface roughness of magnesium casting alloys, after laser fusing of tungsten, vanadium, silicon, carbides and aluminium oxide (Table 23) it was found that regardless of the ceramic powder, the roughness of the top layers resulting from the melting of Mg-Al-Zn magnesium alloys with a laser beam in the power range of 1.2-2.0 kW is increased, in comparison to the untreated surface roughness, and takes the values in the range of R_a=6.4-42.5 µm.

For each of the substrate (independently of the concentration of aluminium) samples after laser fusing speed of 0.5 m/min, and power of 2.0 kW are characterized by the highest surface roughness. While maintaining constant speed and at a constant intensity of powder feed, with the increase of the laser power surface roughness is reduced. Among Mg-Al-Zn casting magnesium alloys, the smallest roughness, respectively 4.0 and 5.6 microns was noted in materials: MCMgAl9Zn1 and MCMgAl12Zn1 after VC powder fusing, at applied laser power of 2.0 kW. Maximum measured surface roughness of R_a=42.5 µm occurs in a surface layer of MCMgAl9Zn1 alloy, after SiC powder fusing at laser power of 1.2 kW. The increase in surface irregularities after laser treatment is related to the fluctuation in the fused material, induced by voltage changes in the re-melted material, and energy absorption of laser radiation by the fused material.

Figures 106-109 show the configuration of the areas at the melting bead cross-section of Mg-Al-Zn casting magnesium alloys. On the basis of metallographic tests, the occurrence of re-melting zone (SP) and heat affected zone (HAZ) was found in each layer of the surface after the laser surface treatment of the tested MCMgAl12Zn1 and MCMgAl9Zn1 casting magnesium alloys. These zones, depending on the laser power and the ceramic powder, have different thickness and shape. In the case of fusing TiC, WC and VC powders of MCMgAl6Zn1 alloys, minimal heat affected zone was found, which increases with increasing laser power. In case of fusing powders into the surface of MCMgAl3Zn1 alloys, only a melting area is created between re-melting zone and parent material (Fig. 106). As a result, metallographic tests, it can be concluded that the change in laser power at a constant fusing speed significantly influences the increase in thickness of both arras in the surface layer. Laser power will also affect the shape and protrusion of the re-melted zone (Fig. 107), rising above the surface of the treated material.

Table 23.
Influence of laser power on R_a of analysed magnesium alloys after alloying

	Laser power, kW	TiC	WC	VC	SiC	Al_2O_3
MCMgAl3Zn1	1.2	7.57	15.63	23	--	--
	1.6	6.4	8.3	6.27	15.3	--
	2	9.2	7.83	5.93	16.5	25.4
MCMgAl6Zn1	1.2	9.75	14.3	14.7	--	--
	1.6	8.15	7.3	5.35	18.6	24.4
	2	8.84	4.45	5.77	21.9	21.4
MCMgAl9Zn1	1.2	5.8	7.4	6.7	42.5	--
	1.6	8.48	10.93	6.3	13.7	27.3
	2	12.92	8.43	4.03	18.3	25.3
MCMgAl12Zn1	1.2	8.3	9.07	13.32	25.5	--
	1.6	9.1	10.8	9.9	17.1	17.7
	2	13.9	8.07	4.97	19.2	17.1

Table 24.
Influence of laser power on SP and SWC of analysed magnesium alloys after alloying

	Moc lasera, kW	Strefa [mm]	TiC	WC	VC	SiC	NbC	Al_2O_3
MCMgAl3Zn1	1.2	SP	0.61	0.45	0.7	--	--	--
		SWC	--	--	--	--	--	--
	1.6	SP	0.72	0.86	1.02	0.6	--	--
		SWC	--	--	--	0.01	--	--
	2	SP	0.92	1.16	1.42	1.6	1.1	--
		SWC	--	--	--	0.1	--	--
MCMgAl6Zn1	1.2	SP	0.74	0.53	0.9		--	--
		SWC	0.02	0.02	0.31	--	--	--
	1.6	SP	0.91	0.63	1.79	1.6	1.2	0.1
		SWC	0.04	0.03	0.27	0.1	--	--
	2	SP	1.51	1.36	1.86	1.8	1.5	0.5
		SWC	0.96	0.12	0.48	0.3	0.1	--
MCMgAl9Zn1	1.2	SP	0.72	0.94	1.46	0.7	--	--
		SWC	0.6	0.57	0.46	0.7	--	--
	1.6	SP	1.46	1.12	1.59	1.6	1.1	0.2
		SWC	0.74	0.72	0.57	0.8	0.9	0.4
	2	SP	1.87	1.52	1.63	2	1.4	1.6
		SWC	0.61	0.82	0.68	1.2	0.9	1.8
MCMgAl12Zn1	1.2	SP	1.07	1.28	1.25	1.1	--	--
		SWC	0.41	0.45	0.43	0.5	--	--
	1.6	SP	1.41	1.67	1.46	2.8	1.4	0.8
		SWC	0.6	0.67	0.6	0.7	0.8	0.7
	2	SP	1.85	1.63	1.7	2.2	1.5	2.3
		SWC	0.61	0.54	0.55	1.2	0.8	1.6

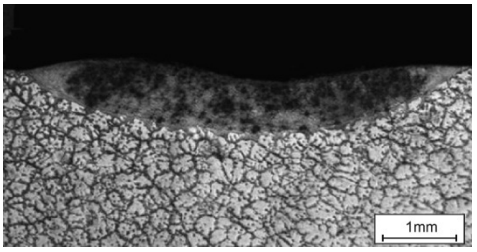

Fig. 106. The surface layer of MCMgAl3Zn1 alloy after alloying by WC, laser power 1.6 kW, scanning speed 0.75 m/min

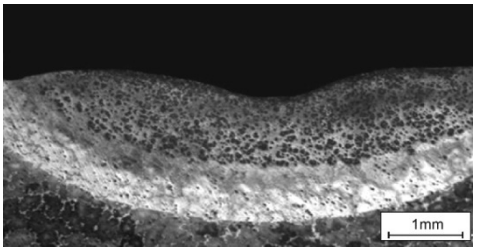

Fig. 107. The surface layer of MCMgAl12Zn1 alloy after alloying by TiC, laser power 1.6 kW, scanning speed 0.75 m/min

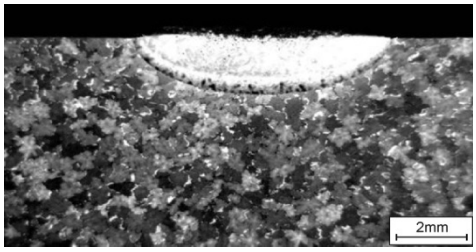

Fig. 108. The surface layer of MCMgAl12Zn1 alloy after alloying by SiC, laser power 1.6 kW, scanning speed 0.75 m/min

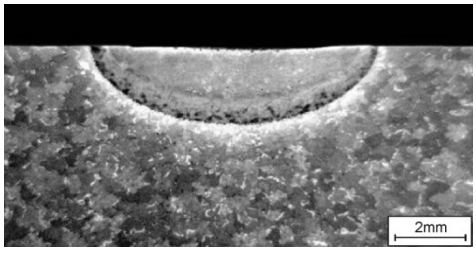

Fig. 109. The surface layer of MCMgAl12Zn1 alloy after alloying by Al_2O_3, laser power 2.0 kW, scanning speed 0.75 m/min

Detailed results of thickness measurements of SP and SWC areas as a function of changes in laser power and the type of powders used are shown in Table 24.

Our findings clearly confirm the proportional effect of laser power on thickness of both the re-melting zone and the heat affected zone. The thickness of coatings, evaluated on the basis of computer image analysis performed on light microscopy images, and confirmed by tests in a scanning electron microscope, is within a wide range, and is a function of four variables, namely: laser beam power, fusing rate, type of fused material, and the type of substrate. The biggest surface layer thickness was measured after fusing SiC and NbC powder, at laser power of 2.0 kW for MCMgAl12Zn1 alloy, respectively, 3590 µm and 3950 µm. For other powders, the biggest greatest thickness of the surface layer obtained for MCMgAl9Zn1 and MCMgAl12Zn1 alloys is in the range of 2340-2470 µm. The smallest thickness of the surface layer in the laser-melted samples are to be found in magnesium casting alloys at 3% aluminium concentration (MCMgAl3Zn1). This melted area of those materials, after tungsten, titanium, vanadium, carbides fusing at 1.2 kW laser power is in the range of 450-720 µm.

The results of metallographic examination showed that the structure of the solidifying material after laser fusing is characterized by areas of different morphology associated with crystallization of magnesium alloys (Figs. 110-115). Multiple changes in direction of crystal growth is observed, characteristic for those areas. In the area at the boundary between the solid and liquid phases, there are small dendrites, whose main axes are oriented along the lines of heat dissipation. Much smaller crystal size in that area, compared to the central part of the re-melting, is related to the initiation of the solidification process in the insoluble phases comprising partially the matrix, an in partly re-melted grains of the native metal. The next stages of crystal growth are closely related to the behaviour of preferred orientation - the direction of crystal growth corresponds to the direction of the largest temperature gradient, assuming that the volume of the material of the entire sample takes over heat from the process of re-melting/fusing. As a result of laser fusing, a structure is formed free from defects with a clear fragmentation of native material grains, containing predominantly dispersive particles of TiC, WC, VC, SiC, NbC carbide used or Al_2O_3 (Figs. 110 and 111 and 113 and 114).

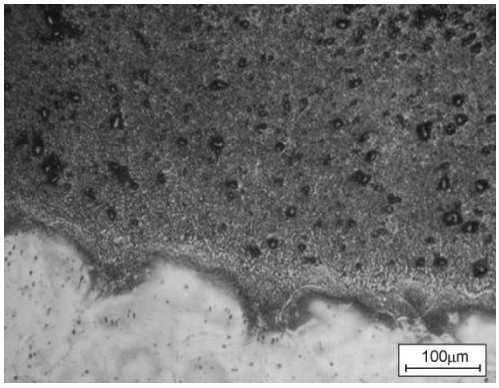

Fig. 110. The boundary remelting of MCMgAl6Zn1 after alloying by TiC, laser power 1.6 kW, scanning speed 0.75 m/min

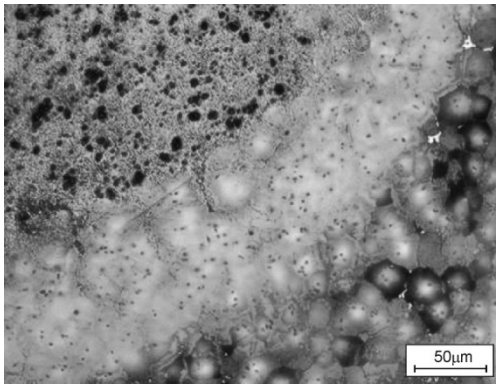

Fig. 111. The boundary remelting of MCMgAl12Zn1 after alloying by WC, laser power 2.0 kW, scanning speed 0.75 m/min

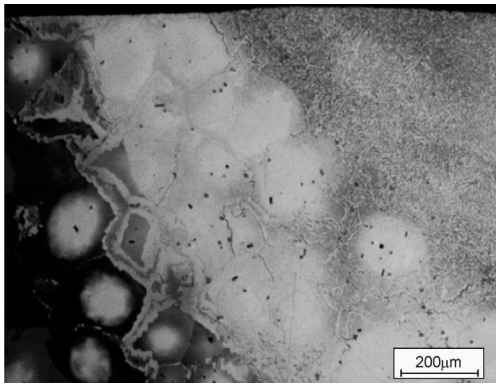

Fig. 112. The boundary remelting of MCMgAl9Zn1 after alloying by Al_2O_3, laser power 1.6 kW, scanning speed 0.5 m/min

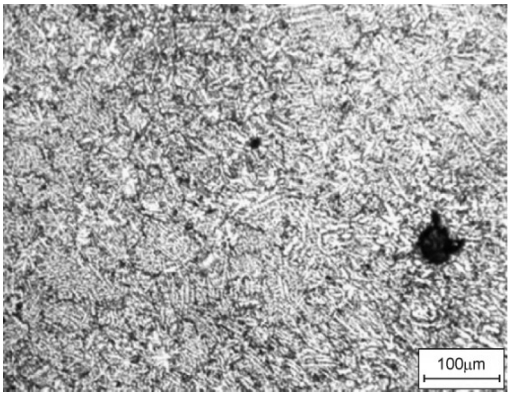

Fig. 113. Central zone of MCMgAl12Zn1 alloy after alloying by VC, laser power 2.0 kW, scanning speed 0.75 m/min

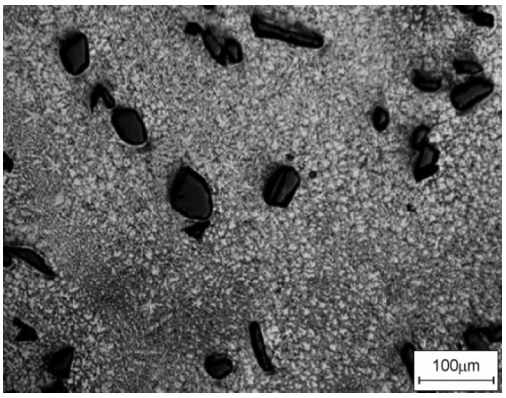

Fig. 114. Central zone of MCMgAl6Zn1 alloy after alloying by SiC, laser power 2.0 kW, scanning speed 0.75 m/min

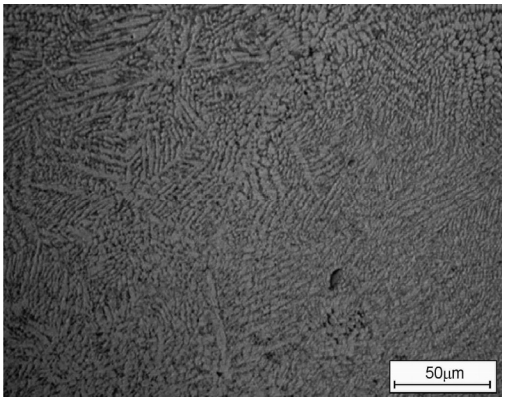

Fig. 115. Central zone of MCMgAl6Zn1 alloy after alloying by NbC, laser power 2.0 kW, scanning speed 0.25 m/min

Tests performed using scanning electron microscopy confirmed the presence of the zone-like structure of the surface layer of magnesium alloy castings (Figs. 116-121). In the re-melted area, there is a dendritic structure formed in accordance with the direction of heat dissipation, along with the un-melted particles of carbides used, or aluminium oxide. Re-melted layer structure after the laser surface treatment, including the share and carbide particle distribution, is dependent on laser power. It was found that the melting and/or laser fusing affects fragmentation of the structure in the surface layer at the whole operating range of the laser power, i.e. from 1.2 to 2.0 kW. As a result of metallographic observation of MCMgAl3Zn1, MCMgAl6Zn1, MCMgAl9Zn1, MCMgAl12Zn1 alloys, even distribution of particles of powders used was observed: TiC, WC and Al_2O_3 in the entire re-melting zone. (Figs. 116, 117, 120). In case of SiC particles fusing, at laser power of 1.2 kW, carbides are mainly placed at the surface layer. For the power of 1.6 kW and 2.0, in samples of MCMgAl12Zn1 and MCMgAl9Zn1, thanks to rapid stirring of molten metal in the liquid metal pool, the SiC particles are distributed throughout the melting zone (Fig. 119). The exception to the rule are cast magnesium alloys with laser fused particles of vanadium carbide, whose share in the re-melting zone is negligible (Fig. 118). A similar pattern was found in the fusing of niobium carbide particles, which have not been disclosed in the re-melted layer structure or its small share in quasi-composite layer (Fig. 121). In addition, in the surface-treated magnesium alloy casting using NbC powder, fine cracks were found in the surface layer of the material.

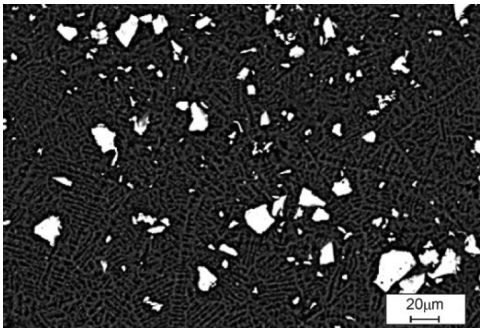

Fig. 116. Central zone of MCMgAl3Zn1 alloy after alloying by TiC, laser power 1.2 kW, scanning speed 0.75 m/min

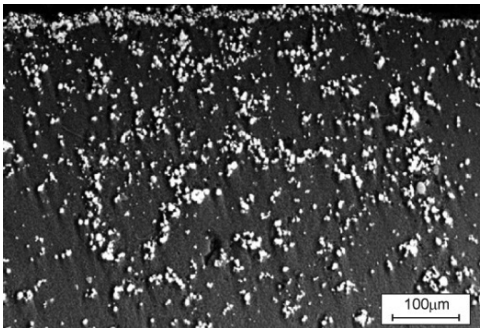

Fig. 117. Remelting zone of MCMgAl6Zn1 alloy after alloying by WC, laser power 1.6 kW, scanning speed 0.75 m/min

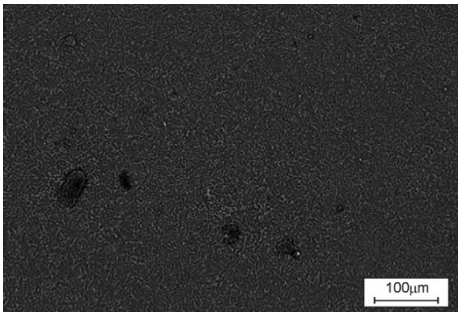

Fig. 118. Central zone of MCMgAl12Zn1 alloy after alloying by VC, laser power 1.6 kW, scanning speed 0.75 m/min

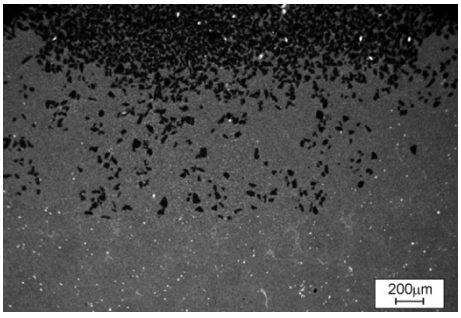

Fig. 119. Remelting zone of MCMgAl9Zn1 alloy after alloying by SiC, laser power 2.0 kW, scanning speed 0.75 m/min

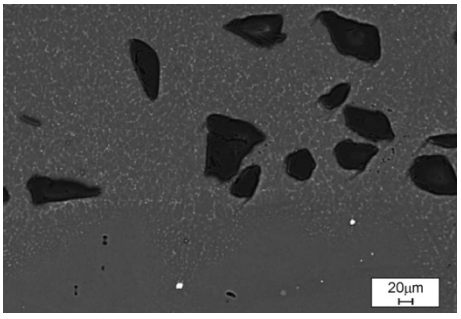

Fig. 120. Central zone of MCMgAl6Zn1 alloy after alloying by Al_2O_3, laser power 2.0 kW, scanning speed 0.50 m/min

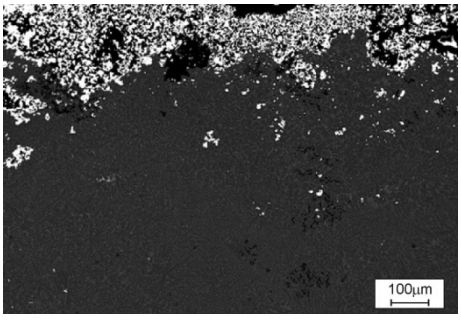

Fig. 121. Remelting zone of MCMgAl12Zn1 alloy after alloying by NbC, laser power 2.0 kW, scanning speed 0.25 m/min

As a result of X-ray phase qualitative analysis of surface layers of Mg-Al-Zn magnesium laser fused alloy castings, the occurrence of α - Mg phase, γ - $Mg_{17}Al_{12}$ phase, and reflections originating from used carbide powders: WC, TiC, VC, SiC, and Al_2O_3 oxide (Fig. 122). Due to small proportion of the remaining phases, below the threshold of detection by X-ray phase analysis (<3%), included in the structure of the substrate material, their unequivocal identification on radiograms was impossible.

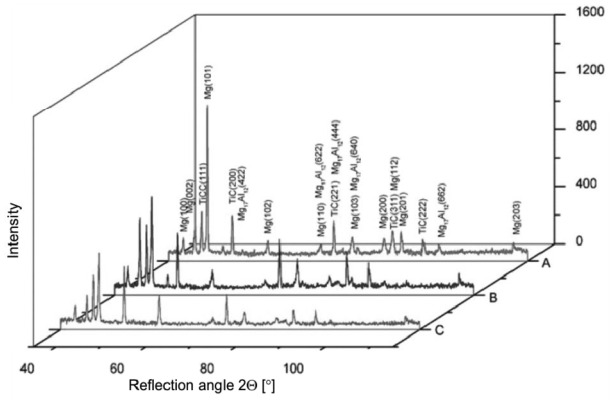

Fig. 122. X ray diffraction pattern of the MCMgAl12Zn1 after alloying by TiC, scanning speed 0.75 m/min, laser power: a) 1.2 kW, b) 1.6 kW, c) 2.0 kW

The results of X-ray qualitative and quantitative, linear and surface microanalysis, using scattered X-ray spectrometry. (Figs. 123-126, Table 25) obtained on the basis of tests carried out on the cross-section of surface layers of Mg-Al-Zn magnesium alloy casting, laser treated using TiC, WC, VC, SiC, Al_2O_3 powders confirm the presence of both major alloying elements being part of the substrate, and the phases present in the substrate, i.e. magnesium, aluminium, zinc, manganese, silicon, and alloys of the elements introduced in the process of laser fusing - titanium, tungsten, vanadium, silicon, aluminium and oxygen, thus confirming the lack of solubility of the fused particles.

Table 25.
Results of the quantitative analysis of chemical composition magnesium cast alloy MCMgAl9Zn1 after alloying SiC particles

Analysis	Element	The mass concentration of main elements, %	
		mass	atomic
1	Mg	67.72	70.79
	Si	32.28	29.21
2	Mg	5.77	7.77
	Al	58.51	70.95
	Mn	35.72	21.28
3	Mg	90.31	31.18
	Al	9.69	8.82
4	Zn	3.13	1.23
	Mg	63.64	67.17
	Al	33.23	31.6

a)

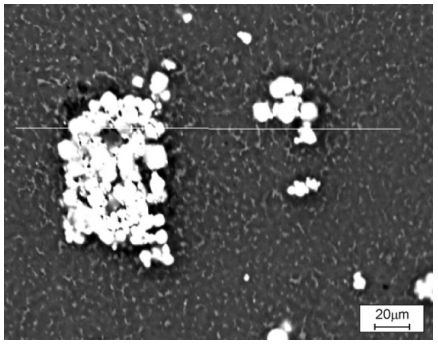

b)

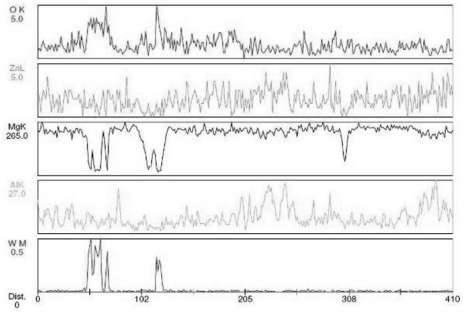

Fig. 123. The structure of the central zone of MCMgAl9Zn1 after alloying by WC, laser power 2.0 kW, scanning speed 0.75 m/min, a) structure, b) linear analysis of changes in the chemical composition

In addition, as a result of quantitative X-ray microanalysis, information was obtained about the mass and atomic concentration of individual elements in the spot-tested micro-areas of the matrix and ceramic particles used. It was also noted in some areas significantly increased levels of aluminium, manganese and silicon, which indicates the presence of Mn-Al phase, in most cases in the form of spheroidal or acicular and Mg_2Si phase with a distinct angular contour (Fig. 124, Table 25). Since the size of individual elements of the structure, due to its fineness, is smaller than the diameter of the beam, the chemical composition can be averaged over the chemical composition of the matrix and, as a result, in some of the elemental concentration may be overstated.

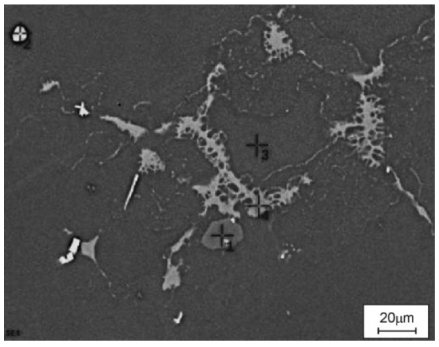

Fig. 124. The structure of the heat affected zone of MCMgAl9Zn1 after alloying by SiC, laser power 1.2 kW, scanning speed 0.75 m/min

a)

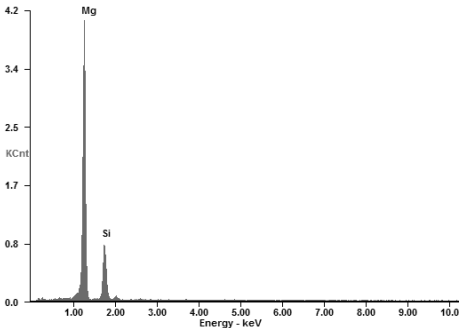

b)

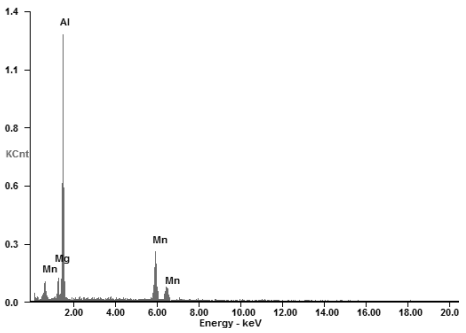

c)

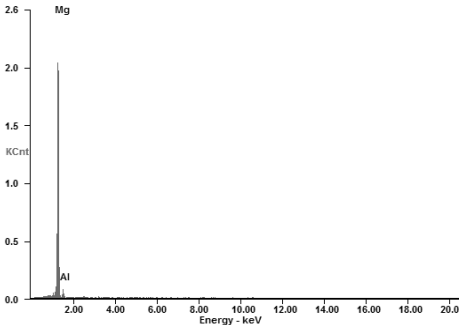

d)

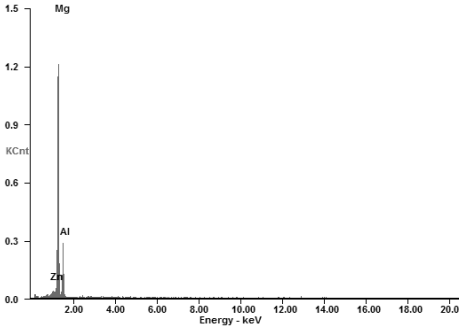

Fig. 125. EDS spectra of the MCMgAl9Zn1 after alloying SiC particles: a) analysis 1, b) analysis 2, c) analysis 3, d) analysis 4

On the basis of thin film testing in transmission electron microscope, it was found that the structure of the magnesium alloys cast with laser fused with carbide particles and aluminium oxide consists in fine grains of solid solution α -Mg with hexagonal network from the spatial group $P6_3/mmc$ o with high dislocation with solidifications of γ-$Mg_{17}Al_{12}$ (regular network, 143 m spatial group) and hard particle phases used for laser fusing (Figs. 127-129).

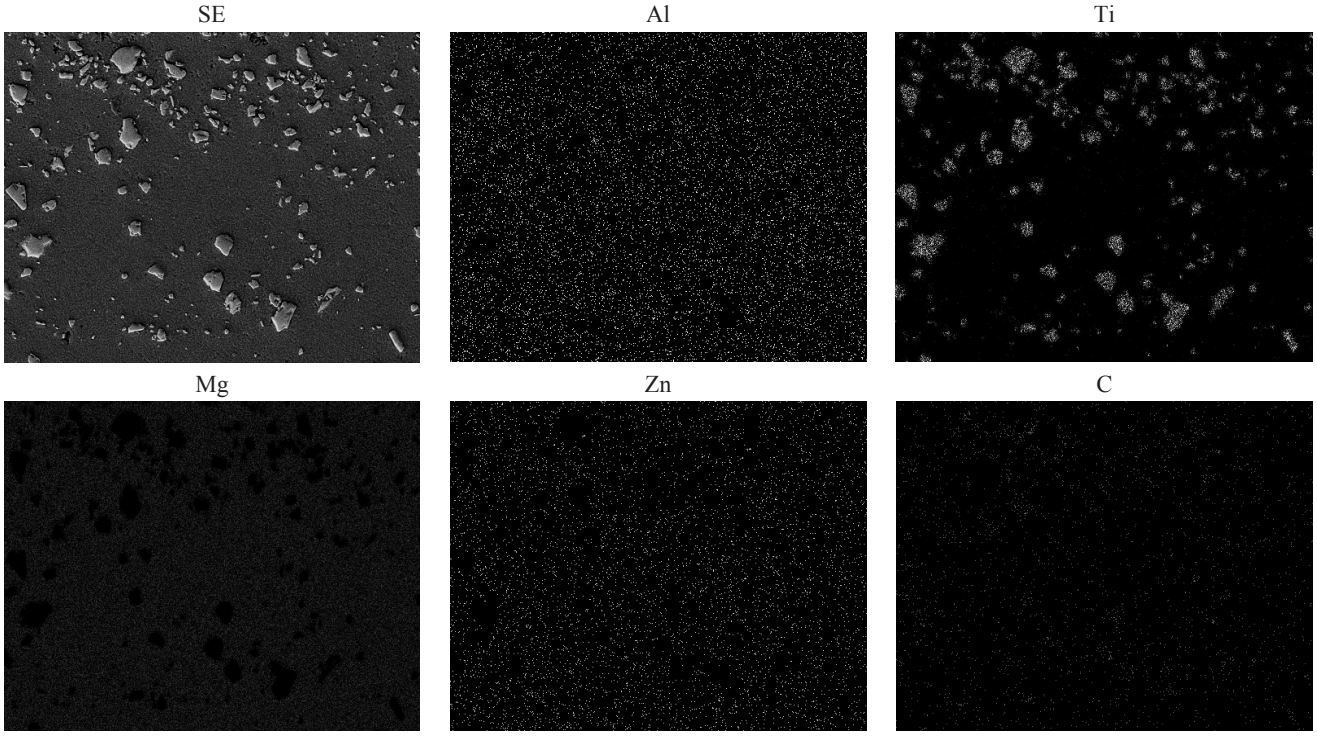

Fig. 126 . The area analysis of chemical elements alloy MCMgAl6Zn1 after alloying by TiC, laser power 1.6 kW, scanning speed 0.75 m/min: image of secondary electrons (A) and maps of elements' distribution

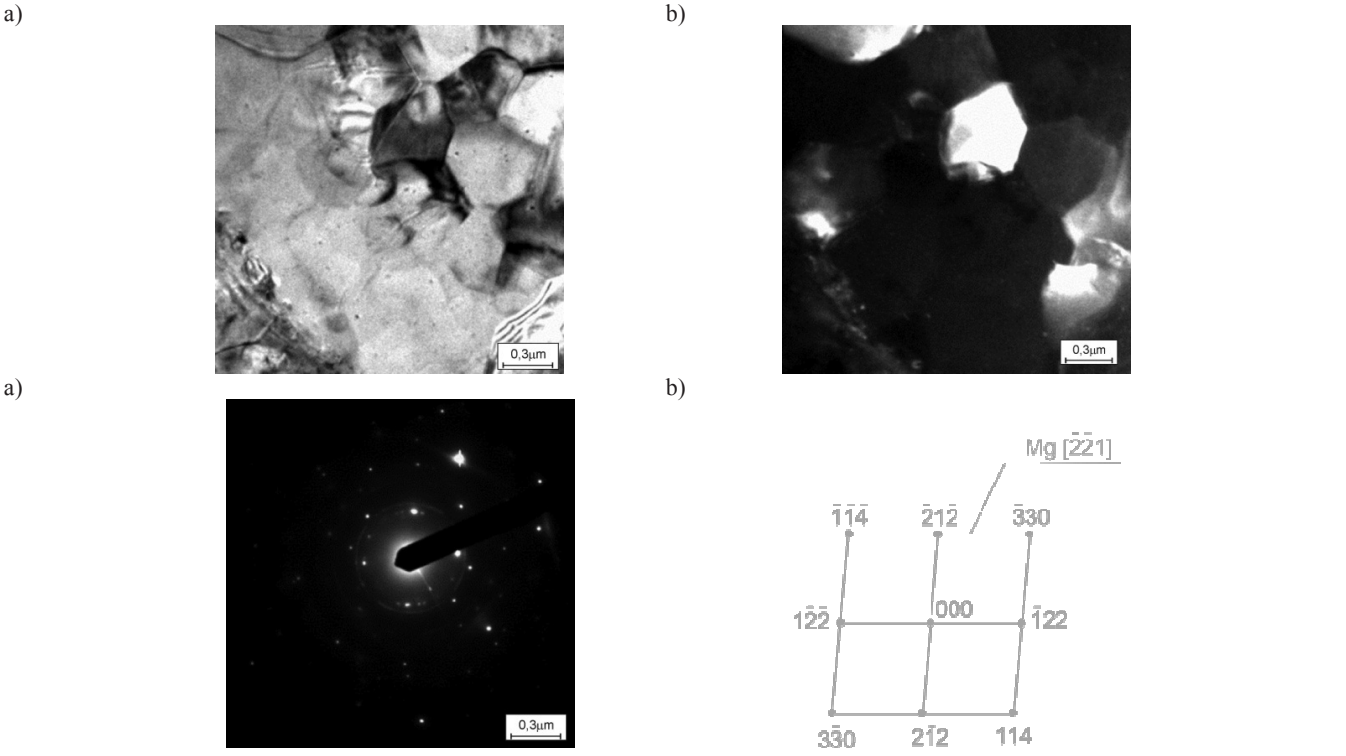

Fig. 127. TEM images of the MCMgAl12Zn1 alloy after alloying by VC particles, laser power 2.0 kW: a) bright field; b) dark field; c) diffraction pattern of area shown in a); d) solution for diffraction pattern shown in c)

a)

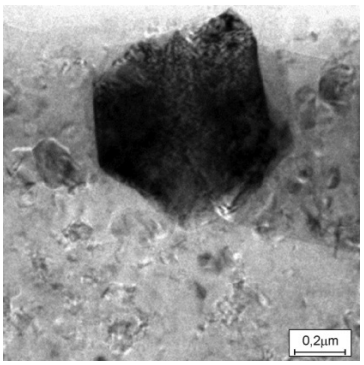

b)

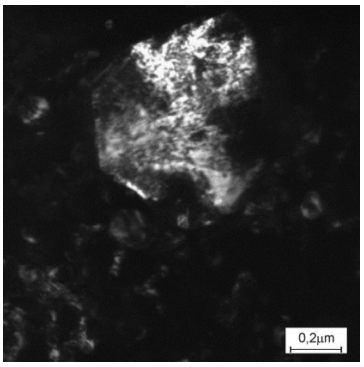

c)

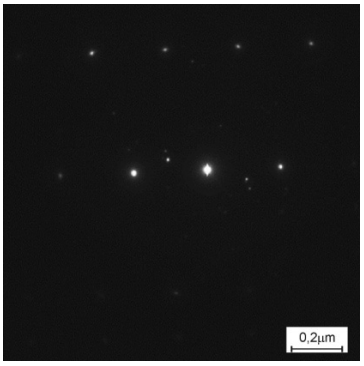

d)

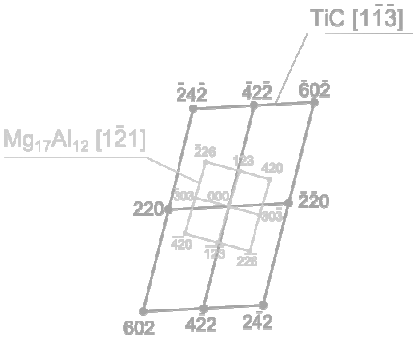

Fig. 128. TEM images of the MCMgAl12Zn1 alloy after alloying by TiC particles, laser power 1.6 kW: a) bright field; b) dark field; c) diffraction pattern of area shown in a); d) solution for diffraction pattern shown in c)

a)

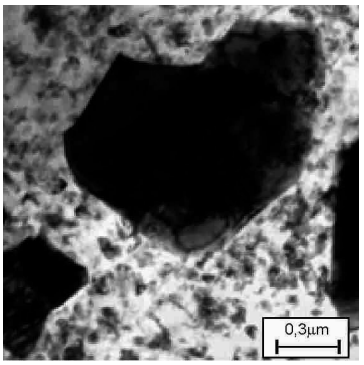

b)

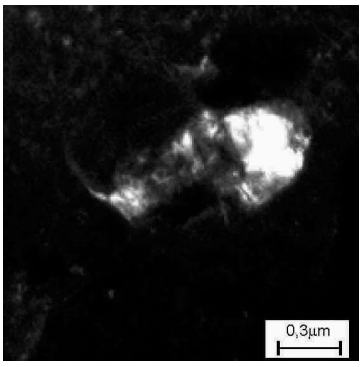

c)

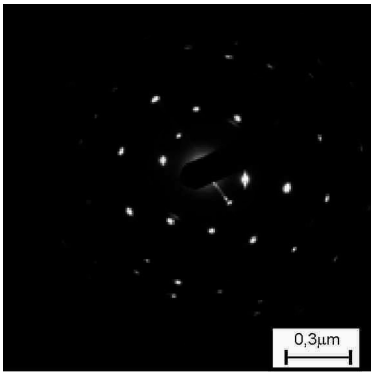

d)

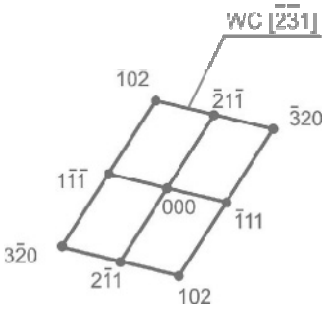

Fig. 129. TEM images of the MCMgAl6Zn1 alloy after alloying by WC particles, laser power 2.0kW: a) bright field; b) dark field; c) diffraction pattern of area shown in a); d) part of solution for diffraction pattern shown in c)

To determine the effect of laser fusing, using tungsten, titanium, silicon, vanadium, carbides powder, and aluminium oxide, as well as the effect of the laser treatment, in particular laser power on corrosion resistance of the tested Mg-Al-Zn alloys, corrosion tests were performed using electrochemical potentiodynamic method of in 3% NaCl aqueous solution. As a result, surface corrosion wear of the tested materials was found, depending on the mass concentration of aluminium powder, and laser power. For corrosion tests, top surfaces were selected, after fusing powders: TiC, WC, SiC, VC and Al_2O_3 due to their quality (shape and continuity of the surface).

Pitting corrosion was found in the tested materials. The nature of changes indicates the possibility of initiation of corrosion processes through the micropores present on the re-melting surface, causing local reduction of surface layers tightness. The anodic polarization curves, and corrosion current density indicate the dissolution rate of test surfaces. In all the tested samples after the laser treatment polarization resistance R_p decreases in comparison to samples without laser treatment. Literature studies show large discrepancies regarding the improvement of the corrosion resistance of magnesium alloys after laser treatment, and the authors of the various works present, at the same time, that the resistance of laser-treated Mg-Al-Zn alloy substrates increases [82] or decreases [83].

A slight shift of the anodic polarization curves (about 0.1V) defined for all the surface layers of tested casting magnesium alloys from laser-fused tungsten particles and aluminium oxide, in the positive direction with respect to the course of the curves obtained for the casting of magnesium alloys without laser treatment, indicates a slight increase in corrosion resistance of magnesium casting samples after laser fuses of the particles used, compared to the samples without laser treatment. Increasing polarization curves derived from the surface layer of magnesium alloy casting with laser-fused particles, in the anode area indicates the presence of pitting corrosion.

The defined values of density current i_{cor} and polarization resistance R_p (Table 26) indicate an adverse effect of fused particles on the corrosion resistance of casting magnesium alloys. As a measure of corrosion resistance, the value of corrosion current was assumed, using the proportionality of the rate of corrosion current density. This relationship shows that the bigger the value corrosion current, the lower the resistance of the surface layers in a corrosive environment. Obtaining higher corrosion currents samples of casting magnesium alloys with embedded laser-fused TiC, WC, SiC, VC and Al_2O_3 particles of higher values of corrosion currents, and lower corrosion potentials, in relation to the values determined for substrate and lower corrosion potentials regarding the values determined for substrate material, indicates a poorer corrosion resistance of magnesium alloy casting samples with laser-fused particles. Corrosion current density i_{cor} observed in the range of 0.009 mA/cm^2 to 1.913 mA/cm^2 respectively, for the surface layer of MCMgAl6Zn1 alloy after fusing Al_2O_3 with a laser power of 1.6 kW and MCMgAl3Zn1 alloy after TiC powder fusing with a laser power of 1.6 kW (Table 26). Polarization resistance value R_p was determined in the range of 13.59 Ω·cm^2 to 650 Ω·cm^2 respectively for the surface layer of MCMgAl6Zn1 alloy after Al_2O_3 powder fusing powder fusing 1.6 kW and MCMgAl3Zn1 alloy after TiC powder fusing at laser power of 1.6 kW (Table 26).

Table 26.
Change in the average value of i_{kor} and R_p of analysed magnesium alloys layers after alloying and corrosion test

	Moc lasera, kW	parametr	TiC	WC	VC	SiC	Al_2O_3
MCMgAl3Zn1	1.2	i_{kor}, mA/cm^2	0.819	1.016	2.582	--	--
		R_p, Ω·cm^2	31.73	25.58	10.07	--	--
	1.6	i_{kor}, mA/cm^2	1.913	1.303	1.074	0.582	--
		R_p, Ω·cm^2	13.59	19.96	24.2	44.81	--
	2	i_{kor}, mA/cm^2	1.26	0.801	0.744	0.091	0.049
		R_p, Ω·cm^2	20.62	32.44	34.93	341.43	603.34
MCMgAl6Zn1	1.2	i_{kor}, mA/cm^2	1.218	0.406	0.482	--	--
		R_p, Ω·cm^2	21.34	64.02	53.9	--	--
	1.6	i_{kor}, mA/cm^2	0.665	0.466	2.261	0.543	0.009
		R_p, Ω·cm^2	39.09	55.79	11.5	48.19	650
	2	i_{kor}, mA/cm^2	1.17	0.808	0.76	0.141	0.097
		R_p, Ω·cm^2	70.1	32.15	34.21	222.48	286.93
MCMgAl9Zn1	1.2	i_{kor}, mA/cm^2	0.843	0.594	0.408	0.365	--
		R_p, Ω·cm^2	30.84	43.71	63.76	72.47	--
	1.6	i_{kor}, mA/cm^2	0.987	0.467	0.52	0.086	0.085
		R_p, Ω·cm^2	26.33	55.71	50.01	308.09	307.41
	2	i_{kor}, mA/cm^2	0.793	1.033	0.394	0.135	0.124
		R_p, Ω·cm^2	32.78	25.18	66.05	192.25	201.79
MCMgAl12Zn1	1.2	i_{kor}, mA/cm^2	1.221	1.268	0.488	0.283	--
		R_p, Ω·cm^2	21.3	20.51	53.29	99.72	--
	1.6	i_{kor}, mA/cm^2	0.97	1.642	1.074	0.18	0.096
		R_p, Ω·cm^2	26.76	15.83	24.2	146.5	272.58
	2	i_{kor}, mA/cm^2	0.986	1.186	0.394	0.157	0.074
		R_p, Ω·cm^2	26.38	21.93	65.99	165.74	349.46

Table 27.
Results of HRF measurement of surface layer analysed magnesium alloys after alloying

	Laser power, kW	TiC	WC	VC	SiC	NbC	Al_2O_3
MCMgAl3Zn1	1.2	56.38	105.06	77.3	--	--	--
	1.6	49.36	68.4	38.7	39.5	33	--
	2	48.76	54.28	35.6	42.4	33.7	30.5
MCMgAl6Zn1	1.2	93.42	50.2	87.3	--	--	--
	1.6	74.42	63.34	80.56	40	50.8	41.9
	2	64.7	65.46	86.06	43	55.5	52.9
MCMgAl9Zn1	1.2	82.2	78.4	94.36	59.3	--	--
	1.6	78.76	86.28	68.58	78.5	76.4	67
	2	84.54	81.64	80.86	83.4	77.8	74.4
MCMgAl12Zn1	1.2	89.7	71.86	75.87	67.3	--	--
	1.6	91.62	83.94	68.72	84.7	84	79.5
	2	82.52	87.86	105.65	89	90.7	78.6

Table 28.
The loss of mass [%] in dependence on applied particles in surface layer of casting magnesium alloys after alloying

	Laser power, kW	TiC	WC	SiC	Al_2O_3
MCMgAl3Zn1	1.2	--	--	--	--
	1.6	--	111	318.18	--
	2	33	166	212.12	257.57
MCMgAl6Zn1	1.2	--	--	--	--
	1.6	50	58.3	218.75	1078.12
	2	83.3	183	156.25	101.56
MCMgAl9Zn1	1.2	--	--	107.84	--
	1.6	100	157	333.33	215.68
	2	85.7	128	147.05	98.03
MCMgAl12Zn1	1.2	--	--	303.03	--
	1.6	--	--	121.21	181.81
	2	--	--	45.45	45.45

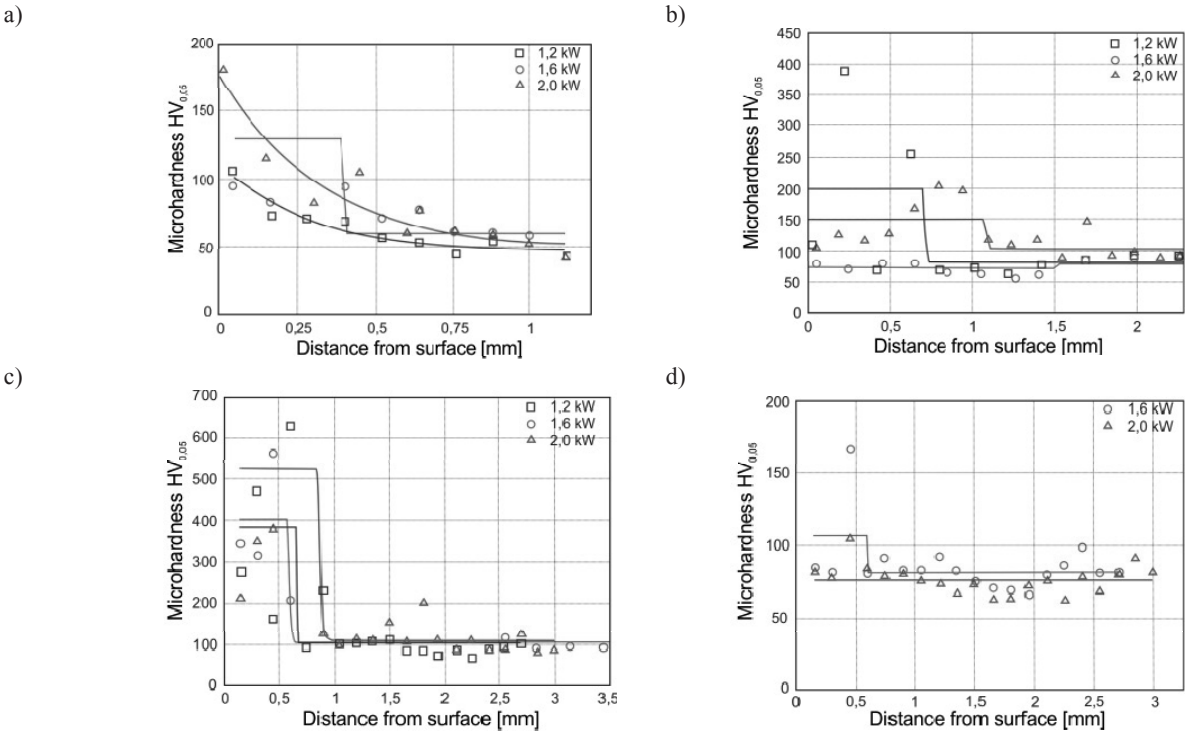

Fig. 130. Microhardness change of the surface layer of the magnesium cast alloy: a) MCMgAl6Zn1 alloyed with WC, alloying speed: 0.75 m/min, b) MCMgAl6Zn1 alloyed with TiC, alloying speed: 0.75 m/min, c) MCMgAl12Zn1 alloying speed SiC, alloying speed: 0.75 m/min, d) MCMgAl9Zn1 alloyed with Al_2O_3, alloying speed: 0.50 m/min

Fusing conditions (laser power, fusing rate), type of substrate, and the nature of the powder affect the hardness of Mg-Al-Zn cast magnesium alloys with laser fused carbide particles. Measured hardness of the layers fits in the range from 32.4 HRF (MCMgAl3Znl alloy with laser-fused particles of Al_2O_3) to 105.06 HRF (MCMgAl3Zn1 alloys with laser-fused particles of WC) (Table 27). As a result of tests, it was found that the greatest increase in hardness was observed in the case of laser enriched MCMgAl3Znl and MCMgAl6Znl magnesium alloys with ceramic particles (Tab. 27). The results of the hardness measurement of Mg-Al-Zn casting alloys with laser-fused particles of tungsten carbide and aluminium oxide indicate that in case of MCMgAl9Znl, MCMgAl12Znl alloys (Table 27) hardness is comparable to the hardness of the material without the laser treatment, and some conditions used in fusing worsens slightly compared to the material without laser treatment. Distribution of microhardness on the cross section of laser treated layers in the function of distance from the surface of the tested samples is shown in Figure 130. Microhardness of the surface layer of MCMgAl3Zn1, MCMgAl6Znl casting alloys with laser fused particles, on average increases twice, compared to those without laser treatment. Native material has a hardness at 70 to 140 $HV_{0.1}$, whereas the re-melting zone in the range of 80 to 700 $HV_{0.1}$. The large dispersion of the cross-sectional microhardness values in the re-melted zone is due to the presence of numerous fluctuations in chemical composition in the laser treated area. The hardness of the surface layer of the casting of magnesium alloys increases due to dispersion hardening, and grain refining. Literature data confirm the significant growth of microhardness as a result of laser treatment as a result of fragmentation of the structure of [84-87], and thanks to introducing hard ceramic powder particles into the magnesium matrix.

Summary of test results in wear resistance of casting of magnesium alloys with laser fused carbide particles is shown in Table 28, as a ratio of Δm weight loss of a sample after laser fusing to Δm weight loss of a heat-treated sample.

The biggest increase in wear resistance are characterized by MCMgA13Znl and MCMgAl6Znl casting magnesium alloys with laser-fused TiC carbide particles (Table 28). A nearly proportional effect of wear of the surface layer of the magnesium alloy castings with laser-fused particles of TiC carbides has been found depending on the type of substrate, and thus the thickness of the laser-treated surface layer.

3.5. Neural networks

Based on the developed neural network models, graphs were created, illustrating the impact of temperature and solutioning and aging time, and aluminium concentration on hardness of the analysed magnesium alloy castings (Fig. 131-134).

The results obtained clearly show that the most preferred type of heat treatment, both in terms of optimum operating conditions, and the consumed energy and time needed to carry out the solutioning and aging, as well as in terms of obtaining best mechanical properties is solutioning at 430°C for 10 hours, and aging at 190°C for 15 hours (Table 29).

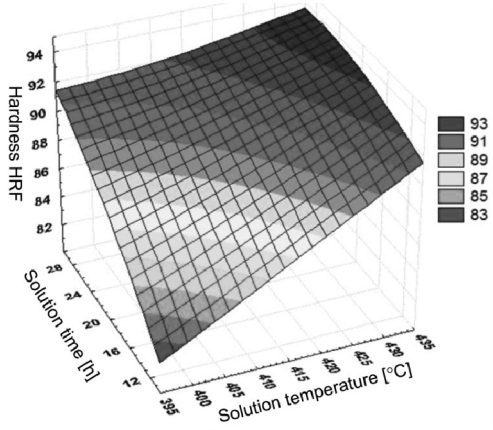

Fig. 131. Influence of temperature and solutioning time on hardness of MCMgAl12Zn1 magnesium alloys at 190°C and 15 h

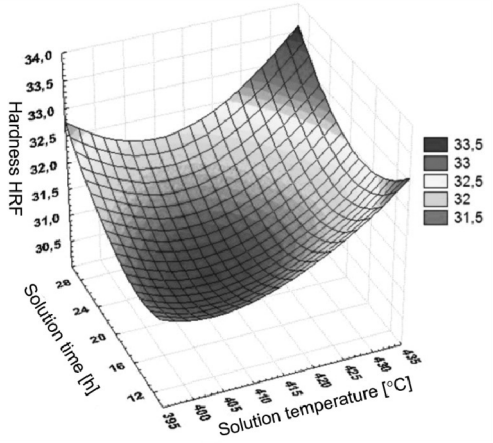

Fig. 132. Influence of temperature and solutioning time on hardness of MCMgAl3Zn1 magnesium alloys at 190°C and 15 h

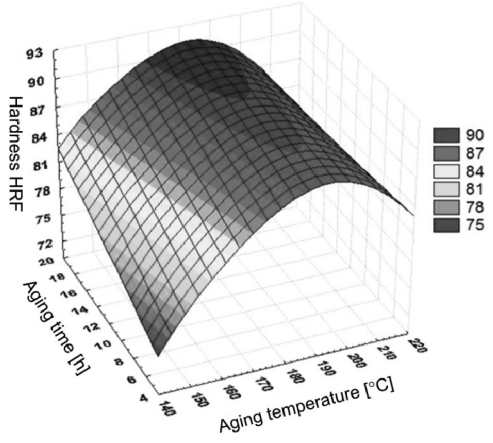

Fig. 133. Influence of temperature and aging time on hardness of MCMgAl12Zn1 magnesium alloys at 430°C and 10 h

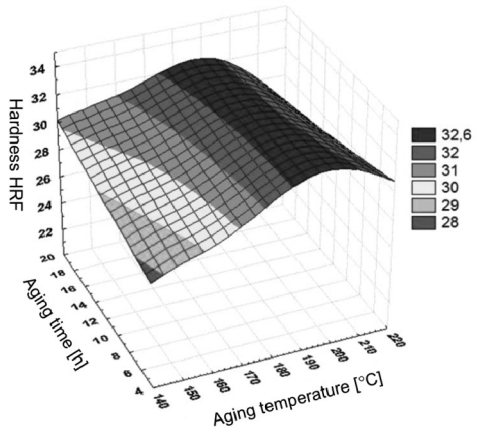

Fig. 134. Influence of temperature and aging time on hardness of MCMgAl3Zn1 magnesium alloys at 430°C and 10 h

Table 29.
Conditions of the heat treatment of analysed alloys

Indication of the heat treatment	Heat treatment		
	Temperature, °C	Time, h	Cooling method
0	As-cast		
1 - solutioning	430	10	water
2 - solutioning	430	10	air
3 - solutioning	430	10	furnace
4 - aging	190	15	air

Table 30 shows the error values, ratios of standard deviations and correlation coefficients of designed neural networks for the training set, validation and tests, which were the basis of assessment of network characteristics assessment. On the basis of the neural network quality assessment indicators, as well as ratios of standard deviations for the training and the test sets, accuracy in predicting the value of the output of the network can be inferred. The temperature of phase transformations modelled on the basis of the presented neural networks are shown in Figures 135-137.

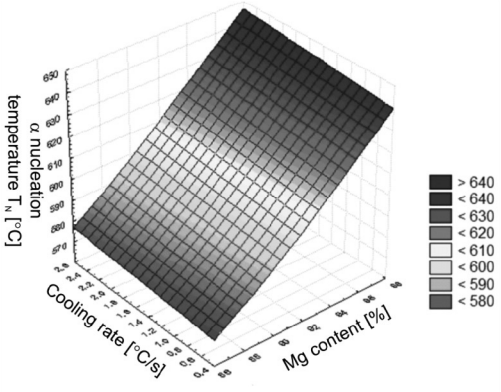

Fig. 135. Influence of cooling rate and magnesium content on α nucleation temperature of analysed magnesium alloys

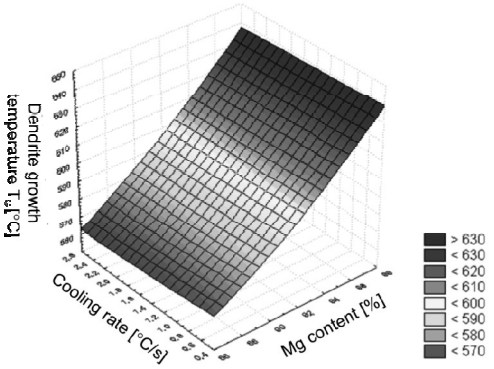

Fig. 136. Influence of cooling rate and magnesium content on dendrite growth temperature of analysed magnesium alloys

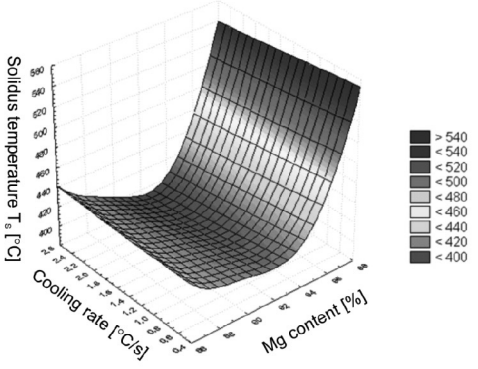

Fig. 137. Influence of cooling rate and magnesium content on solidus temperature of analysed magnesium alloys

Another analysed example is the use of neural networks in determining the heat values generated during Mg-Al-Zn crystallization, based on the mass concentration of aluminium and cooling rate. For numerical input and output variables, minimax variable conversion technique was used. The number of network layers has been described as three layers of 7 neurons in the hidden layer. Activation functions in the input and output layer were determined as linear with saturation, in the case of hidden layer as logistics, while for all the layers, PSP linear functions were used. The networks were taught using backpropagation (50 learning epochs) and conjugate gradients (112 learning epochs). The ratio of standard deviations was calculated for the adopted model of the neural network, for the grain size of 0.63. Table 31 shows the error ratios of standard deviations and correlation coefficients designed for neural networks for the training set, validation, and test sets. Figure 138 shows the values of heat generated during the crystallization of magnesium alloys modelled on the basis of the neural network.

In turn, neural networks used to determine grain size of Mg-Al-Zn cast alloys based on mass concentration of aluminium, and the cooling rate. To determine the grain size on the basis of aluminium mass concentration and cooling rate used, a MLP type unidirectional network with two neurons in the input layer was developed.

Table 30.
Regression statistics of neural network calculating the T_N, T_G and T_{sol} of magnesium alloys during crystallization

Temperature	Network architecture	Training set			Validating set			Testing set		
		Average error	Quotient of the standard deviations	Pearson's correlation coefficient	Average error	Quotient of the standard deviations	Pearson's correlation coefficient	Average error	Quotient of the standard deviations	Pearson's correlation coefficient
T_N	MLP 2:2-8-1:1	3.56	0.21	0.97	3.06	0.25	0.97	3.01	0.14	0.99
T_G	MLP 2:2-8-1:1	2.15	0.16	0.98	1.2	0.07	0.99	1.89	0.12	0.99
T_{sol}	MLP 2:2-8-1:1	4.54	0.15	0.98	4.6	0.15	0.98	2.83	0.1	0.99

Table 31.
Regression statistics of neural network calculating the latent heat of magnesium alloys during crystallization

Parameter	Network architecture	Training set			Validating set			Testing set		
		Average error	Quotient of the standard deviations	Pearson's correlation coefficient	Average error	Quotient of the standard deviations	Pearson's correlation coefficient	Average error	Quotient of the standard deviations	Pearson's correlation coefficient
Q_c	MLP 2:2-7-1:1	67.3	0.63	0.77	67.56	0.72	0.69	65.6	0.51	0.87

Table 32.
Regression statistics of neural network calculating the grain size of magnesium alloys after thermal analysis

Parameter	Network architecture	Training set			Validating set			Testing set		
		Average error	Quotient of the standard deviations	Pearson's correlation coefficient	Average error	Quotient of the standard deviations	Pearson's correlation coefficient	Average error	Quotient of the standard deviations	Pearson's correlation coefficient
Z	MLP 2:2-13-1:1	21.36	0.56	0.83	11.09	0.39	0.92	17.83	0.61	0.8

Table 33.
Regression statistics of neural network calculating the mechanical properties of magnesium alloys after thermal analysis

Property	Network architecture	Training set			Validating set			Testing set		
		Average error	Quotient of the standard deviations	Pearson's correlation coefficient	Average error	Quotient of the standard deviations	Pearson's correlation coefficient	Average error	Quotient of the standard deviations	Pearson's correlation coefficient
HRF	MLP 2:2-6-1:1	1.37	0.09	0.99	1.77	0.11	0.99	1.58	0.1	0.99
R_c	MLP 2:2-8-1:1	7.88	0.39	0.92	5.66	0.32	0.94	6.92	0.4	0.91
$R_{c0,2}$	MLP 2:2-4-1:1	8.72	0.39	0.91	6.74	0.34	0.94	13.15	0.37	0.96

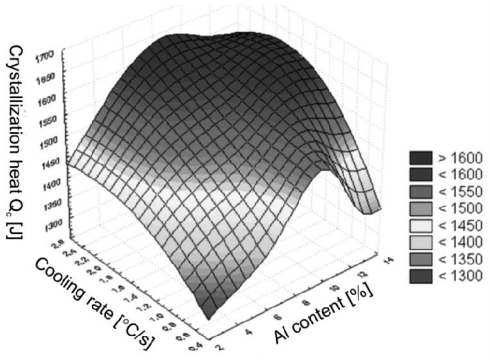

Fig. 138. Influence of cooling rate and aluminium content on latent heat of analysed magnesium alloys after thermal analysis

For input and output variables, minimax variable conversion technique was used. The number of network layers has been described as three layers of 13 neurons in the hidden layer. Activation functions in the input and output layer were determined as linear with saturation, in the case of hidden layer as logistics, while for all the layers, PSP linear functions were used. Networks were taught by backpropagation (14 learning epochs).

Table 32 shows the error values, ratios of standard deviations and correlation coefficients of designed neural networks for the training set, validation and test sets. Figure 139 shows the values of grain size on the basis of presented neural network. The developed neural network model allows to determine the grain size of error of ±21.36μm.

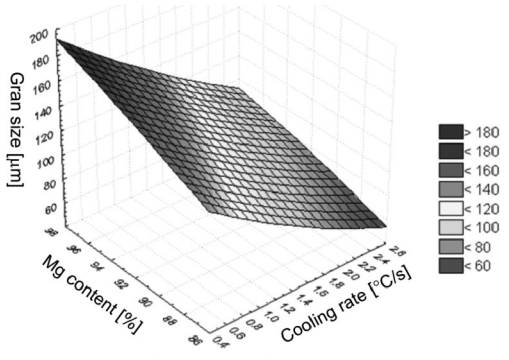

Fig. 139. Influence of cooling rate and magnesium content on grain size of analysed magnesium alloys after thermal analysis

Neural networks were also used to determine grain size of Mg-Al-Zn cast alloys based on mass concentration of aluminium, and the cooling rate.

For this purpose MLP type 2 unidirectional networks with 2 neurons in the input layer. For input and output variables, minimax variable conversion technique was used. The number of network layers has been described as three layers with 6 neurons in the hidden layer for the network calculating HRF hardness, with 8 neurons in the hidden layer of the network defining the compressive strength, and 4 neurons in the hidden layer defining the yield strength. Activation functions in the input and output layer were determined as linear with saturation, in the case of hidden layer as logistics, while for all the layers, PSP linear functions were used. Table 33 shows the error values, ratios of standard deviations and correlation coefficients of designed neural networks for the training set, validation and test sets. The values of mechanical properties for implemented neural networks are shown in Figures 140, 141. The developed neural network models allow for calculation, including the possible measurement error, the different values of material properties, i.e. hardness ±1.37 HRF, compressive strength of 7.88 MPa and a yield strength of ±8.72 MPa.

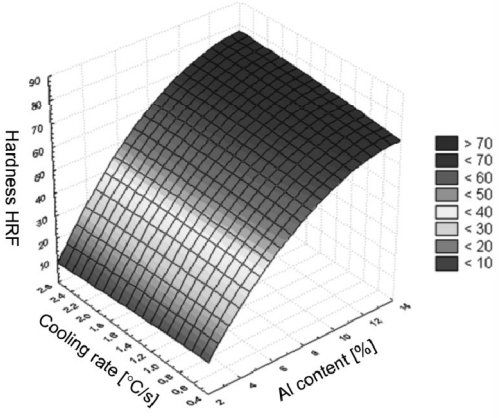

Fig. 140. Influence of cooling rate and aluminium content on hardness of analysed magnesium alloys after thermal analysis

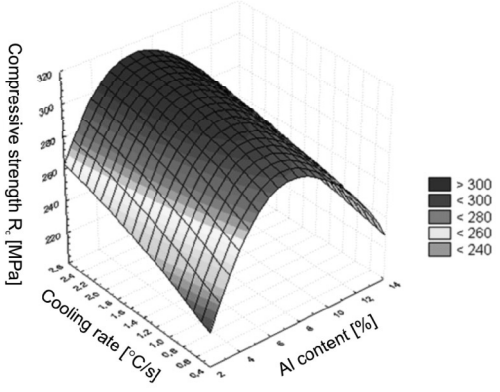

Fig. 141. Influence of cooling rate and aluminium content on ultimate compressive strength of analysed magnesium alloys after thermal analysis

On the basis of the developed neural network model, laser power influence graphs were created, graphs of concentration of aluminium, as well as graphs illustrating the type of fused powder on hardness of the analysed castings of magnesium alloys after laser fusing (Figs. 142-146). The graphs, in most cases, illustrate the remelting rate of 0.75 m/min, appropriate for optimum geometry for the laser path. The results clearly indicate that the highest hardness can be found in MCMgAl12Zn1, in whose surface TiC and WC powders were fused with a laser power of 2.0 kW and the rate of 0.75 m/min.

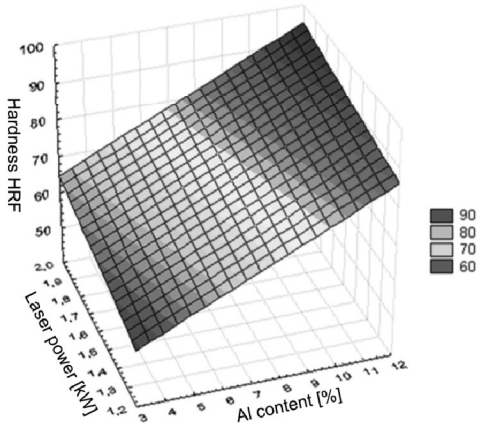

Fig. 142. Influence of aluminium content and laser power on hardness of magnesium alloys alloyed with TiC, alloying speed: 0.75 m/min

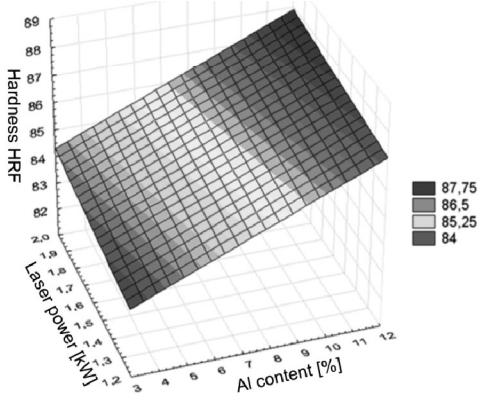

Fig. 143. Influence of aluminium content and laser power on hardness of magnesium alloys alloyed with VC, alloying speed: 0.75 m/min

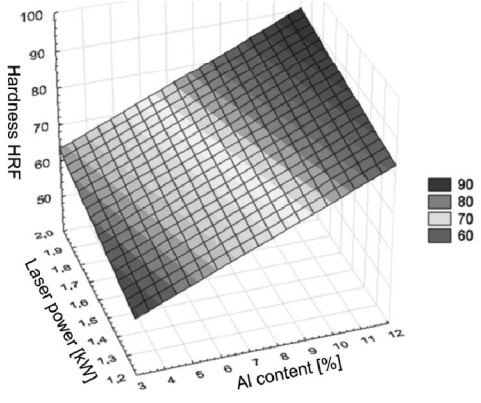

Fig. 144. Influence of aluminium content and laser power on hardness of magnesium alloys alloyed with WC, alloying speed: 0.75 m/min

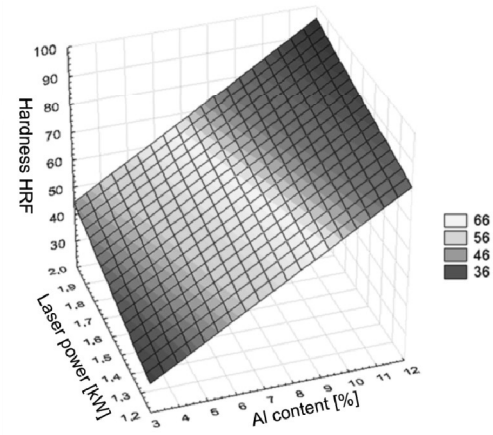

Fig. 145. Influence of aluminium content and laser power on hardness of magnesium alloys alloyed with SiC, alloying speed: 0.75 m/min

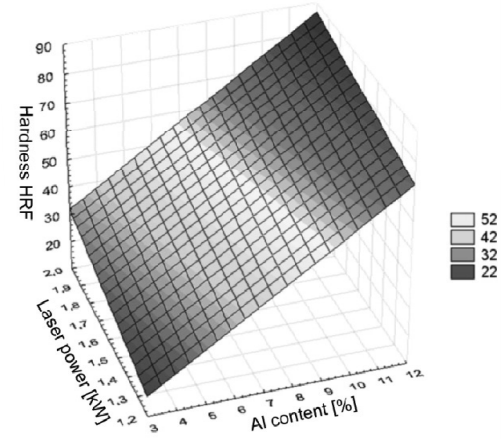

Fig. 146. Influence of aluminium content and laser power on hardness of magnesium alloys alloyed with Al_2O_3, alloying speed: 0.50 m/min

Table 34 shows the error ratios of standard deviation and correlation coefficients of the designed neural network, which is the basis for the assessment of the network.

Table 34.
Regression statistics of neural network calculating roughness of analysed magnesium alloys after alloying

Indicators of quality evaluation model	Data set		
	Training	Validating	Testing
Average error, HRF	1.99	1.68	1.53
Quotient of the standard deviations	0.42	0.41	0.42
Pearson's correlation coefficient	0.91	0.91	0.91

Moreover, on the basis of the developed neural network model, laser power influence graphs were created, graphs of concentration of aluminium, as well as graphs illustrating the type

of fused powder on roughness of the analysed castings of magnesium alloys after laser fusing (Figs. 147-151).

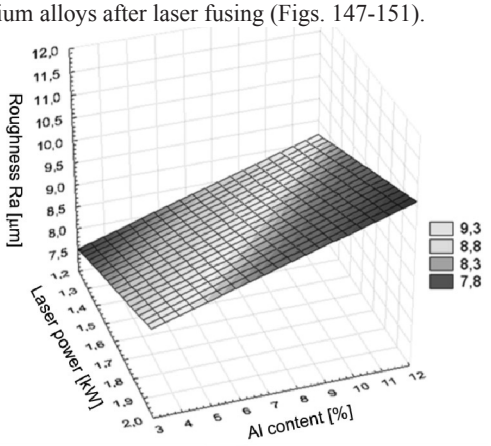

Fig. 147. Influence of aluminium content and laser power on roughness of magnesium alloys alloyed with TiC, alloying speed: 0.75 m/min

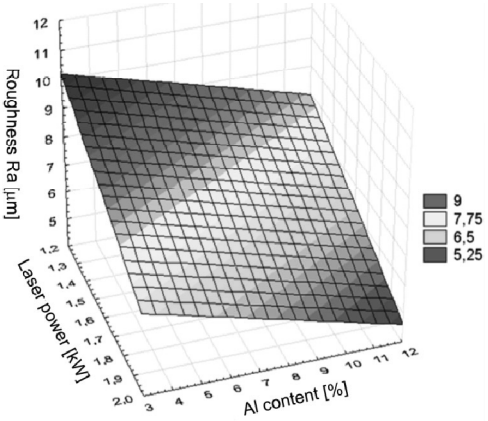

Fig. 148. Influence of aluminium content and laser power on roughness of magnesium alloys alloyed with VC, alloying speed: 0.75 m/min

The graphs, in most cases, illustrate the remelting rate of 0.75 m/min, appropriate for optimum geometry for the laser path. The results clearly indicate that the lowest roughness of the obtained composite layer can be found in MCMgAl12Zn1 casting alloys whose surface TiC and WC powders were fused, with a laser power of 2.0 kW and the rate of 0.75 m/min.

The ability to model the mechanical properties of the finished materials is very valuable for manufacturers and constructors. It means meeting the expectations and customer requirements regarding the quality of supplied products. Property modelling is also associated with financial benefits, as costly and time-consuming tests are reduced to a minimum, i.e. tests necessary to verify the predicted sizes. In the literature, there are many computational models predicting mechanical properties of different types of materials, but their industrial application is limited because of narrow ranges of the concentrations of various alloying elements or types requiring specific manufacturing conditions.

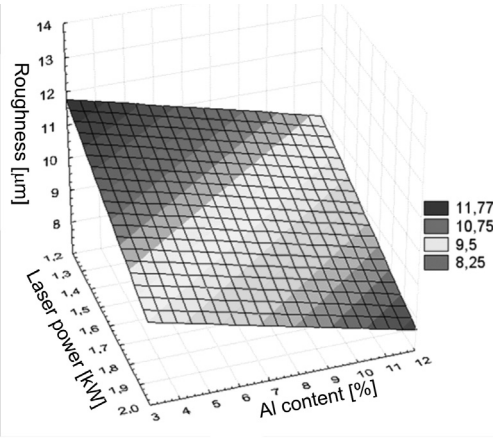

Fig. 149. Influence of aluminium content and laser power on roughness of magnesium alloys alloyed with WC, alloying speed: 0.75 m/min

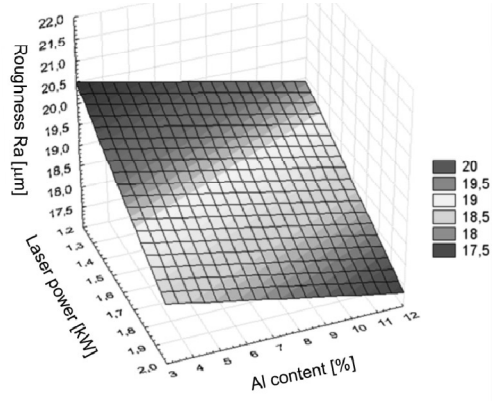

Fig. 150. Influence of aluminium content and laser power on roughness of magnesium alloys alloyed with SiC, alloying speed: 0.75 m/min

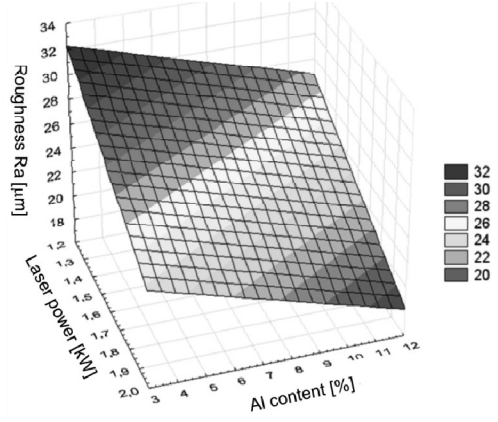

Fig. 151. Influence of aluminium content and laser power on roughness of magnesium alloys alloyed with Al_2O_3, alloying speed: 0.50 m/min

Acknowledgements

Mariusz Król is a holder of scholarship from the project POKL.04.01.01-00-003/09-00 entitled „Opening and development of engineering and PhD studies in the field of nanotechnology and materials science" (INFONANO), co-founded by the European Union from financial resources of European Social Fund and headed by Prof. L.A. Dobrzański.

References

[1] Z. Górny, J. Sobczak, Non-ferrus metals based novel materials in foundry practice, Publisher Institute of Foundry, Cracow, 2005 (in Polish).
[2] L.A. Dobrzański, Materials engineering and materials design: fundamentals of materials science and metallography, Scientific and Technical Publishing, Warsaw, 2006 (in Polish).
[3] L.A. Dobrzański, T. Tański, L. Čížek, Z. Brytan, Structure and properties of the magnesium casting alloys, Journal of Materials Processing Technology 192-193 (2007) 567-574.
[4] K. Przybyłowicz, Metallography, Scientific and Technical Publishing, Warsaw, 2007 (in Polish).
[5] L.A. Dobrzański, Rules of selection of engineering materials, Publisher of Silesian University of Technology, Gliwice, 2001 (in Polish).
[6] H. Friedrich, S. Schumann, Research for a "new age of magnesium" in the automotive industry, Journal of Materials Processing Technology 117 (2001) 276-281.
[7] H. Baker, ASM Specialty Handbook, Magnesium and magnesium alloys, Avedesian (Ed.), ASM International, The Materials Information Society, USA 1999.
[8] L.A. Dobrzański, T. Tański, L. Čížek, The microstructure and mechanical properties of Mg - Al cast magnesium alloys, Archives of Foundry Engineering 6/22 (2006) 614-619 (in Polish).
[9] M. Saternus, Magnesium - technology, production and perspectives, Ores and non-ferrous metals 53/6 (2008) 337-349 (in Polish).
[10] L.A. Dobrzański, B. Tomiczek, M. Pawlyta, M. Król, Aluminium AlMg1SiCu matrix composite materials reinforced with halloysite particles, Archives of Metallurgy and Materials 59/1 (2014) 333-336
[11] F. Biczyk, Structural casting alloys, Publisher of Silesian University of Technology, Gliwice, 2003 (in Polish).
[12] K.U. Kainem, Magnesium - Alloys and Technology, Willey-VH, Weinheim, 2003.
[13] Z. Górny, Casting of metals and alloys, vol. III. Special methods of casting, Foundry Institute, Cracow, 1997.
[14] A. Kosowski, Metallography of cast alloys, AGH Publisher, Cracow, 1996 (in Polish).
[15] S. Lun Sin, D. Dubé, Influence of process parameters on fluidity of investment-cast AZ91D magnesium alloy, Materials Science and Engineering A 386 (2004) 34-42.
[16] R. Dębicki, Growth application perspectives of non-ferrous castings for the automotive industry, Materials of science conference, „Modern trends in non-ferrous metal foundry", Cracow, 1997, 37-59 (in Polish).
[17] A. Białobrzeski, Pressure founding, Scientific and Technical Publishing, Warsaw 1992 (in Polish).
[18] A. Fajkiel, P. Dudek, Magnesium alloys - a modern station for casting in Foundry Research Institute in Cracow, Bulletin of the Institute of Foundry no. 3, Cracow, 2000 (in Polish).
[19] L.A. Dobrzański, T. Tański, Influence of aluminium content on behaviour of magnesium cast alloys in bentonite sand mould, Solid State Phenomena 147-149 (2009) 764-769.
[20] J. Sieniawski, Metallography and heat treatment, Rzeszów University of Technology Publishing House, Rzeszow, 2001 (in Polish).
[21] Standard specification for magnesium alloys die castings, ASTM B94-94, American Society for Testing and Materials, 1994.
[22] M. Szweycer, D. Nagolska, Metallurgy and foundries - materials technology, Publisher of Poznan University of Technology, Poznan, 2002 (in Polish).
[23] M. Svoboda, M. Pahutová, K. Kuchařová, V. Sklenička, T.G. Langdon, The role of matrix microstructure in the creep behaviour of discontinuous fiber-reinforced AZ 91 magnesium alloy, Materials Science and Engineering A 324 (2002) 151-156.
[24] L. Čížek, J. Hubáčková, M. Greger, L. Pawlica, R. Kocich, B. Smetana, T. Tański, S. Król, Heat treatment of selected magnesium alloys, 21 Days of Heat Treatment, Jihlava 2006, 361-366.
[25] L. Čížek, R. Kocich, M. Greger, T. Tański, M. Prażmowski, Study of microstructure selected magnesium alloys, Materials Engineering 14 (2007) 21-24.
[26] L.A. Dobrzański, T. Tański, L. Čížek, Investigation of the MCMgAl12Zn1 magnesium alloys structure after heat treatment, Journal of Achievements in Materials and Manufacturing Engineering 29/1 (2008) 23-30.
[27] L. A. Dobrzański, T. Tański, Sz. Malara, M. Król, J. Domagała-Dubiel, Contemporary forming methods of the structure and properties of cast magnesium alloys, Magnesium Alloys - Design, Processing and Properties, F. Czerwinski (Ed.), Publisher InTech, 2011, 321-350.
[28] A. Kiełbus, T. Rzychoń, R. Cibis, Microstructure of AM50 die casting magnesium alloy, Journal of Achievements in Materials and Manufacturing Engineering 18 (2006) 135-138.
[29] L. A. Dobrzański, M. Król, T. Tański, Thermal analysis, structure and mechanical properties of the MC MgAl3Zn1 cast alloy, Journal of Achievements in Materials and Manufacturing Engineering 40/2 (2010) 167-174.
[30] L.A. Dobrzański, W. Kasprzak, J. Sokołowski, R. Maniara, M. Krupiński, Applications of the derivation analysis for assessment of the ACAlSi7Cu alloy crystallization process cooled with different cooling rate, Proceedings of the 13th Scientific International Conference on "Achievements in Mechanical and Materials Engineering" AMME'2005, Gliwice-Wisła, 2005, 147-150.

[31] L.A. Dobrzański, R. Maniara, J.H. Sokolowski, The effect of cooling rate on microstructure and mechanical properties of AC AlSi9Cu alloy, Archives of Materials Science and Engineering 28/2 (2007) 105-112.
[32] L.A. Dobrzański, R. Maniara, J. Sokołowski, W. Kasprzak , Effect of cooling rate on the solidification behavior of AC AlSi7Cu2 alloy, Journal of Materials Processing Technology 191 (2007) 317-320.
[33] W. Longa, solidification of castings, Publisher „Śląsk", Katowice, 1985 (in Polish).
[34] M. Stawarz, J. Szajnar, Quality assessment of ductile iron by ATD method, Archives of Foundry Engineering 3/10 (2003) 199-206 (in Polish).
[35] T. Tański, K. Labisz, Electron microscope investigation of PVD coated aluminium alloy surface layer, Solid State Phenomena 186 (2012) 192-197.
[36] T. Tański, K. Lukaszkowicz, Investigation of microstructure and mechanical properties of PVD-coated magnesium and aluminium alloys, Proceedings of the 8th International Conference on Industrial Tools and Material Processing Technologies, 2011, 363-368.
[37] L.A. Dobrzański, K. Lukaszkowicz, A. Kriz, Properties of multi-layer Ti/CrN and Ti/TiAlN coatings deposited with the PVD technique onto the brass substrate, Journal of Materials Processing Technology 143 (2003) 832-837.
[38] K. Lukaszkowicz, J. Sondor, A. Kriz, M. Pancielejko, Structure, mechanical properties and corrosion resistance of nanocomposite coatings deposited by PVD technology onto the X6CrNiMoTi17-12-2 and X40CrMoV5-1 steel substrates, Journal of Materials Science 45 (2010) 1629-1637.
[39] T. Tański, Investigation of the structure and properties of PVD and PACVD-coated magnesium die cast alloys, Magnesium Alloys, Waldemar A. Monteiro (Ed.), Publisher InTech, 2012 (in print).
[40] T. Tański, K. Labisz, K. Lukaszkowicz, Structure and properties of diamond-like carbon coatings deposited on non-ferrous alloys substrate, Solid State Phenomena 199 (2013) 170-175.
[41] L.A. Dobrzański, M. Staszuk, PVD and CVD gradient coatings on sintered carbides and sialon tool ceramics, Journal of Achievements in Materials and Manufacturing Engineering. 43/2 (2010) 552-576.
[42] H. Altun, S. Sen, The effect of PVD coatings on the wear behaviour of magnesium alloys, Materials Characterization 58 (2007) 917-921.
[43] J. Liang, P. Wang, L.T. Hu, J.C. Hao, Tribological properties of duplex MAO/DLC coatings on magnesium alloy using combined microarc oxidation and filtered cathodic arc deposition, Materials Science and Engineering A 454-455 (2007) 164-169.
[44] H.Q. Sun, Y.N. Shi, M.X. Zhang, Wear behaviour of AZ91D magnesium alloy with a nanocrystalline surface layer, Surface and Coating Technology 202 (2008) 2859-2864.
[45] L.A. Dobrzański, A.D. Dobrzańska-Danikiewicz, Forming of the engineering materials surface structure and properties, The Silesian University of Technology Publishing House, Gliwice, 2013, 1-492 (in Polish).
[46] L.A. Dobrzański, J. Domagała, T. Tański, A. Klimpel, D. Janicki, Laser surface treatment of magnesium alloy with WC powder, Archives of Materials Science and Engineering 30/2 (2008) 113-116.
[47] L.A. Dobrzański, Sz. Malara, T. Tański, Laser surface treatment of magnesium alloys with aluminium oxide powder, Journal of Achievements in Materials and Manufacturing Engineering 37/1 (2009) 70-77.
[48] L. A. Dobrzański, T. Tański, Sz. Malara, Effect of the heat and surface laser treatment on the corrosion degradation of the Mg-Al alloys, Materials Engineering - Materiálové inžinierstvo 18 (2011) 85-92.
[49] T. Tański, K. Lukaszkowicz, Structure and mechanical properties of hybrid PVD coatings applied onto magnesium and aluminum alloys, Materials Engineering 4/182 (2011) 772-775 (in Polish).
[50] L.A. Dobrzański, T. Tański, J. Domagała, M. Bonek, A. Klimpel, Microstructure analysis of the modified casting magnesium alloys after heat and laser treatment, Journal of Achievements in Materials and Manufacturing Engineering 32/1 (2009) 7-12.
[51] A. Klimpel, Laser technologies in welding, Publisher of Silesian University of Technology, Gliwice, 2011 (in Polish).
[52] J. Kusiński, Lasers and their applications in materials engineering, Scientific Publishers „Akapit", Cracow, 2002 (in Polish).
[53] J. Kusiński, Joint penetration laser treatment, Ironmaster - Ironmaster News 4 (2002) 166-175 (in Polish).
[54] A. Klimpel, The application of high power diode laser for welding and surfacing, Overview of welding 6 (2001) 1-6 (in Polish).
[55] T. Burakowski, T. Wierzchoń, Engineering of metal surfaces, Scientific and Technical Publishing, 1995 (in Polish).
[56] C. Bishop, Neural networks for pattern recognition, Oxford University Press, London, 1995.
[57] T. Masters, Neural networks in practice, WNT Publisher, Warsaw, 1996 (in Polish).
[58] L.A. Dobrzański, A. Śliwa, T. Tański, Numerical simulation model for the determination of hardness for casting the magnesium alloys MCMgAl6Zn1, Archives of Materials Science 29/ 3 (2008) 118-124.
[59] L.A. Dobrzański, T. Tański, J. Trzaska, Optimization of heat treatment conditions of magnesium cast alloys, Materials Science Forum 638-642 (2010) 1488-1493.
[60] L.A. Dobrzański, M. Król, T. Tański, Application a neural networks in crystallization process of Mg-Al-Zn alloys, Archives of Computational Materials Science and Surface Engineering 2/3 (2010) 149-156.
[61] L. A. Dobrzański, T. Tański, The application of neural networks to optimize the heat treatment conditions of Mg-Al alloys, Technical Magazine, Mechanics, 7/108 (2011) 81-86 (in Polish).
[62] W.S. McCulloch, W. Pitts, Bulletin of Mathematical Biophysics, 9, 1943.
[63] M. Nałęcz, W. Ducha, J. Korbicz, L. Rutkowskiego, R. Tadeusiewicza, Biocybernetics and Biomedical Engineering, vol. 6, Neural networks, EXIT, Warsaw, 2000 (in Polish).

[64] R. Tadeusiewicz, Neural networks, Academic Publishing House RM, Warsaw 1993 (in Polish).
[65] M.H. Beale, H.B. Demuth, M.T. Hagan, Neural network design, University of Colorado Bookstore, Boulder, Colarado, 2002.
[66] "Method and Apparatus for Universal Metallurgical Simulation and Analysis" - United States Patent, Patent No: US 7,354,491 B2, Date of Patent 2008, Canadian Patent, Patent No.:CA 2 470 127, Date of Patent 2009.
[67] www.uwindsor.ca/umsa.
[68] L. A. Dobrzański, M. Król, T. Tański, Influence of cooling rate on crystallization, structure and mechanical properties of MCMgAl6Zn1 alloy, Archives of Foundry Engineering 10/3 (2010) 105-110.
[69] L.A. Dobrzański, M. Król, T. Tański, Effect of cooling rate and aluminum contents on the Mg-Al-Zn alloys' structure and mechanical properties, Journal of Achievements in Materials and Manufacturing Engineering 43/2 (2010) 613-633.
[70] L.A. Dobrzański, M. Król, T. Tański, R. Maniara, Thermal analysis of the MCMgAl9Zn1 magnesium alloy, Journal of Achievements in Materials and Manufacturing Engineering vol. 34/2 (2008), pp. 113-116
[71] L. A. Dobrzański, M. Król, T. Tański, R. Maniara, Effect of cooling rate on the solidification behaviour of MCMgAl6Zn1 alloy, Archives of Materials Science and Engineering 29/3 (2008) 110-117.
[72] L.A. Dobrzański, M. Król, T. Tański, R. Maniara, Effect of cooling rate on the solidification behaviour of magnesium alloys, Archives of Computational Materials Science and Surface Engineering 1/1 (2009) 21-24.
[73] L.A. Dobrzański, M. Król, T. Tański, R. Maniara, Effect of cooling rate on the solidification behaviour of MC MgAl6Zn1 alloy, Journal of Achievements in Materials and Manufacturing Engineering 37/1 (2009) 65-69.
[74] www.crct.polymtl.ca
[75] S. Jura, Z. Jura, Theory of ATD method in studies of Al alloys, Solidification of Metals and Alloys 28 (1996) 57-87 (in Polish).
[76] S. Pietrowski, Silumin, Publisher of University of Lodz, Łódź, 2001 (in Polish).
[77] J. Gawroński, The crystallization of alloys. Method of thermal and derivative analysis (ATD), Archives of Foundry Engineering, 16 (2005) 256-261 (in Polish).
[78] L. Backuerud, G. Chai, J Tamminen, Solidification characteristics of aluminum alloys vol. 3 Foundry alloys, AFS Skanaluminium, Stockholm, 1990.
[79] T. Tański, K. Lukaszkowicz, Structure and mechanical properties of hybrid PVD coatings applied onto the magnesium and aluminum alloys, Materials Engineering, 4/182 (2011) 772-775 (in Polish).
[80] L. Čížek, L. Pawlica, R. Kocich, M. Janošec, T. Tański, M. Prażmowski, Structure and properties of Mg-Zr and Mg-Si alloys, Journal of Achievements in Materials and Manufacturing Engineering 27/2 (2008) 127-130.
[81] Y.S. Zou, Y.F. Wu, H. Yang, K. Cang, G.H. Song, Z.X. Li, K. Zhou, The microstructure, mechanical and friction properties of protective diamond like carbon films on magnesium alloy, Applied Surface Science 258 (2011) 1624-1629.
[82] G. Abbas, Z. Liu, P. Skeldon, Corrosion behaviour of laser-melted magnesium alloys, Applied Surface Science 247 (2005) 347-353.
[83] D. Dube, M. Fiset, A. Couture, I. Nakatsugawa, Characterization and performance of laser melted AZ91D and AM60B, Materials Science and Engineering A 299 (2001) 38-45.
[84] L. Li, The advances and characteristics of high-power diode laser materials processing, Optics and Lasers in Engineering 34 (2000) 231-253.
[85] Y. Jun, G.P. Sunb, S.S. Jia, Characterization and wear resistance of laser surface melting AZ91D alloy, Journal of Alloys and Compounds 455 (2008) 142-147.
[86] J.D. Majumdar, R. Galun, B.L. Mordike, I. Manna, Effect of laser surface melting on corrosion and wear resistance of a commercial magnesium alloy, Materials Science Engineering A 361 (2003) 119-129.
[87] A.K. Mondal, S. Kumar, C. Blawert, N.B. Dahotre, Effect of laser surface treatment on corrosion and wear resistance of ACM720 Mg alloy, Surface and Coating Technology 202 (2008) 3187-3198.